UNIVERSIDAD DE GUANAJUATO

CAMPUS GUANAJUATO

DIVISIÓN DE CIENCIAS NATURALES Y EXACTAS

SEARCHING FOR THE INFLUENCE RADIUS OF AGN IN NEARBY NARROW-EMISSION-LINE GALAXIES USING THE CALIFA SURVEY

Tesis presentada al

POSGRADO EN CIENCIAS (ASTROFÍSICA)

como requisito para la obtención del grado

MAESTRÍA EN CIENCIAS (ASTROFÍSICA)

por

LIC. AITOR CARLOS ROBLETO ORÚS

asesorado por

DR. JUAN PABLO TORRES PAPAQUI (DA-UGto)

Guanajuato, Gto. - Septiembre 2017

Dedicado a mis padres Conchita y Carlos, y a mi abuela Purita.

Agradecimientos

A pesar de que una tesis se entiende como el trabajo de una sola persona guiada por un director o asesor, la realidad es que se trata de un viaje en el que nos apoyamos en muchas personas sin las cuales dicho viaje no sería posible. Agradezco a:

Mi asesor de tesis, Dr. Juan Pablo Torres Papaqui, por estar siempre cuando lo necesité, abierto a discutir nuevas ideas y explorar nuevos caminos, lo que permitió que el presente trabajo creciera a algo mucho mayor a lo originalmente planeado, así como su apoyo económico y de gestión, para que pudiera yo asistir a cursos y congresos, lo cual enriqueció enormemente esta tesis.

Los sinodales, Dr. Heinz Andernach, Dr. Roger Coziol, Dr. René Ortega y Dr. César Caretta, cuyos importantes comentarios ayudaron mucho, enriqueciendo y dándole perspectiva al presente documento.

A Karla Arellano, por ser un gran apoyo en todos los sentidos, por darme un lugar especial, por acogerme durante mis vistias, cursos y congresos en Puebla y acompañarme y apoyarme en los viajes, y en todo momento, y muy importante para este trabajo, por sus inestimables puntos de vista, enseñanzas y consejos.

A mis compañeros del posgrado, muy especialmente a los miembros del grupo GIFU, Abdías Morales, Fernando Romero, Josué Trejo, René Ortega y Daniel Neri, quienes desarrollaron una parte de los scripts de extracción de datos eque se usaron en esta tesis, así como el útil intercambio de ideas en las reuniones de grupo.

Un lugar muy especial en estos agradecimientos lo tiene Marcel Chow, un gran amigo, que me animó a seguir adelante y me apoyó en los peores momentos, y de cuyo basto conocimiento también se nutrió un poco esta tesis, especialmente por sus consejos en programación y métodos matemáticos.

Al profesor José Peña, Atanacio Pani, Hugo Huepa y demás personal y colaboradores del Observatorio Asotronómico Nacional de Tonantzintla, quienes me itnrodujeron al mundo de la astronomía profesional y además han sido grandes amigos.

Al Dr. César Caretta por acogerme en su casa cuando llegué a México y no tenía dónde quedarme.

A los profesores del Departamento de Astronomía de la Universidad de Guanajuato, en cuyos excelentes cursos pude formarme como astrónomo.

A mucha gente en mi Nicaragua natal, especialmente a Humberto García del Observatorio Astronómico de la UNAN-Managua, mis compañeros del grupo de astronomía Carlos Rodas y Mario Ríos, y al profesor Javier Pichardo.

A mi familia por el constante y enorme apoyo, moral y económico que hizo posible que llegara a este punto en mi vida, especialmente a mis padres María Concepción Orús y Carlos Robleto y a mi abuela Purificación Marca.

Y por último pero no menos importante, al pueblo mexicano, que a través del programa de

becas nacionales de CONACyT, posibilitó que pudiera yo culminar el sueño de estudiar una maestría en astrofísica.

A muchas otras personas que no he olvidado y han sido importantes pero que me llevaría demasiado espacio nombrar, a todos, gracias.

Resumen

En este estudio, usamos datos de espectroscopía de campo integral (IFS, por sus siglas en inglés) del censo CALIFA para estudiar regiones de galaxias que contienen Núcleos Galácticos Activos (AGN, por sus siglás en inglés), en las cuales la radiación ionizante producida por el AGN domina la ionización del gas. Seleccionamos una muestra de 18 galaxias Seyfert tipo 2. Para poder identificar las diferentes fuentes de radiación ionizante que dominan en las diferentes regiones de estas galaxias (AGN, formación estelar u otras) usamos diagramas y mapas de diagnóstico BPT (Baldwin et al. 1981). Encontramos que los límites que separan los tipos Seyfert y LINER en los diagramas BPT tradicionales necesitan ser modifacados para el caso de regiones espacialmente resueltas; proponemos nuevos límites entre estos tipos BPT para los diagramas que usan las líneas de emisión [N II] y [S II].

Definimos el *radio de influencia* R_i como la distancia desde el centro galáctico hasta el spaxel más lejano clasificado como Seyfert por los diagramas BPT. Encontramos que R_i es del orden de kiloparsecs, en algunos casos extremos, incluso sobrepasando el radio efectivo de la galaxia anfitriona. También encontramos que R_i tiene una relación directa con la tasa de acreción del agujero negro supermasivo (SMBH, por sus siglas en inglés) y a su vez es independiente de la masa de éste. Encontramos una relación de R_i con la morfología de la galaxia anfitriona, alcanzando potencialmente valores mayores de R_i en espirales tardías, especialmente en las espirales barradas, aunque con muy poca significancia estadística.

Se hizo una búsqueda de componentes desplazadas al azul en líneas de emisión para explorar la posible presencia de vientos (outflows) producidos por los AGN, los cuales introducen energía mecánica en el medio interestelar, afectando la física del gas a grandes distancias. Algunos candidatos a outflow fueron encontrados.

Abstract

In this study we use Integral Field Spectroscopy (IFS) data from the CALIFA survey to study the regions of galaxies hosting an Active Galactic Nucleus (AGN) where the gas is predominantly ionized by the AGN. We selected a sample of 18 Seyfert 2 galaxies. In order to identify the dominant sources of ionizing radiation in the different regions of these galaxies (AGN, star formation, or others) we use BPT diagnostic diagrams (baldwin1981classification), and construct maps of their spatial distribution. We found that the criteria that separates Seyfert from LINER types in the traditional BPT diagrams need to be modified for the case of spatially resolved regions, and we propose new limits for the BPT diagrams based on the [N II] and [S II] emission lines.

We define the *influence radius* R_i as the distance from the galactic centre to the furthest spaxel classified as Seyfert by the BPT diagrams. We find that in all galaxies R_i is of the order of kiloparsecs, which represents 50% or more of their effective radius, and even is larger than it in one case. We find that R_i is correlated to the accretion rate of the supermassive black hole (SMBH), but independent of its mass. Also, we find a trend of R_i to vary depending on the host galaxy morphology, getting higher the later the spiral types,especially with a bar, although with very little statistical significance.

We also searched for blue-shifted components of emission lines to detect the presence of outflows driven by AGN and found only a few candidates.

Contents

List of Figures

List of Tables

Acronyms

AGN Active Galactic Nucleus/Nuclei

BB Black Body

BLAGN Broad-Line AGN

BLR Broad-Line Region

BPT81 Bladwin, Phillips and Terlevich (diagrams)

BPT-NII BPT81 diagram using the [N II] λ6583 emission line

BPT-SII BPT81 diagram using the [S II] $\lambda\lambda 6716, 6731$ emission lines

BPT-OI BPT81 diagram using the [O I] λ6300 emission line

CALIFA Calar Alto Legacy Integral Field Area Survey

Ci10 Cid Fernandes (2010) limit between Seyfert and LINER AGN ionization in the BPT-SII

DR3 Data Release 3

DR7 Data Release 7

IFS Integral Field Spectroscopy

IFU Integral Field Unit

ISM Inter-Stellar Medium

Ka03 Kauffmann (2003) limit for minimum AGN ionization in the BPT81 diagramns

Ke01 Kewley (2001) limit for maximum starbutst ionization in the BPT81 diagrams

Ke06 Kewley (2006) statistical limit between Seyfert and LINER AGN ionization in the BPT-SII and BPT-OI diagrams

NELG Narrow-Emission-Line Galaxy

NLAGN Narrow-Line AGN

NLR Narrow Line Region

LINER Low-Ionization Nuclear Emission Region

LLAGN Low Luminosity AGN

PIZ Partially Ionized Zone

QSO Quasi-Stellar Object (quasar)

QSR Quasi-Stellar Radiosource

SDSS Sloan Digital Sky Survey

SF Star Formation/Star Forming

SMBH Supermassive Black Hole

TO Transition Object

UM Unified Model of AGN

Chapter 1

Introduction

1.1 Introduction to the Problem and Previous Studies

In the spectroscopic studies of narrow emission-line galaxies (NELGs), one important problem is to establish solid criteria to discriminate between gas ionization caused by an Active Galactic Nucleus (AGN), related to an accreting Super-Massive Black Hole (SMBH), and ionization due to OB stars in star-forming regions (Cid Fernandes et al. 2004). This problem becomes even more acute in the cases of AGN classified as transition-type objects (TOs), where star formation is relatively intense, and in Low-Ionization Nuclear Emission-Line Regions (LINERs), where the AGN is very weak.

In order to better understand the relation between AGN and their host galaxies, it is important to know the region of influence within which the ionization of the Inter-Stellar Medium (ISM) is dominated by ionizing photons from the AGN.

Influence and contributions of nuclear star forming regions to spectra of Seyfert 2 galaxies have been discussed by Cid Fernandes et al. (2004) using long-slit spectroscopy. However, this method has the difficulty of spatially separating contributions from different zones of the same object, concluding that in many cases the observed spectrum is the result of contributions both from an AGN and nuclear star formation.

Thanks to Integral Field Spectroscopy (IFS), we have a more powerful tool to address this problem. IFS allows us to populate emission-line diagnostic diagrams with thousands of *spectral pixels (spaxels)* for each individual galaxy, effectively making 2D-maps of them. Previous IFS studies were done by Sarzi et al. (2010) and Singh et al. (2013), which are from the SAURON and CALIFA collaborations, respectively in the case of LINERs, who studied radial profiles of Hβ and Hα surface brightness as well as [O III] λ5007 /Hβ and [N I] $\lambda\lambda$5197, 5200/Hβ line ratios, concluding that those profiles cannot be explained by AGN alone, but also have a contribution from the stellar component.

In this work we present an IFS study of a sample of Seyfert 2 galaxies taken from the third data release of the CALIFA survey (Sánchez et al. 2016a, from now on we will refer to this data release as CALIFA DR3), based on the single-slit spectral classification as Seyfert 2 galaxies taken from (Abazajian et al. 2009, Sloan Digital Sky Survey seventh data release, from now on, SDSS DR7). We took advantage of both the spatial and spectral resolution of the CALIFA data to estimate the influence radii, processing the spectra with the population synthesis code STARLIGHT, described in Cid Fernandes et al. (2005), in order to obtain a synthetic fit for the continuum spectrum of each spaxel and to measure the intensity of the emission lines. Maps

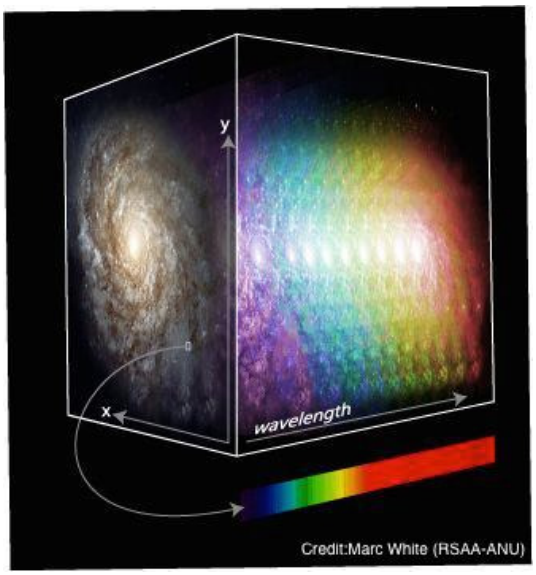

Fig. 1.1: Illustration of the spatial and spectral array in a data cube. Credits: CALIFA.

and radial profiles of emission-line ratios and diagnostic diagrams were constructed and used to estimate the influence radius.

In section 1.2, a brief introduction to the Integral Field Spectroscopy and the CALIFA survey is presented. In section 1.3 we summarize the Unified Model of AGN, which is the current paradigm that describes them. Some recent developments in this model are presented in section 1.4. In section 1.5, we describe the physics producing the emission lines in Seyfert galaxies and the diagnostic diagrams that we use.

In chapter 2 we describe our sample and in chapter 3 we explain the methodology. In chapter 4 the results of this work are presented and discussed. Finally, in chapter 5, the conclusions are summarized and some words on future research on this topic are stated.

1.2 Integral Field Spectroscopy

Integral Field Spectroscopy (IFS) is the next step in the evolution of spatially resolved spectroscopy since the multiple object optical fibre spectrometers. It consists on spatially resolved images for which each pixel contains a spectrum, so we have both spectroscopy and spatial resolution. Here pixels are called *spaxels* meaning "spectral pixels".

In IFS, the observed data is arranged as a *data cube*. Since each spaxel consists of one spectrum, which has dimension of wavelength, and has assigned an x and y coordinate for its position, we can arrange the spaxels forming a three-dimensional matrix with these three coordinates (geometrically a cube, as in figure 1.1)[1]. This allows us to obtain images in any band or wavelength that we want, within the limits of the wavelength range of the spectrometer used. This means that we can spatially resolve the spectral features (continuum, emission and absorption lines) emitted from different regions of a spatially extended object, like a galaxy or a nebula.

[1]Data cubes are stored using the FITS format, so files also include header text files with details of the instrument and the observations.

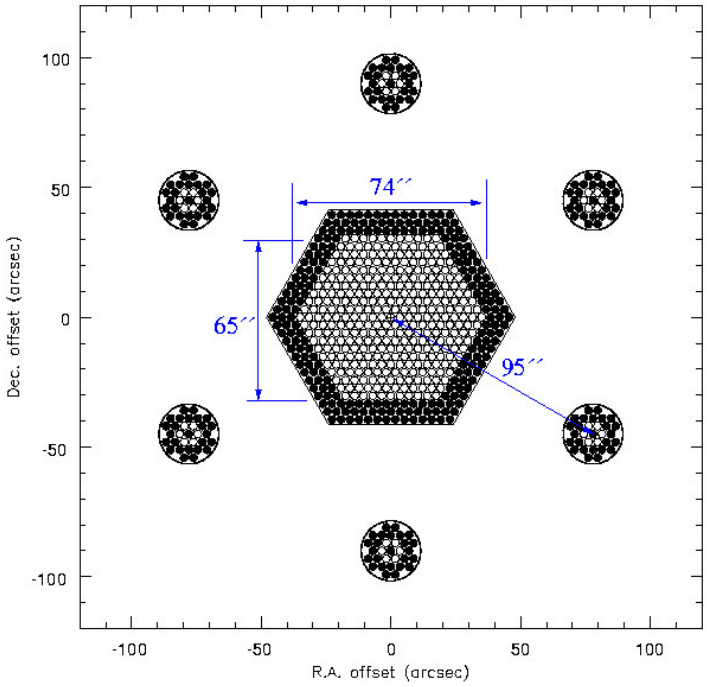

Fig. 1.2: Diagram with the physical distribution of the optical fibres and the dimensions of the sky (in arcseconds) covered by the hexagonal array of fibres of the PMAS/PPAK instrument. Credits: Centro Astronómico Hispano Alemán.

1.2.1 The CALIFA Survey

The Calar Alto Legacy Integral Field Area Survey (CALIFA) consists of publicly available IFS observations of over 600 galaxies, in the nearby Universe, that is up to redshift $z = 0.03$. They were observed with the 3.5 meter telescope at the Calar Alto Observatory in Spain. CALIFA DR3, the third and last data release, was published in April 2016 by Sánchez et al. (2016a).

The instrument used was the PMAS/PPAK spectrograph in Integral Field Unit (IFU) mode, which contains 382 optical fibres connected to a diffraction grating. 331 of these fibres form an hexagonal array used to directly observe the object of study (see figure 1.2), and the rest are used for calibration and sky background measurements. With this telescope, the array covers a *Field-of-View (FoV)* of 74" $\times$ 65". The array has a filling factor of $\approx 60\%$, due to the distance between the fibres. A technique called *dithering* was used, which consists in taking three different pointings of the same field with offsets $(0, 0)$, $(-5.22, -4.53)$ and $(-5.22, 4.53)$, all of them in arcseconds, with respect to the nominal position of the observed object, allowing to fill in the gaps and to obtain a final filling factor of 100%. The spatial sampling resolution of the final datacubes after the dithering process is 1" (distance between the centres of the spaxels).

The CALIFA survey was made using two different spectroscopic configurations for the data cubes: V500 ($R \approx 850$, $3745 - 7500$ Å) and V1200 ($R \approx 1650$, $3400 - 4840$ Å), and for some galaxies, these were combined to obtain a resulting data cube with a wider spectral range, called COMB (R variable, $3400 - 7500$ Å). Integration times were fixed to 1800 s per pointing for

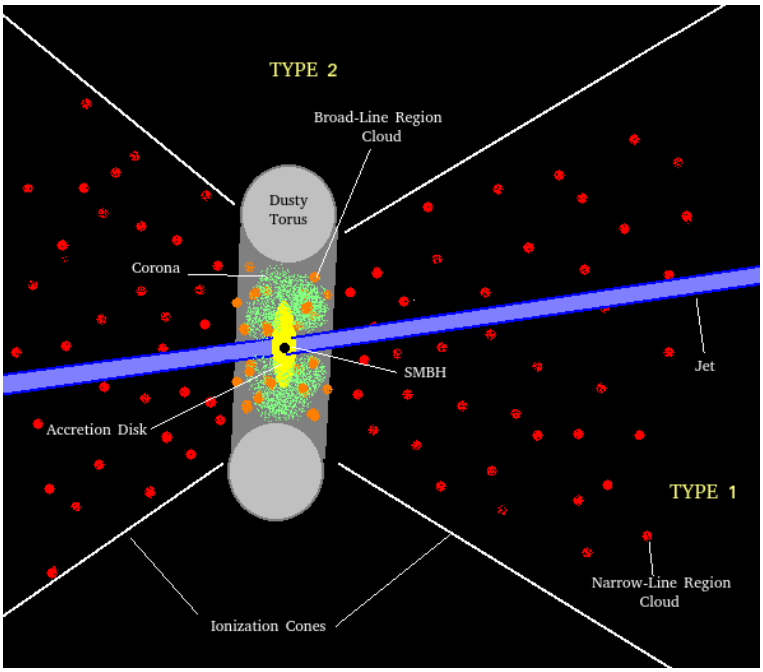

Fig. 1.3: Representation of a transverse cut of the classic UM for AGN. Each part is described in the text. The "TYPE 1" and "TYPE 2" labels mark the approximate line-of-sight that an observer would have in order to see the system as such AGN types.

V1200 and 900 s per pointing for V500. For more detailed technical information we refer the reader to Sánchez et al. (2016a).

1.3 The Unified Model of AGN

Since the 1990s, the different AGN phenomena are interpreted on the basis of the so called *Unified Model of AGN* (*UM*, see the seminal works by Antonucci 1993 and Urry & Padovani 1995). In this model, all AGN are produced by the same physical phenomenon, i.e. the accretion of matter by a SMBH. Almost all the variety of spectral features that we observe in different AGN can be explained as due to the line-of-sight orientation of the system with respect to the observer. Such is illustrated in figure 1.3, each component part being briefly described in what follows:

Super Massive Black Hole (SMBH)

A black hole with mass between the range from 10^6 to 10^{10} solar masses. They reside at the centres of almost all massive galaxies (Kormendy & Kennicutt Jr 2004; Ho 2008) and provide the necessary gravitational potential to sustain AGN accretion. Its size is defined traditionally by the *Schwarzschild radius* R_S, as the event-horizon of a non-rotating black hole (Peterson 1997; Netzer 2013):

$$R_S = \frac{2GM_{BH}}{c^2} \tag{1.1}$$

where G is the Newton gravitational constant, M_{BH} is the black hole mass and c is the speed of light. For a typical SMBH of 10^8 $M_\odot$, the Schwarzschild radius is $R_S = 3 \times 10^{13}$ cm or 10^{-2} lt-days (lightdays).

Accretion Disk

A geometrically thin, optically thick disk of gas trapped by the intense gravitational field of the SMBH, heated to temperatures of the order of 10^5 K due to gravitational contraction. This disk is considered to be the main source for the ultra violet (UV) and optical featureless continuum of AGN. Two approximations have been proposed historically to explain this continuum, at least to first order (Peterson 1997): Synchrotron emission from relativistic charged particles moving through intense magnetic fields and the sum of contributions of locally emitted thermal radiation from different parts of the disk at different temperatures. Although they can be useful as a first order approximation, both models are too simplistic to describe in detail the physics of accretion disks around SMBHs, since complex (special and general) relativistic, magnetohydrodynamical and turbulence effects should be taken into account (Netzer 2013, chapter 4, section 2).

From this accretion disk arises most of the UV and optical continuum radiation that we detect from AGN. Accretion disks emit a UV/optical continuum spectrum that follows a power-law of the form:

$$F_\nu \propto \nu^\alpha \tag{1.2}$$

where F_ν is the specific flux[2], ν is the frequency and α is the power-law index. α indicates the slope of the continuum and it is a measure of the hardness of the radiation, usually flatter ($\alpha \approx -0.5$) for the more luminous AGN, and progressively down to $\alpha \approx -1.8$ for the less luminous ones (Koski 1978; Cid Fernandes et al. 2004).

The radius R of the accretion disk is estimated by Peterson (1997) in ≈ 240 $R_S = 7.1 \times 10^{15}$ cm = 2.8 lt-days for a 10^8 $M_\odot$ SMBH, which is compatible with reverberation mapping and microlensing measurements (Mosquera et al. 2013, Mediavilla et al. 2017).

Jets

Some AGN produce a pair of jets made of highly-collimated relativistic particles, escaping away in a direction approximately perpendicular to the plane of the accretion disk, in opposite directions. They produce radiation emission, generally at radio wavelengths but also at X rays and gamma rays[3]. Radiation coming from these jets is beamed and highly polarized, which implies strong magnetic fields and charged particles moving at middle to ultra relativistic speeds. Radiation is emitted via synchrotron and synchrotron self-Compton (SSC) processes. They can reach a size of hundreds of kiloparsecs (kpc), extending well beyond their host galaxies, representing an important input of mechanical energy for the gas in galaxy clusters.

Their physics is as complicated to describe as that of the accretion disk; in fact, different models have been proposed in which both are deeply connected: thermal pressure, radiation pressure and hydromagnetic models (and many variations of them). All these models assume that jets originate in the innermost parts of the accretion disk. Coziol et al. (2017) found that jets have an origin in transient stochastic phenomena compatible with the chaotic nature of the accretion processes. For a more detailed description of AGN jets and their physics, see Netzer (2013), chapter 7, section 9 and the review by Blandford (1993).

[2]Also called monochromatic flux, F_ν is the flux emitted per unit frequency with units of [erg s^{-1} cm^{-2} Hz^{-1}].
[3]Some AGN jets can also be detected in the optical range, like in the case of the galaxy M87.

Although jets are usually well collimated, shocks are produced when they collide with the *inter-galactic medium (IGM)*, causing an expansion of the material and the generation of *hot spots* of intense radiation (Kaiser & Alexander 1997). It has been found that some of this kpc (or even Mpc) scale jets present a precession movement (Blandford 1993, chapter 4, section 5), which implies that the orientations of their accretion disks also have a precession movement. This has implications for the discussions in chapter 4.

Corona

As the accretion disk reaches high temperatures, some of the electrons and other charged particles reach high speeds and escape from the disk, getting trapped in the magnetic field around it. These particles form a very diluted cloud of plasma composed of free electrons (and some protons) at very high kinetic temperatures, of the order of 10^6 K, called the *corona*. These free electrons interact with the UV photons escaping from the accretion disk in which is known as the *inverse-Compton effect*. In such interactions, part of the energy of the high speed electrons is transferred to the photons, augmenting their energy to higher frequencies; in fact the frequency of the photons goes up from the UV to that of X rays. Part of the emitted X rays can also be scattered (reflected) back by the accretion disk (Uttley et al. 2014). The corona is the source for most X ray emission in the unresolved nuclear regions of the AGN. For more details see Peterson (1997).

X ray Reverberation mapping (Uttley et al. 2014; Kara et al. 2016) and microlensing observations have shown that the X ray emitting region has a size of $\approx 5\ R_S = 0.6$ lt-days for $10^9\ M_\odot$ SMBHs (Mediavilla et al. 2017).

Broad Line Region (BLR)

Some AGN present very broad permitted emission lines, or more precisely, a broad component of these emission lines[4]. This broadening is interpreted as due to ionized gas moving at very high velocities, corresponding to a Doppler broadening with ranges from 500 to 30000 km s^{-1}, with typical velocities of $\approx$ 5000 km s^{-1} (Peterson 1997). This ionized gas is thought to be gravitationally tied, and thus at close distance from the SMBH. Being the case, the broadening of the line profile corresponds to the gas orbital velocity range (velocity dispersion), so it can be used as a proxy to estimate the mass of the SMBH (see Netzer 2013, chapter 7, section 1.10). An analysis on the use of such proxy and the influence of other parameters like the SMBH spin can be found in Mejía-Restrepo et al. (2016).

A steady-outflow movement of this gas due to radiation pressure from the accretion disk, has been suggested, assuming a model in which this gas is in the form of clouds. This model predicts logarithmic line profiles that can explain the observations as a first order approximation (Peterson 1997 chapter 5, section 4 and references therein).

The broad components present variability in the flux with time. They vary as a response to the ionizing continuum variations, with a delay time. This allows to apply reverberation mapping techniques in order to estimate the size of the broad-line emitting region. Different emission lines vary with different delays, indicating that they are produced at different distances from the accretion disk. The size of the BLR directly depends on the central source continuum brightness, using as a proxy the continuum luminosity at 5100 Å (L_{5100}). With the approximation given in Netzer (2013), chapter 7, section 1.8, we can calculate that for an AGN with $L_{5100} = 10^{44}$ erg s^{-1}, the BLR would have a radius of $\approx 7.6 \times 10^{-3}$ pc.

[4]Given the high densities in the BLR, forbidden transitions are collisionally suppresed (Peterson 1997, chapter 5).

Narrow-Line Region (NLR) and Ionization Cones

Besides the broad components, all AGN spectra present very strong narrow emission-line components. This component is interpreted as produced by ionized gas situated at larger distances from the SMBH than that of the BLR (parsec to kiloparsec scale), and also with a slower movement (typical line widths $\approx$ 500 km s^{-1}). Such line widths are still larger than those measured in typical H II regions of starburst galaxies. Since the gas density in the NLR is lower than in the BLR, we have the presence of narrow lines both for permitted and forbidden transitions (Peterson 1997), which is important for this work, as it allows us to measure the emission lines needed for the diganostic diagrams.

The NLR is remarkable because it is the only component of AGN big enough to be spatially resolved by current telescopes. It usually has an axisymmetric morphology, and in some cases presents evidence of ionization by shocks of the outflowing plasma with the interstellar medium (apart from the dominant photoionization, see Peterson 1997, chapter 6, section 5). In some cases the NLR takes the shape of the so-called *ionization cones*: two opposite conical regions where the emission line ratios of high excitation lines such as [O III] λ5007/Hβ are higher than outside them (Peterson 1997, chapter 6, section 5) extending up to distances of hundreds of parsecs and even kiloparsecs. Thanks to this, we can produce spatially-resolved diagnostic diagrams, for which IFS isespecially useful.

Whenever ionization cones are present, there are important consequences for the evolution of the host galaxy, because in that case, kiloparsec-size regions around the nucleus have almost all the gas ionized by the AGN, which helps to suppress the existence of the adequate physical conditions for star formation (SF). Precisely these extensive regions of ionized gas are the main subject of study of the present work, in which we try to determine their extension using spatially-diagnostic diagrams (see section 1.7).

Dusty Torus and the AGN Types 1 and 2 Classification

An important amount of nuclear infrared (IR) emission, at wavelengths greater than 1 μm can be detected in AGN, which is consistent with the presence of enormous amounts of dust (Antonucci 1993 and references therein, Peterson 1997). Even more, the detection of polarized light, which can be interpreted as radiation coming from BLR emission dispersed by dust, and the presence of marked heavy-metal absorption bands in the X ray spectrum supports the hypothesis of great amounts of dust forming a torus. This dusty torus must be located at greater distances from the SMBH than the accretion disk and in a similar (if not the same) plane.

Historically, AGN have been classified as *type 1 (Broad-Line AGN, BLAGN)* or *type 2 (Narrow-Line AGN, NLAGN)*, depending on whether they present broad components in their permitted emission lines or not, respectively. The core argument of the classic UM is that type 1 AGN are those for which the line-of-sight allows direct observation of the BLR and the accretion disk continuum, and type 2 AGN are those for which the BLR is hidden from the observer by a geometrically thick dusty torus (see Netzer 2013, chapter 6, section 7). Even more, the dusty torus is also optically thick for X rays, obscuring the corona, which explains why it is hard to detect X ray emission from type 2 AGN. This means that both type 1 and type 2 AGN are really objects of the same nature and structure. This is a very powerful model as it allows to explain almost the whole variety of observed AGN (Antonucci 1993; Urry & Padovani 1995.

In the UM interpretation, this torus must be both optically and geometrically thick enough to hide the accretion disk, the BLR and the corona from an observer that is seeing the system from a direction close to the plane of the torus, who would only observe narrow lines in the spectrum, explaining the observations of NLAGN. Hence BLAGN, would be the case in which

the line-of-sight makes an angle with the plane of the torus broad enough to allow for the direct observation of the BLR, the corona and the accretion disk continuum. There is a special case for type 1 AGN in which the line-of-sight is directly pointing towards the jet. They are called *blazars*, and their observed continuum is dominated by synchrotron and SSC emission, being detected even in gamma rays.

1.4 Evolution of the UM Paradigm

Recent observations have led to consider that some improvements of the UM are necessary. We discuss here briefly two of the most important, which could be possibly related: the first involves the presence of great amounts of gas emanating from the nuclear zones (outflows) and the is related to the geometry and origin of the dusty torus.

1.4.1 AGN-Driven Outflows

Galaxy-scale winds flowing out from AGN were observed soon after de UM was proposed, but it was not until the last decade that many observations (see the multiple references in Faucher-Giguère & Quataert 2012) showed that they are more ubiquitous than previously thought. They are usually detected as shifted broad-components of emission lines in optical, millimetre, and X rays. This implies a high velocity radial movement out of the AGN (hence the name *outflow*). In order to detect them, it is necessary to separate these displaced contributions from the main emission lines in the rest frame of the galaxy (see section 3.9). Also, UV Broad-Absorption Lines (BALs) are observed in some cases.

Compared to jets, AGN-driven outflows do not show relativistic speeds, but they are usually in the order of hundreds of to thousands of km s^{-1} (although cases where they reach up to 0.1 c are not uncommon). They are not tightly collimated as the jets, and do not have prominent synchrotron radio emission, therefore they are a unrelated to jets.

Outflows are asumed to be important for galactic evolution as they can cover long distances, transporting large amounts of momentum. This means that they could quench star formation in their host galaxies, although Maiolino et al. (2017), using IFS observations, found evidence of ongoing star formation inside an outflow, produced with the ejected material.

Typical momentum flux in outflows is about 10 times greater than the radiation pressure produced by the AGN accretion disk, reaching up to 20 times in some cases (see Rupke & Veilleux 2011). Simulations by Debuhr et al. (2011) and DeBuhr et al. (2012) showed that they could be in part responsible for the $M_{BH} - \sigma$ relation through mechanisms of AGN feedback. The most accepted physical mechanism for the origin and propagation of these outflows is the ejection of gas from the accretion disk, driven by radiation pressure and shocks with the ISM. In the process, they lose energy by cooling and gain momentum while shocking the ISM, similar to the case of supernovae ejecta, but on a galactic scale. For a more detailed analytic description of the physics of the AGN-driven outflows, see Faucher-Giguère & Quataert (2012).

1.4.2 The Origin and Geometry of the Dusty Torus

As an explanation for physical processes that could explain the existence of the dusty torus, Wada (2012) proposed the so called *radiation fountain model*, in which the intense radiation pressure from the accretion disk ejects large quantities of ionized gas. This ejected material takes the geometry of two low-density, broad axisymmetric cones where radiation escapes explaining the AGN ionization cones. The gas inside these cones condensates forming filamentary structures

ionized by the intense radiation of the accretion disk, with lower density (diffuse) gas in between. These filamentary structures would account for the BLR emission and, as they drift away from the centre, they would become the NLR emitting gas. These structures, plus the part of the gas that is not condensed would form the AGN outflow. Part of this gas "rains" back over the cold accreting material far from the cones. The geometry of the cones and this returning material would shape the dusty torus into a large disk of dust and molecular gas that is able to support star formation (from one parsec to tens of parsecs in scale). This star formation produces some supernovae that have the effect of thickening the dusty disk, allowing the latter to produce the geometrical effect of obscuration of the accretion, disk depending on the line-of-sight, in the same way as the classic dusty torus does. A dusty disk of ≈ 90 pc in diameter has been directly observed in the core of NGC4261 by the *Hubble Space Telescope (HST)*, and Ruiz et al. (2001) reported a torus of up to ≈ 12 pc in radius in the Circinus Galaxy.

This model has the advantage not only to explain the angle dependence on the line-of-sight but also to predict very accurately the observed IR spectra of nearby AGN (Wada et al. 2016). According to this model, the ionization cones, the BLR, the NLR and the outflows have a common origin explained by the same physical phenomena.

1.5 Seyfert AGN and Their Spectral Features

Apart from the presence or absence of broad components in the emission-lines, AGN have been classified under other criteria, such as the radio emission (e.g. radio-loud or radio-quiet) or the luminosity. This last criterion is important to us. The most luminous AGN are *quasars (or QSOs, Quasi-Stellar Objects)*. They have usually bolometric luminosities of the order of 10^{13} $L_\odot$ (Peterson 1997). Below quasars we have Seyfert 1 galaxies, with luminosities of $\approx 10^{11}$ $L_\odot$. This luminosity comes from unresolved regions of the galactic nucleus, and it is different from the stellar luminosity of the underlying host galaxy (usually no more than $\approx 10^{11}$ $L_\odot$). The other category is that of *Low-Luminosity AGN (LLAGN)* that includes Seyfert 2 and LINER AGN. Seyfert 2 have typical luminosities of $\approx 10^9$ to 10^{10} $L_\odot$, allowing for an easier observation of the host galaxy. Finally, the less luminous are LINERs, with luminosities of $\approx 10^8$ $L_\odot$. All categories (quasars, Seyferts and LINERs) can be classified as type 1 or 2.

As we go down in luminosity, the spectral index α goes also down, making the spectra steeper and redder. This implies that the observed continuum gets contaminated with the stellar continuum, and that some features as the stellar absorption bands and lines are present. This is especially true for the continuum of type 2 Seyferts and LINERs, for which, according to the UM, the accretion disk is not in the line-of-sight and most of the continuum that we observe in the optical range comes from the stars of the host galaxy.

The most important spectral feature of any AGN in the optical range is the presence of very characteristic emission lines. In the next section we describe the emission lines used in this work.

Recombination Lines: The Hydrogen Balmer Series

These are the most common permitted emission lines found in astronomical objects and even in the diffuse ISM. They are caused by *recombination* after an ionized hydrogen atom captures a free electron. The electron is usually not captured directly into the ground level, but instead into an upper level. Since this is not a stable configuration, the electron soon begins to emit photons as it decays to lower energy levels. These transitions produce different series of emission lines at different ranges of the electromagnetic spectrum. In the optical range we can observe the

Balmer series, corresponding to photons emitted by electrons decaying from different superior levels down to level $n = 2$.

Of these lines, Hα λ6563, which is produced by an electron transitioning down from level $n = 3$ to $n = 2$, is the most prominent and the one with the least energetic photons of the series. The next line, less prominent but with higher energy photons is Hβ λ4861. Presence of these lines indicates that recombination has occurred, and that there exist photons capable of ionizing hydrogen. Hydrogen is the neutral atom with the lowest ionization potential of all (13.6 eV), marking the lower limit for ionizing photons.

1.5.1 Collisionally Excited Lines

They are produced in transitions between low-energy levels of ions or neutral atoms which have excitation potential of the order of kT, where k is Boltzmann constant and T is the (electron) kinetic temperature, which represents the mean kinetic energy of the particles of the gas (which in the ionized gas of the ISM is mainly held by free electrons). This implies that the major contribution to excitation in those states comes from the collisions of the ions with free electrons. Since radiative transitions between the mentioned states are *forbidden* by the electric-dipole selection rules, the probability for them to occur is small ($\approx 10^{-2}$ to 10^{-3} s^{-1}), and therefore are observable only in low-density environments, where the frequency of collisions with free electrons is very low and the excited ions have time to be radiatively de-excited before an electron collides with them. Such low-density environments can be commonly found in star-forming H II regions, planetary nebulae and in the NLR of AGN. For a more detailed description of the physics of collisionally-excited lines, see Osterbrock & Ferland 2006, chapter 3, section 5.

In this work, we measure the most prominent of these lines present in AGN spectra, which are used in the BPT81 diagnostic diagrams: [O I] λ6300, [S II] $\lambda\lambda$6716, 6731, [N II] λ6583 and [O III] λ5007.

1.6 Emission-Line Ratios

The presence of emission lines from different ions provides information about the physical coniditions of both the gas and the radiation field that produce these lines. We can compare the intensity of lines produced by ions that require higher ionization energies to exist (or even lines from de-excitations of neutral atoms) with those of atoms that require lower ionization/excitation energies by calculating the ratio of those intensities; that would give us information about the hardness of the ionizing radiation field[5]. If we use lines that are very close in wavelength, so they are affected by almost the same amount of reddening, we have the advantage that the line ratio will be barely or not affected at all by dust extinction.

Since hydrogen has the lower ionization potential and prominent optical emission lines, it is common to use the Balmer lines as the denominator for the optical the ratios. For the numerator we can use different lines that require ions ionized by photons of the energies that we are interested to study. For example, using low-excitation line ratios such as [N II] λ6583/Hα we can compare the amount of photons capable of singly-ionizing nitrogen (ionization potential 14.5 eV) to those capable of ionizing hydrogen (ionization potential 13.6 eV). We can have an idea of the hardness (slope) of the ionizing continuum if we use higher ionization lines, as in the [O III] λ5007/Hβ ratio, which gives compares the amount of photons capable of double-ionize O^+ into

[5]Line ratios are also affected by the physical conditions of the gas, such as temperature, density and metallicity; line ratios can be used to estimate those parameters too, see Osterbrock & Ferland (2006), chapter 5, and Peimbert et al. (2017).

O^{++} (ionization potential 35.1 eV) to that of photons capable of ionize hydrogen; in this case we use Hβ in the denominator because it is closer to the wavelength of the numerator line than Hα and thus is the ratio is less affected by reddening.

1.7 Diagnostic Diagrams

Line ratios alone cannot establish which is the nature of the source of ionization in galaxies, although they can reveal important aspects of it. The combination of different line ratios forming the so-called *diagnostic diagrams*, can give us a more complete vision.

1.7.1 BPT81 Diagrams

Baldwin et al. (1981) proposed a set of diagnostic diagrams that separate emission-line galaxies by the dominant source of ionizing radiation. For this purpose, various combinations of emission-line ratios were tested, leading into conclusion that the most efficient are the combinations of the high-ionization line ratio $\log_{10}$([O III] λ5007/Hβ), versus any of these three other low-excitation line ratios: $\log_{10}$([N II] λ6583/Hα), $\log_{10}$([S II] $\lambda\lambda$6716, 6731/Hα) and $\log_{10}$([O I] λ6300/Hα). From now on, we will call these diagnostic diagrams BPT-NII, BPT-SII and BPT-OI respectively (and BPT81 collectively).

In these diagrams (figure 1.4), star-forming (SF) galaxies (for which the main ionization source are young OB stars) are located typically in the left side (low values of the low ionization line ratios), forming a sequence, descending continuously from high to low values of the $\log_{10}$ ([O III] λ5007/Hβ) line ratio, reaching a limit where the value of the low-ionization ratio saturates, which is the maximum value that stars can achieve, given their steep black-body ionizing continuum and luminosity, limited by their mass (Kewley et al. 2001). For the high-excitation line ratio, in the case of (SF) regions, the decreasing behaviour of $\log_{10}$([O III] λ5007/Hβ) with increasing $\log_{10}$([N II] λ6583/Hα) is, instead, more related to the metallicity, which is lower for high values of $\log_{10}$ ([O III] λ5007/$H\beta$) and increases toward lower values of this line ratio (see Kewley et al. 2001 and Osterbrock & Ferland 2006, chapter 12).

If the main ionization source is an AGN, the situation is different. Due to the high intensity and hardness of the produced ionizing continuum, AGN have very extended *partially ionized zones (PIZs)* from where the collisional emission lines arise. This allows for the low-ionization line ratios to reach high values beyond the limit achievable by stars, with the effect of AGN being located towards the right side of the diagram. Such large values of the $\log_{10}$([O I] λ6300/Hα) and $\log_{10}$([S II] $\lambda\lambda$6716, 6731/Hα) line ratios are indicators of a large PIZ produced by high-energy photoionization (Osterbrock & Ferland 2006, chapter 12). Since the PIZs in SF regions are much smaller (Osterbrock & Ferland 2006, chapter 2) they remain in the left side of the diagram, and we can use these line ratios to roughly identify the main radiation source as an AGN or as SF regions.

In summary, SF galaxies are located in the left side and AGN are located in the right side the BPT81, in a distribution that somehow remembers the shape of a flying seagull or the letter V. This V shape is more evident in the BPT-NII diagram, but BPT-SII and BPT-OI diagrams show also an important and very useful difference: in these diagrams, the right sequence is clearly divided into two branches: the upper one with higher values of $\log_{10}$ ([O III] λ5007/Hβ) and the lower one with lower values of this line ratio. Those two groups respectively correspond to the Seyfert and LINER AGN.

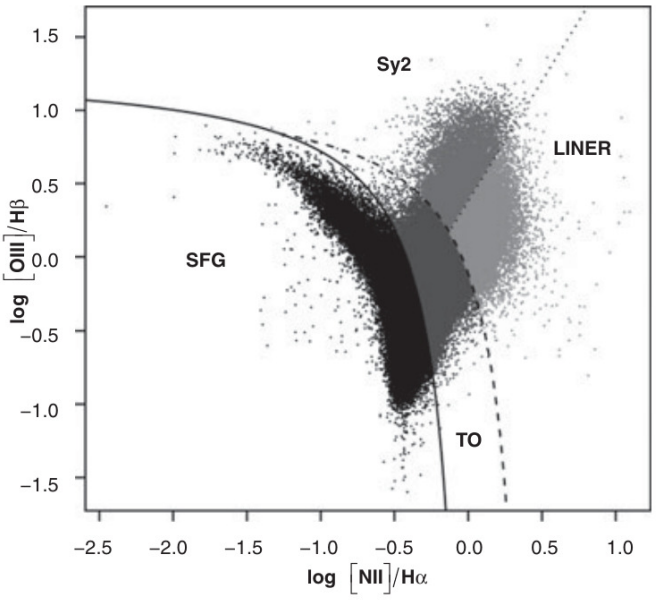

Fig. 1.4: Example of a BPT-NII diagram. Each point is a galaxy from the SDSS DR7, including 256 510 of them. The diagram is divided in different zones; the location of each data point indicates the ionization source dominating the spectrum of its galaxy(SFG: Star Forming Galaxy, Sy2: Seyfert 2, TO: Transition Object, LINER: Low-Ionization Nuclear Emission Region. The limits that determine each zone are explained in the text: the solid line is the Ka03 limit, the dashed line is the Ke01 maximum starburst line and the dotted line is the limit proposed by Torres-Papaqui et al. (2012) between LINER and Seyfert AGN. Credit: Figure 1 (b) from Ortega-Minakata et al. (2014).

The $\log_{10}([\text{O III}]\ \lambda 5007/\text{H}\beta)$ ratio is an indicator of temperature and of the mean level of ionization (Osterbrock & Ferland 2006, chapter 12, section 1). It is much more sensitive to the presence hard photons and differentiates better between the harder continuum of a Seyfert AGN and the softer one of a LINER AGN (although it cannot differentiate SF galaxies from AGN, since young stars can also produce high values of this ratio).

Therefore, it is the combination of both low-excitation and high-ionization line ratios used by the BPT81 diagnostic diagrams that allows us to distinguish between the different ionization sources (activity) of emission-line galaxies (SF, Seyfert AGN or LINER AGN). It is important to notice that, since the high values of low-excitation line ratios can also be produced by shocks, the BPT81 diagrams cannot distinguish extended AGN photoionized PIZs from those due to shock ionization, and other tracers or diagnostics are needed in order to be able to separate them.

1.7.2 Limits Between Ionization Sources in the BPT81 Diagrams

It becomes necessary to trace clear limits between the different zones of the BPT81 diagrams dominated by different ionization sources. In this section we briefly describe the most used in the literature.

The Kewley 2001 line: SF-AGN limit

The most commonly used limit between SF galaxies and AGNs is the one proposed by Kewley et al. (2001). They produced photoionization models for *StarBurst Galaxies (SBG)* from evolutionary tracks of stellar populations, accounting for reddening and mass loss. As a result they were able to reproduce the left wing of the BPT81 diagrams, marking limits of the zones of maximum excitation that star formation can produce (the saturation limit mentioned before). This limit is known as the *Kewley (2001)*, abbreviated as Ke01, or *maximum starburst line*. For the different BPT81 diagrams, the Ke01 limits between SF and AGN are:

$$\log_{10}\left(\frac{[\mathrm{O\ III}]}{\mathrm{H}\beta}\right) = \frac{0.61}{\log_{10}\left(\frac{[\mathrm{N\ II}]}{\mathrm{H}\alpha}\right) - 0.47} + 1.19 \tag{1.3}$$

$$\log_{10}\left(\frac{[\mathrm{O\ III}]}{\mathrm{H}\beta}\right) = \frac{0.72}{\log_{10}\left(\frac{[\mathrm{S\ II}]}{\mathrm{H}\alpha}\right) - 0.32} + 1.30 \tag{1.4}$$

$$\log_{10}\left(\frac{[\mathrm{O\ III}]}{\mathrm{H}\beta}\right) = \frac{0.73}{\log_{10}\left(\frac{[\mathrm{O\ I}]}{\mathrm{H}\alpha}\right) + 0.59} + 1.33 \tag{1.5}$$

for the BPT-NII, BPT-SII and BPT-OI respectively.

The Kauffman 2003 line: SF-TO limit

Kauffmann et al. (2003) revised the properties (emission-line ratios and stellar populations) of 55 757 galaxies from SDSS. They found a significant overlap of the line ratios from the AGN population with those of SBGs. That means that some AGN are hosted by SBGs, showing properties of both types of objects in their spectrum. These are called *composite* or *Transition Objects (TOs)*. Although some of their properties are not properly understood yet (see the review on LLAGN by Ho 2008).

Kauffmann et al. (2003) traced the lowest ionization limit (abbreviated as Ka03) reached by the TOs, meaning that they found no AGN with lower ionization than that limit (that is for the SDSS sample, but it is a big sample with consequently very good statistics). Therefore, TOs are defined as the objects between both the Ka03 line of minimum AGN ionization and the Ke01 line of maximum starburst ionization. This line has only been defined for the BPT-NII diagram. The equation for the Ka03 line is:

$$\log_{10}\left(\frac{[\mathrm{O\ III}]}{\mathrm{H}\beta}\right) = \frac{0.61}{\log_{10}\left(\frac{[\mathrm{N\ II}]}{\mathrm{H}\alpha}\right) - 0.05} + 1.3 \tag{1.6}$$

Kewley 2006 line: Seyfert-LINER limit

Kewley et al. (2006) took advantage of the large number of spectra taken by SDSS, and constructed BPT diagrams for over 200 000 galaxies. This allowed for a continuous and clearer distribution of the galaxies in the different parts of each diagram. They noticed that there was a lower density of galaxies populating the zone between Seyferts and LINERs in the right wing of the BPT-SII and BPT-OI diagrams. They made histograms of the density of galaxies along concentric circular segments at different distances from the inflection point of the distribution and made a linear fit to the minimum points of these histograms, resulting in a line that

effectively separated both Seyfert and LINER populations. This line is called the Ke06 line. The corresponding equations are:

$$\log_{10}\left(\frac{[\text{O III}]}{\text{H}\beta}\right) = 1.89\log_{10}\left(\frac{[\text{S II}]}{\text{H}\alpha}\right) + 0.76 \tag{1.7}$$

$$\log_{10}\left(\frac{[\text{O III}]}{\text{H}\beta}\right) = 1.18\log_{10}\left(\frac{[\text{O I}]}{\text{H}\alpha}\right) + 1.30 \tag{1.8}$$

for the BPT-SII and the BPT-OI respectively.

Cid Fernandes 2010 line

Cid Fernandes et al. (2010) transposed the Ke06 lines for the BPT-OI and BPT-SII to the BPT-NII diagram, using statistics for the SDSS galaxies. The result is the Ci10 limit between Seyferts and LINERs for the BPT-NII diagram:

$$\log_{10}\left(\frac{[\text{O III}]}{\text{H}\beta}\right) = 1.01\log_{10}\left(\frac{[\text{N II}]}{\text{H}\alpha}\right) + 0.48 \tag{1.9}$$

1.7.3 The BPT81 Diagrams in the IFS era

The BPT81 diagrams have been widely applied to IFS data ever since the surveys like CALIFA and SAMI began to produce results. For traditional longslit/fibre spectroscopy, alternative limits can be found in literature. Torres-Papaqui et al. (2012) proposed a dividing line between Seyfert 2 and LINERs, defined as the line that splits a sample of ambiguous types from SDSS DR7 in two groups of the same number of galaxies.

In general, it has been just assumed that the same limits described above, developed for non-spatially resolved spectroscopic data also apply for spatially resolved regions within the same galaxy [6]. As we shall show in chapter 3, this appears not be the case and some modifications to the BPT81 limits are needed, especially for the limit between Seyfert and LINER-type spaxels. Sharp & Bland-Hawthorn (2010) used IFS observations of two galaxies to trace "tracks" on the BPT-NII following the bulk of data points of one galaxy with dominant AGN photoionization and one galaxy with dominant shock ionization. This is a first effort to establish limits between Seyfert and LINERs for IFS data. Nevertheless, since it is based only on two galaxies, one for each track proposed, we consider that it could not be representative of the Seyfert 2 population.

We propose a new limit to distinguish between Seyfert and LINER-like spaxels in the BPT-NII and BPT-SII diagrams, to substitute the Ci10 and Ke06 lines for Seyfert IFS datacubes. The methodology, based in our sample of 18 galaxies, is explained in section 3.7 and results are shown and discussed in section 4.2.1.

[6] It is important to remark that of all the limits mentioned above, the Ke01 is physically motivated, while the Ka03, Ke06 and Ci10 limits are based on pure empirical statistics.

Chapter 2

Sample

For our study, we use a sample of Seyfert 2 AGN. They have some advantages over quasars when we want to study the spatially resolved properties of their host galaxies: as Seyferts are less luminous, images are not saturated by the nuclear radiation, and the structure of the host galaxies can be easily observed. Also since even 3C273, which is the nearest quasar, is at redshift $z = 0.15$ (Strauss et al. 1992), the spatial resolution that we would obtain with IFS would not be enough for our purposes, even if the host galaxy was observed.

The CALIFA survey is the legacy IFS survey with the best spatial resolution to date, combined with a spectral range that allows to measure the most important optical emission lines. The CALIFA survey, that goes only as deep as redshift $z = 0.03$, includes no quasars nor blazars. Also, despite being LLAGNs, Seyfert 2 (Ho 2008) have high enough values of their line ratios to avoid controversy about their AGN nature.

CALIFA DR3 observed 19 galaxies with a Seyfert 2 nucleus, as classified by SDSS DR7 (see Sánchez et al. 2016b and the CALIFA DR3 dataproducts). Of these 19, we discarded UGC04145, because the datacube presented serious consistency problems. Table 2.1 lists the 18 galaxies finally selected for this work, their spectroscopic configuration available with the CALIFA DR3, their J2000 coordinates, their SDSS spectroscopic redshift, their effective radius (both in arcsec and kpc, determined by the CALIFA collaboration from SDSS r filter images) and their morphological classification by the CALIFA collaboration, the last two taken from the CALIFA DR3 data products.

NGC5216 is classified as Seyfert 1 in the catalogue by Véron-Cetty & Véron (2006). Since the UM explains both Seyfert 1 and 2 as the same kind of objects that only differ because of the observers line-of-sight, the main difference between them (apart from the line-broadening) should be the observed continuum of the nuclear region, which comes mainly from the accretion disk in the case of Seyfert 1 and is contaminated by the stellar continuum in the case of Seyfert 2 (see section 1.3). Given that we are using diagnostic diagrams based only on the emission lines, covering spatially resolved regions far larger than the nucleus (the only region where we could find BLR emission) the combination of type 1 and 2 AGN in our sample should not significantly affect our results, hence we keep NGC5216 in our sample, despite its ambiguous classification in the literature.

In Appendix A, figure A.1 shows images of the galaxies of the sample taken by SDSS DR7. All images have the same size of 80" $\times$ 80", comparable to the CALIFA datacubes field of view.

Galaxy	Right Ascension (J2000.0)	Declination (J2000.0)	Spectroscopic Configuration	Redshift (SDSS)	Effective Radius (arcsec)	Effective Radius (kpc)	Morphology (CALIFA)
IC0485	08h00m19.765s	+26d42m05.19s	COMB	0.0277 ± 0.00012	36.491	19.5	SBab
IC0540	09h30m10.330s	+07d54m09.90s	COMB	0.0069 ± 0.00019	22.287	2.71	SBab
IC2247	08h15m59.098s	+23d11m58.65s	COMB	0.0144 ± 0.00019	24.006	6.76	Sab
IC4215	13h16m16.830s	+25d24m18.79s	V500	0.0129 ± 0.00018	16.516	3.99	Sb
MCG-02-02-030	00h30m07.307s	−11d06m49.11s	COMB	0.0117 ± 0.00016	17.747	3.94	SBb
MCG-02-08-014	02h52m23.395s	−08d30m37.49s	V500	0.0167 ± 0.00016	26.836	8.62	Sa
NGC0681	01h49m10.829s	−10d25m35.13s	COMB	0.0058 ± 0.00017	34.706	3.53	SBa
NGC2410	07h35m02.260s	+32d49m19.60s	V500	0.0155 ± 0.00016	27.156	8.19	SBb
NGC2916	09h34m57.602s	+21d42m18.97s	COMB	0.0124 ± 0.00016	28.558	6.91	Sbc
NGC3160	10h13m55.074s	+38d50m34.23s	V500	0.0228 ± 0.00016	18.301	8.02	SBab
NGC3182	10h19m33.023s	+58d12m20.61s	V500	0.0070 ± 0.00017	24.765	3.02	E7
NGC4644	12h42m42.657s	+55d08m43.85s	COMB	0.0164 ± 0.00016	19.417	6.24	Sb
NGC5216	13h32m06.892s	+62d42m02.51s	COMB	0.0098 ± 0.00018	29.533	5.38	E0
NGC5378	13h56m51.016s	+37d47m50.08s	COMB	0.0100 ± 0.00016	29.386	5.35	SBb
NGC5957	15h35m23.214s	+12d02m51.36s	COMB	0.0061 ± 0.00016	28.997	2.95	SBb
NGC5971	15h35m36.892s	+56d27m42.07s	COMB	0.0112 ± 0.00016	24.009	4.85	SBb
NGC6394	17h30m21.420s	+59d38m23.57s	COMB	0.0284 ± 0.00009	25.551	14.1	SBbc
UGC09110	14h14m13.398s	+15d37m20.67s	V500	0.0155 ± 0.00016	24.512	7.39	SBb

Table 2.1: List of Seyfert 2 galaxies selected from the CALIFA DR3.

Chapter 3

Methodology

3.1 Extraction of the Datacubes

All CALIFA datacubes are in FITS format. This "cubic"arrangement (see section 1.2) has the advantage that we can plot spatially resolved maps at any wavelength covered by the spectrum, as if we were obtaining filter photometry at any wavelength within the observed spectral range, and we may integrate them in either narrow or broad wavelength intervals. We used these data to create luminosity maps for various emission lines (see section 3.6).

The data were already reduced and calibrated by the CALIFA collaboration. The extraction of the spectra was done using scripts developed by the *Guanajuato Integral Field Unit Group (GIFU group)*, specifically in order to prepare automatically the data in a way that it can be used as an input for the STARLIGHT code (Cid Fernandes et al. 2005), which is described in the next section. As we have thousands of spectra per datacube, it is important to fully automatize the process with a script that loops over all spectra.

3.2 STARLIGHT: Spectral Synthesis

Each galaxy datacube was analysed with the *STARLIGHT spectral synthesis code* described in Cid Fernandes et al. (2005). This is the fifth version of this code, obtained by private communication with the author. It is very similar in general to the publicly available fourth version. Here we describe briefly the methods that it uses.

STARLIGHT adds different template spectra to create a model that fits an observed spectrum. These templates are usually synthetic spectra of stellar populations of different ages and metallicities. Also, any template can be used to fit spectra of individual stars or galaxies, according to the necessities of the project. In our case we used a base of templates of spectra of star populations with 25 different ages and 6 metallicities from Asari et al. (2007), for a total of 150 template spectra. These spectra are called *Simple Stellar Populations (SSP)*, since they are representative of stars of the same age and metallicity (like those born inside the same stellar cluster). A set of SSP that we use as templates is called a *base*.

This is how STARLIGHT works: we have an observed spectrum O_λ and the base with a set of N_* spectra. We want to obtain a model of the observed spectrum that is a sum of the contribution of the different populations in the base, each one contributing with a *light fraction* at a certain wavelength λ_0 (which is used to normalize the flux). The model M_λ is then:

$$M_\lambda = \sum_{j=1}^{N_*} L^0_{\lambda j} \otimes G(v_*, \sigma_*) 10^{-0.4 A_{\lambda j}} \tag{3.1}$$

where $L^0_{\lambda j}$ is the normalized luminosity, flux or intensity of the population j at wavelength λ, $A_{\lambda j}$ accounts for dust extinction, and $G(v_*, \sigma*)$ is a Gaussian filter to account for the kinematic effects of velocity shift v_* and velocity dispersion σ_*. STARLIGHT varies randomly the contribution of the different SSP in the base, and performs a combination of Metropolis and Markov Chain algorithms to search for the parameter space that minimizes the χ^2 merit figure:

$$\chi^2 = \sum_\lambda [(O_\lambda - M_\lambda) w_\lambda]^2 \tag{3.2}$$

where w_λ is a statistical weight assigned for a given λ, in case one wants to fit better certain features. For more details we direct the reader to the STARLIGHT manual, which can be downloaded at `http://www.starlight.ufsc.br/node/2` and to Cid Fernandes et al. (2005). As this is a random process, the computation time varies. For each spaxel from CALIFA datacubes it usually takes less than 20 minutes, and around three to four weeks to complete a datacube[1]. As a result, we obtain the best fit of M_λ with the light fraction corresponding to the contribution of each stellar population and the sum of them all in the form of a synthetic spectrum. We can use this spectrum as a template for the stellar continuum, substracting it from the observed one to obtain a pure-emission spectrum and obtain a better measurement of the emission lines (see section 3.3).

3.2.1 Previous Preparation of Data for STARLIGHT

We need to prepare the spectra and feed STARLIGHT with some information, which we do with scripts developed by the GIFU group to automatize the process, as we have literally thousands of spectra per datacube. First of all, our observed spectrum must be re-sampled to a resolution of 1 Å with integer values for λ. We also must mask out all possible emission features present, as STARLIGHT fits star-like spectra and, with the exception of young massive Be stars and Wolf-Rayet, stars do not show emission lines. STARLIGHT fits the continuum and stellar absorption features, such as the H and K lines of Ca II, and the presence of emission lines would introduce large errors into the final result. For this work, the masked regions of the spectrum are shown in table 3.1.

A statistical weight w_λ can be given to certain wavelengths in where there are absorption or continuum features, which are very dependent on stellar age and metallicity. We gave a statistical weight of 2 to the absorption features Ca II K line, a powerful indicator of stellar age and to the G absorption band, very dependent on stellar metallicity. Although STARLIGHT does not care if we use flux, intensity or luminosity units for our spectra, the bases must have this same units, and it is important to note that CALIFA uses the specific surface flux[2], with units of [erg s^{-1} cm^{-2} $Å^{-1}$ $arcsec^{-2}$], multiplied by a factor of 1×10^{16}, so we have to multiply by 1×10^{-16} to recover the real value of the specific surface flux in the mentioned units.

[1] With an Intel i5 quadruple-core processor and 8 GB of RAM.

[2] The specific surface flux has similar units to specific intensity, using $arcsec^2$ instead of steradians for the solid angle, which is convenient in this case as each spaxel from the CALIFA datacubes covers 1 $arcsec^2$ in the sky. In order to convert this specific surface flux to specific intensity we should divide by the number of steradians in one $arcsec^2$, that is $2.3504430539097885 \times 10^{-11}$. Unless otherwise specified, we will keep using specific surface flux units along this document.

Table 3.1: Regions masked out of the spectra for the STARLIGHT continuum fit and their corresponding emission lines. The He I λ5876 masked region, also masks the Na D band absorption by the interstellar medium, centered at ≈ 5890 $\mathring{A}$.

Emission Lines	Masked Spectral Range ($\mathring{A}$)
[O II] $\lambda\lambda 3726, 3729$	$3710.0 - 3744.0$
[Ne III] $\lambda 3869$	$3858.0 - 3880.0$
Hϵ $\lambda 3970$	$3960.0 - 3980.0$
Hδ $\lambda 4102$	$4092.0 - 4112.0$
Hγ $\lambda 4340$	$4330.0 - 4350.0$
Hβ $\lambda 4861$	$4848.0 - 4874.0$
[O III] $\lambda\lambda 4959, 5007$	$4940.0 - 5028.0$
He I $\lambda 5876$	$5866.0 - 5916.0$
[O I] $\lambda 6300$	$6280.0 - 6320.0$
[N II] $\lambda\lambda 6548, 6583$ and Hα $\lambda 6563$	$6528.0 - 6608.0$
[S II] $\lambda, \lambda 6717, 6731$	$6696.0 - 6752.0$

3.3 Emission Line Measurements

We measured the parameters of some emission lines in the spectra which are necessary to produce maps and profiles of emission lines luminosity, line ratios and diagnostic diagrams. This was done using scripts developed by the GIFU Group, that fit Gaussians to the emission lines. For this we used the synthetic spectrum generated by STARLIGHT as a reference level for the continuum, in order to subtract the stellar continuum from the observed spectrum, to get only the pure-emission spectrum (see figures 3.1 and 3.2). The Gaussian parameters of interest are: the Full Width at Half Maximum (FWHM), the standard deviation σ, the integrated specific surface flux (integral of the specific surface flux under the Gaussian), the equivalent width (EW), and signal-to-noise ratio (SNR) of the line and of the adjacent continuum. The process is automatized so the script fits all the spaxels from a datacube automatically, taking the data directly from each of the STARLIGHT output files for each spaxel. The fitted Gaussian is in the form:

$$F_\lambda(\lambda) = \frac{F_\lambda}{\sigma\sqrt{2\pi}} \exp - \frac{(\lambda - \mu)^2}{2\sigma^2} \tag{3.3}$$

where $F_\lambda(\lambda)$ is the specific surface flux at each wavelength λ in units of [erg s^{-1} cm^{-2} Å^{-1} arcsec^{-2}], F_λ is the integrated surface flux of the Gaussian in units of [erg s^{-1} cm^{-2} arcsec^{-2}], μ is the mean or centre, and σ is the standard deviation in Å. Only spaxels with SNR ≥ 3 in the four emission lines included in each BPT81 diagram are selected to construct the maps. For the kinematic maps, only spaxels with SNR ≥ 3 in Hα are selected.

3.4 Visual Inspection

A visual inspection of the spectrum of some spaxels of each galaxy was done in order to assess the quality of the data and to confirm the Seyfert 2 characteristics of the spectra (the presence

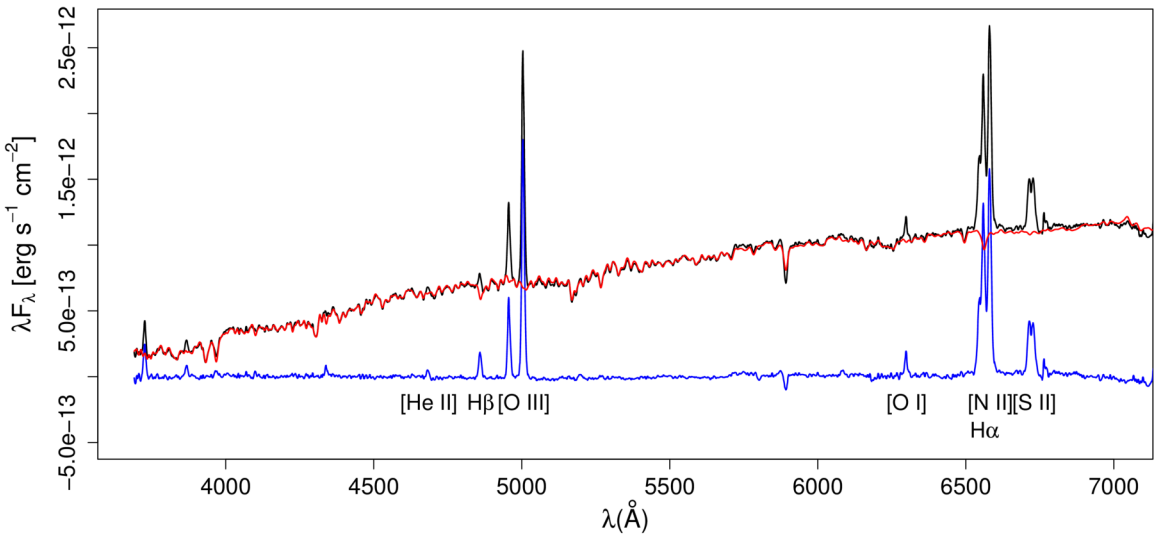

Fig. 3.1: An example of a spectrum from one of the central spaxels of NGC2410 with intense narrow emission lines characteristic of Seyfert 2 AGN. The black line is the observed spectrum, the red line is the synthetic stellar continuum model fitted with STARLIGHT, and the blue line is the resulting pure-emission spectrum after subtracting the model from the observed spectrum. Some prominent emission lines are indicated.

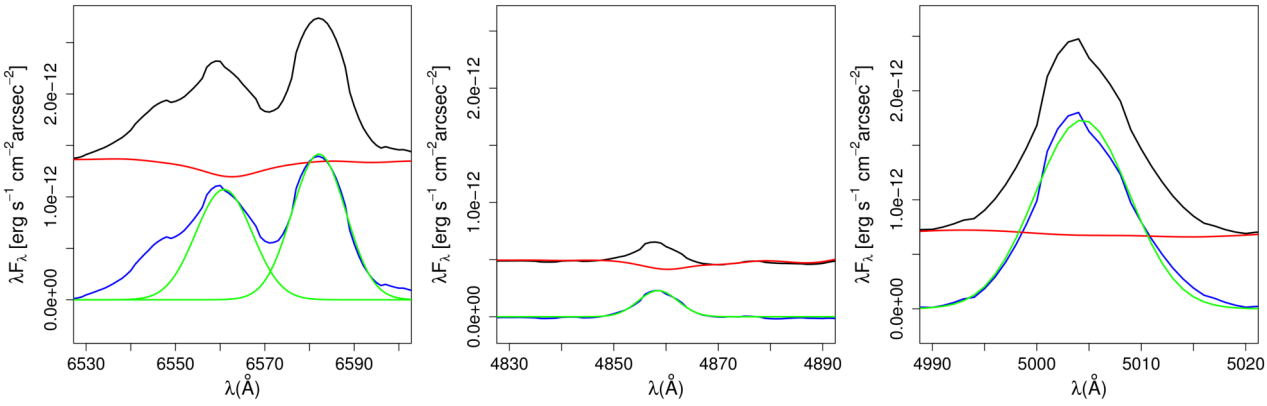

(a) (b) (c)

Fig. 3.2: Examples of emission-line Gaussian fits for one of the central spaxels of NGC2410. The black line is the observed spectrum, the red line is the STARLIGHT synthetic continuum, the blue line is the pure-emission residual spectrum after subtracting the synthetic spectrum from the continuum and the green lines are the fitted Gaussians. (a) Hα and [N II] λ6583 (b) Hβ and (c) [O III] λ5007.

of high excitation prominent emission lines in the nuclear spaxels). This inspection revealed that UGC04145 had unreliable spectra, and as stated before, we discarded it from the sample.

A visual inspection of SDSS images and the literature also reveals that NGC5216 is an interacting galaxy, part of the Arp104 pair, connected by a tidal bridge of stars and material with the spiral NGC5218. We will discuss the peculiarities of this system in more detail in section 4.1.

3.5 Dereddening

For each measured emission line , dereddening was applied using the equations from Cardelli et al. (1989) with $R_V = 3.1$ (using scripts developed specifically for this work) to obtain the V-band normalized extinction law f_V, then we renormalized the fluxes relative to Hβ to obtain the flux ratio using the following equation:

$$\frac{F_{\lambda 0}}{F_{H\beta 0}} = \frac{F_\lambda}{F_{H\beta}} 10^{c(H\beta)\ [f_{H\beta}(\lambda)-1]} \tag{3.4}$$

where $F_{\lambda 0}/F_{H\beta 0}$ is the dereddened ratio of the flux at wavelength λ to that of $H\beta$, $F_\lambda/F_{H\beta}$ is the ratio of the observed flux of those lines, $f_{H\beta}(\lambda)$ is the extinction law at λ, normalized to that of $H\beta$, and $c(H\beta)$ is a normalization constant determined assuming the ratio of $F_{H\alpha 0}/F_{H\beta 0}$ to be equal to 2.86 (Brocklehurst 1971) given by:

$$c(H\beta) = \frac{\log_{10} 2.86 - \log_{10}\left(\frac{F_{H\alpha}}{F_{H\beta}}\right)}{\frac{f_\alpha}{f_\beta} - 1} \tag{3.5}$$

where f_α and f_β are the values of the Cardelli et al. (1989) extinction law for Hα and Hβ respectively. By convention, the resulting value of $F_{\lambda 0}/F_{H\beta 0}$ is multiplied by 100. The values obtained for the extinction law were double-checked with those in López-Sánchez et al. (2011).

For the uncertainties determination, we assumed an error on flux calibration plus line fitting of 7%, as found by Catalán-Torrecilla et al. (2015) for the CALIFA galaxies, and propagated from there as follows:

The uncertainty on the determination of the normalization constant $c(H\beta)$ is:

$$\sigma^2_{c(H\beta)} = \left[-\frac{1}{F_{H\alpha}\left(\frac{f_\alpha}{f_\beta}-1\right)\ln 10}\right]^2 \sigma^2_{F_{H\alpha}} + \left[-\frac{1}{F_{H\beta}\left(\frac{f_\alpha}{f_\beta}-1\right)\ln 10}\right]^2 \sigma^2_{F_{H\beta}} \tag{3.6}$$

Then we propagate to the uncertainty in the dereddened and normalized surface specific flux $\frac{F_{\lambda 0}}{F_{H\beta 0}}$:

$$\sigma^2_{\frac{F_{\lambda 0}}{F_{H\beta 0}}} = \left[\frac{10^{c(H\beta)\left(\frac{f_\lambda}{f_\beta}-1\right)}}{F_{H\beta}}\right]^2 \sigma^2_{F_\lambda} + \left[-\frac{F_\lambda 10^{c(H\beta)\left(\frac{f_\lambda}{f_\beta}-1\right)}}{(F_{H\beta})^2}\right]^2 \sigma^2_{F_{H\beta}} + \left[\frac{F_\lambda\left(\frac{f_\lambda}{f_\beta}-1\right)\ln(10)10^{c(H\beta)\left(\frac{f_\lambda}{f_\beta}-1\right)}}{F_{H\beta}}\right]^2 \sigma^2_{c(H\beta)} \tag{3.7}$$

After this, provisional BPT-NII diagrams were plot. The resulting spaxels classified as Seyfert were dereddened (again from non-dereddened data) with a value of $F_{H\alpha 0}/F_{H\beta 0} = 3.1$, more appropriate in the case of AGN (Osterbrock & Ferland 2006). As a byproduct, a manual (in Spanish) was written explaining this procedure; it is included in appendix B. Since we are dealing here with spatially resolved regions instead of whole galaxies, we have to be careful to use the adequate value of $F_{H\alpha 0}/F_{H\beta 0}$ for each spaxel. The mean difference in the resulting dereddened flux between using those values in our sample is $\approx 0.8\%$. This procedure was implemented in all the scripts developed specifically for this work.

3.6 Construction of Maps

One of the advantages of working with IFS is that we have the spatial distribution of the light emitted by an object, allowing us to construct maps of the spatial distribution of the different spectral features and derived physical properties and diagnostics. We use this kind of maps as our main analysis tool, therefore, special care was taken in the details of their correct construction. In the present section we describe all the steps, procedures and corrections needed to adequately elaborate the different maps we used.

3.6.1 Determination of centres, inclinations and position angles.

In order to determine R_i, we need a reference central point to measure them, i.e. the centre of each galaxy, assumed as the position of the SMBH. Also this centre, plus the inclination and the position angles are needed to correctly deproject the maps (see section 3.6.2) and measure distances inside the galaxies. The CALIFA collaboration established these parameters for their sample, using photometry in the r band from SDSS DR7 images. We need to be sure that the centres are well determined at least to an accuracy of 1 arcsecond (our angular resolution). Another commonly used method to determine galactic centres is the kinematic method (using the rotation velocity maps and sometimes the velocity dispersion maps).

Both photometric (stellar) and kinematic (gas) determinations should produce the same results, although this is not always true in practice. As it was found by Palunas & Williams (2000), usually photometric determinations give a better fit for the position of the centre and the inclination angle, while the kinematic method gives a better fit for the position angle. Barnes & Sellwood (2003) found that the position angle is poorly determined by photometric methods when the inclination angle is low (face-on galaxy), but agrees better with kinematic measurements when the inclination angle is high (edge-on galaxy), because in that case non-axisymmetric structures such as bars and spiral arms have a less prominent effect on photometric determinations. Some systematic uncertainties that affect the photometric method, as listed by Barnes & Sellwood (2003) are:

1. Seeing
2. Dust obscuration.
3. Finite disk thickness.
4. Non-axisymmetric features of the disc (bars, spiral arms).
5. Intrinsic ellipticity of the disc.

Table 3.2: Minor to major axis ratio (B/A), position angles and inclination angles for the galaxies in the sample. The former two were photometrically determined by the CALIFA collaboration from SDSS images (CALIFA DR3 dataproducts), the latter was determined for this work.

Galaxy	B/A	Postion Angle (deg)	Inclination Angle (deg)
IC0485	0.40598	-31.54314	66.04745
IC0540	0.30456	170.31782	72.26831
IC2247	0.18383	-32.11959	79.40707
IC4215	0.36458	48.20037	68.61826
MCG-02-02-030	0.34269	163.97014	69.95915
MCG-02-08-014	0.38021	96.84196	67.65331
NGC0681	0.65278	69.77192	49.24847
NGC2410	0.3168	34.00000	71.53049
NGC2916	0.58891	12.82305	53.92030
NGC3160	0.28539	138.94835	73.41784
NGC3182	0.82819	141.5943	34.08675
NGC4644	0.44886	48.38552	63.32943
NGC5216	0.90582	58.81518	25.06605
NGC5378	0.62817	60.16971	51.08476
NGC5957	0.75068	89.36933	41.35068
NGC5971	0.49239	128.34905	60.50221
NGC6394	0.29281	33.92281	72.97374
UGC09110	0.44667	21.20425	63.46977

The kinematic method can also be affected strongly by the last two, but it is more robust against the first three. A visual inspection of the optical SDSS images of the galaxies of our sample (see figure A.1) shows that we have some edge-on galaxies that have the nucleus almost hidden by very opaque dust bands. Also some galaxies have bars and very prominent spiral arms, like NGC6394 and UGC09110 respectively. This can complicate the correct localization of the centres by the photometric method. Thus we took the photometric results by the CALIFA collaboration and also found the centres ourselves with the kinematic maps in order to see which determination was better for each galaxy.

We took the minor to major axis ratio (B/A) and the position and inclination angles provided by the CALIFA collaboration and determined the centres, although a visual inspection of the images was done to detect any anomaly in the provided values (see table 3.2.

Kinematic Maps: Rotation Velocity

Velocity of the (ionized) gas along the line-of-sight v_{los} (also sometimes called radial velocity, but we will not use this term in this context to avoid confusion with the actual radial movement of gas and stars inside galaxies), can be determined for each spaxel by measuring the Doppler shift in emission lines as a velocity shift respect to the rest frame of the galaxy:

$$v_{los} = c\ \frac{\lambda_1 - \lambda_0}{\lambda_0} \tag{3.8}$$

where λ_0 is the wavelength of the line at rest, λ_1 the observed wavelength (given by the mean of the Gaussian that we fitted to the line) and c is the speed of light. An example of a map of v_{los} for the galaxy NGC6394 is shown in figure 3.3 (a). As the spectra are already corrected for redshift, we are dealing here only with the velocities in the reference frame of the galaxy. The median of the velocity of all spaxels of each galaxy is subtracted in order to eliminate any residual systemic velocity.

However, we really need to know the real rotation velocity of the gas around the galaxy, not only the component in our line-of-sight, as this last one depends strongly on the galaxy's inclination angle. Hence, an inclination correction is needed (Wuyts et al. 2016; Genzel et al. 2017). Disk galaxies are usually modeled as an infinitesimally thin disk, but in reality they have a considerable thickness. For highly inclined disk galaxies this thickness can influence the measurement of the minor axis of the projected disk. A scale length for the thickness in disk galaxies, is assumed to be $C/A = 0.25$ (Wuyts et al. 2016), where C is the projected axis perpendicular to the plane of the disk and A is the major axis. Hence the inclination angle i is given by:

$$\cos i = \sqrt{\frac{(B/A)^2 - (C/A)^2}{1 - (C/A)^2}} \tag{3.9}$$

With this, we applied the *inclination correction* to each spaxel:

$$v_\theta = \frac{v_{los}}{\sin i} \tag{3.10}$$

where v_θ is the tangential or rotational velocity. An example of inclination corrected rotational velocity map is shown in figure 3.3 (b).

As we are plotting this maps using the Hα line emission, a great part of what wee see in them comes from star forming regions. This regions are usually turbulent,especially when their star formation rate is high: radiation pressure from massive stars introduces mechanical energy and momentum into the interstellar medium. As this turbulence implies movement of gas at different speeds in random directions, it introduces noise in our measurements. In our case also we can have noise from the movement of clouds in the NLR. Therefore another correction, called *pressure correction* is needed (Burkert et al. 2010). Usually this correction is more important at high redshift where the star formation rate was higher that in the local Universe, but the effect was found to be significant for our sample.

The turbulent motions are accounted for the velocity dispersion of the ionized gas σ_{gas} (see next section).Then the pressure-corrected rotation velocity is:

$$v_{rot}^2 = v_\theta^2 + 2\sigma_{gas}^2 \frac{R}{R_d} \tag{3.11}$$

where R is the radial distance from a given spaxel to the centre of the galaxy, and R_d is the scale length given by

$$R_d = \frac{R_e}{1.68} \tag{3.12}$$

with R_e being the effective radius (Burkert et al. 2010; Genzel et al. 2017). v_{rot} is then the velocity of a thin infinitesimal disk of gas with circular orbits without the turbulent movement of the gas. This result yields the true rotational velocity component in the plane of the disk.

One important consequence of this correction that can be seen clearly comparing figures 3.3 (b) and (c) is that in general the velocity increases for all spaxels. This happens because part of

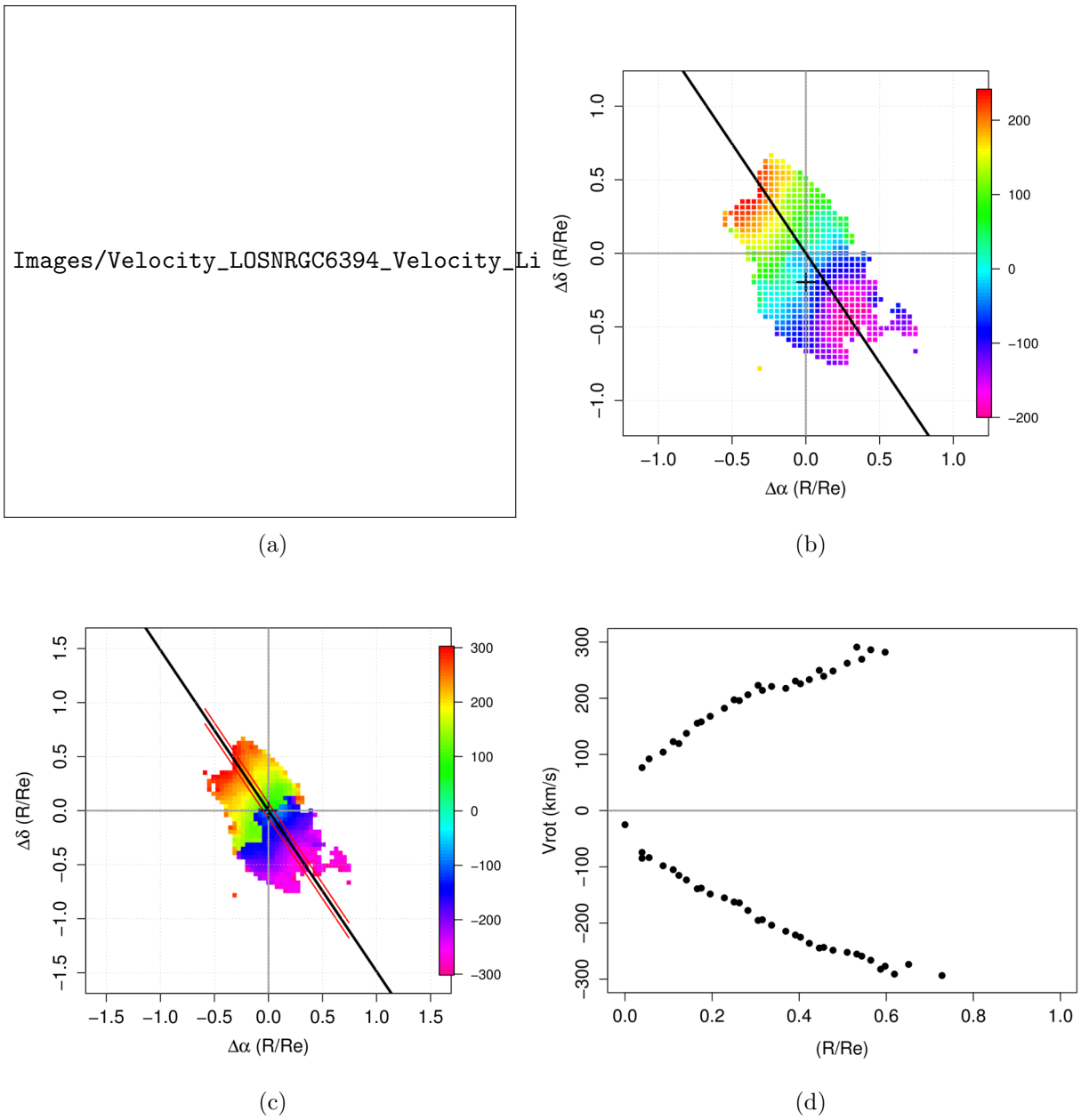

(a) (b)

(c) (d)

Fig. 3.3: An example of the effect of the corrections applied to obtain the rotation velocity map in the case of the galaxy NGC6394. The colour scale shows velocity in km s^{-1}. The horizontal and vertical axes are distances in declination and right ascension respectively, normalized to the effective radius. The black crosses mark the rotation centre determined by the lowest velocity spaxel. The black line marks the direction of the position angle as given by CALIFA. (a) Line of sight velocity map. (b) Rotational velocity map after the inclination correction; the effect is small as the galaxy has a low inclination. (c) Rotational velocity map after the inclination and the pressure corrections. After the corrections are applied, the kinematic centre coincides with the one reported by CALIFA, at coordinates (0,0). The red lines in (c) enclose the spaxels used for plotting the rotation velocity profile. (d) Rotation velocity profile. As we can see in figure A.1, NGC6394 is a spiral galaxy with a very prominent bar. These maps show mostly the bar rotation, with almost parallel isovelocity contours(spaxels of the same colour) and a linear rotation profile, as expected for a classic bar with a solid-body-like rotation.

the gravitational force acting on the gas is balanced with the pressure force (Burkert et al. 2010). Also the border between the positive and negative velocity zones have now become abrupt and well defined, as it should be, contrary to the v_{los} component case where there was zone of very low velocity between them.

This correction has proven to be crucial for our analysis as it changes significantly the kinematic determination of the rotation centres: only after performing both inclination and pressure corrections, the galactic centres coincide with the ones photometrically determined by CALIFA (see figure 3.3) in most galaxies, for example see figure 3.3 (c). However there are some galaxies which have centres that do not coincide with that of CALIFA even after these corrections, so we had to examine them carefully to understand why this is happening. To accomplish that, we can have some extra help from the velocity dispersion maps, explained in the next section.

Kinematic Maps: Velocity Dispersion

Whenever we have a large number of bodies moving randomly, like stars in a galaxy or multiple individual clouds of gas, the width of emission-lines increases due to the Doppler shifts caused by the movement of these bodies moving. This confers the emission lines a Gaussian-like profile with a width characterized by the standard deviation σ. We can obtain this parameter from the Gaussian that we fitted to the line, which we will call σ_{obs}. This parameter gives us a measure of the range of velocities that the particles reach, called velocity dispersion. In order to obtain the intrinsic width σ, σ_{obs} has to be corrected by the *instrumental width* σ_i. This is the width that would have an infinitesimally thin spectral line when observed with the instrument; that is in practice the instrumental spectral resolution. As we are using re-sampled spectra to fit the Gaussian, we have changed artificially this resolution to be 1 Å. The instrumental width correction is then: CORRECTION FOR NOMINAL VALUE

$$\sigma = \sqrt{\sigma_{obs}^2 - \sigma_i^2} \tag{3.13}$$

Finally we need to convert this width in [Å] to velocity units of [km s^{-1}], which gives us the *velocity dispersion* of the ionized gas σ_{gas}, a measure of the range of randomly directed velocities that the clouds of gas have apart from the rotational motion:

$$\sigma_{gas} = \frac{c\ \sigma}{\lambda_o} \tag{3.14}$$

The effect of the instrumental width correction is small, on average $\approx$ 20 km s^{-1} for most galaxies. Examples of the velocity dispersion map and the velocity dispersion profile for NGC6394 are shown in figures 3.4 (a) and (b).

Kinematic Maps: v_{rot}/σ_{gas}

Finally we can combine the information from both the rotation velocity and the velocity dispersion in order to have a broader picture of the galactic kinematics. Obtaining maps of the rate between both quantities v_{rot}/σ_{gas}, we can see in which regions the ionized gas movement is dominated by rotation ($v_{rot}/\sigma_{gas} > 1$) or by pressure and turbulence ($v_{rot}/\sigma_{gas} < 1$). A map of this parameter was elaborated for each galaxy. These maps clearly show the bulges with the lowest values of v_{rot}/σ_{gas}, as expected, which is of great help to locate the real kinematic centre in the cases where there are non-negligible discrepancies between the rotation velocity, velocity

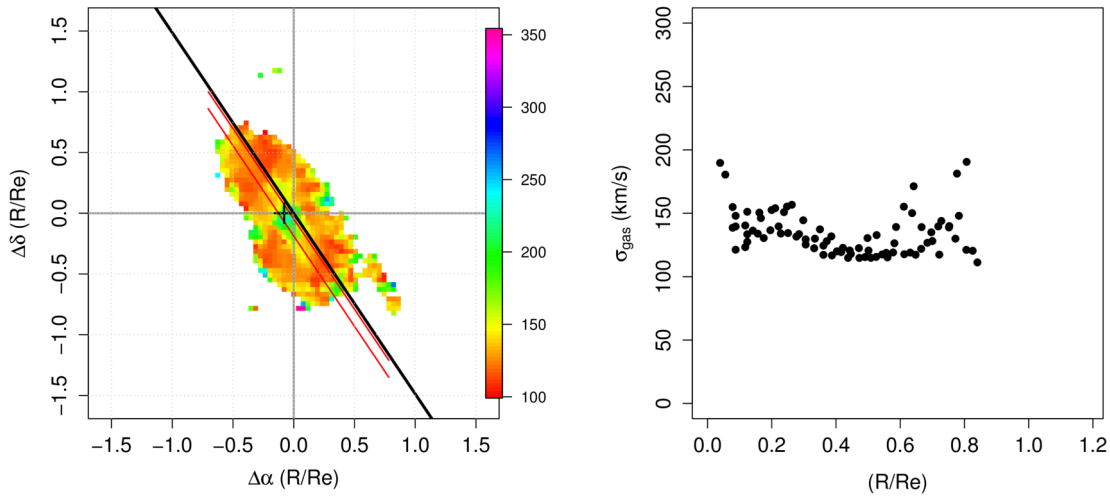

(a) (b)

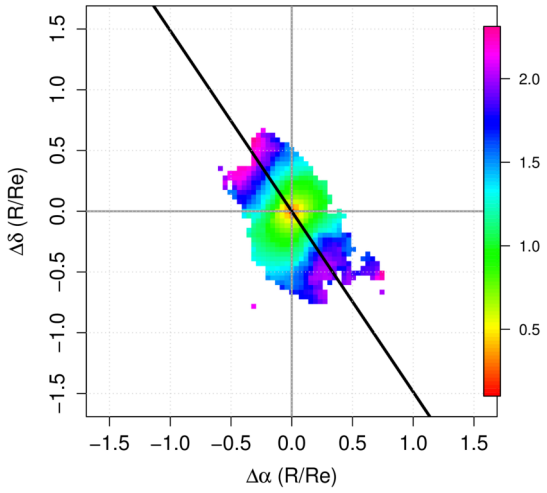

(c)

Fig. 3.4: (a) Velocity dispersion map for NG6394. The units of the colour scale are in km s^{-1}. The CALIFA photometrically determined centre (from SDSS) is at coordinates (0,0). The black cross marks the point of maximum velocity dispersion near the CALIFA centre. The black line marks the direction of the position angle and the red lines contain between them the spaxels used for the velocity dispersion profile. We can see that the bar has a very low velocity dispersion in general, as expected from its solid-body-like rotation curve, except for a region near the centre. (b) Velocity dispersion profile. The velocity dispersion is high at the centre and diminish along the bar which has a very well defined rotation movement, but goes up again in the star forming regions where the bar meets the disk at ≈ 0.8 Re. (c) v_{rot}/σ_{gas} map showing that despite having a prominent bar, there is still a small region where the movement of the gas is pressure dominated, like in a bulge, that coincides with the higher velocity dispersion seen in (a) and is compatible with the position of both photometrically and kinematically determined centres.

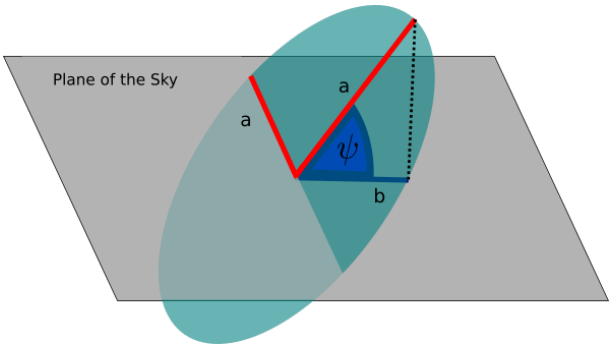

Fig. 3.5: Diagram showing the geometric disposition assumed in order to deproject maps. The observer is supposed to be up, in a direction perpendicular to de plane of the sky. The galaxy is supossed to be a circle of radius a forming an angle ψ with the plane of the sky. The observer sees a projected ellipse of semi-major axis a and semi-minor axis $b = a \cos \psi$.

dispersion and photometry-determined centres. An example of one of these maps can be seen in figure 3.4 (c).

3.6.2 Deprojection

The maps had to be deprojected in order to account for deformations due to the angle of the galaxies disk plane respect to the plane of the sky (inclination). This allows us to measure real distances in the plane of the disk instead of distances projected in the plane of the sky.

Deprojection Procedure

Here we describe the algorithm developed by us to deproject the maps. We start from the hypothesis that the galaxy is a flat circular disc and that we see it as an ellipse as a result of the inclination angle between the disc and the plane of the sky (see figure 3.5). We can deduce, in first approximation, this angle from the B/A ratio, of the minor B to the major A axis of each galaxy (i.e. a measure of how flattened is the ellipse that we see compared to the supposed original circular form). The steps to achieve this where done as follows:

1) We have information for the Position Angle (PA) and the B/A ratio of the semi-minor B to the semi-major axis A of each galaxy, as provided by the CALIFA DR3 dataproducts. PA was converted from degrees to radians. In cases where we decided not to use the CALIFA determined centre, the coordinates of all spaxels were displaced in order to give coordinates $(0, 0)$ to the new centre.

2) Each spaxel has an assigned (projected) x_p and y_p coordinate corresponding to the Right Ascension (RA) and Declination (δ) axis respectively. The coordinates origin is at the bottom-left corner of the array, beginning at $(0, 0)$. They were displaced in order to put the origin at the centre as given by the FITS file's header. Then we calculated the projected galactocentric distance R_p for each spaxel using the Pythagorean theorem.

$$R_p = \sqrt{x_p^2 + y_p^2} \tag{3.15}$$

3) The projected angle θ_p in the plane of the sky for each spaxel was then calculated.

$$\theta_p = \arctan \frac{y_p}{x_p} \tag{3.16}$$

4) The coordinate frame was rotated in order to have $PA = 0$, to make the next transformations easier. The projected x_p and y_p coordinates of each spaxel were rotated and reassigned as:

$$x_1 = R_p \left[\cos(\theta_p - PA)\right] \tag{3.17}$$

$$y_1 = R_p \left[\sin(\theta_p - PA)\right] \tag{3.18}$$

Spaxels with coordinates $x = 0$ and $y = 0$ were reassigned to $x = 0.0000001$ and $y = 0.0000001$ in order to avoid infinite values in future calculations.

5) For each galaxy, the inclination angle ψ was found (see figure 3.5).

$$\psi = \arccos \frac{a}{b} \tag{3.19}$$

6) Deprojection can be done now, and as the position angle was set to $PA = 0$ (step 4) we have to correct only the x_1 coordinate.

$$x_2 = \frac{x_1}{\cos \psi} \tag{3.20}$$

$$y_2 = y_1 \tag{3.21}$$

7) With the new deprojected coordinates, the deprojected galactocentric radius R_d was calculated for each spaxel as well as the deprojected angle θ_d for each spaxel.

$$R_d = \sqrt{x_2^2 + y_2^2} \tag{3.22}$$

$$\theta_d = \arctan \frac{y_2}{x_2} \tag{3.23}$$

For the spaxels in the second and third quadrant ($x_2 < 0$, $y_2 > 0$ and $x_2 < 0, y_2 < 0$, respectively), the arctan function, degenerates, so we have to add π to equation 3.23 in those cases.

8) Finally the resulting map was rotated again to the original position angle. The final deprojected coordinates x_d and y_d are:

$$x_d = R_d \left[\cos(\theta_d + PA)\right] \tag{3.24}$$

$$y_d = R_d \left[\sin(\theta_d + PA)\right] \tag{3.25}$$

With these coordinates we can plot the spaxels at the position they would be if we were seeing the galaxy completely face-on. This procedure was not applied to ellipticals nor edge-on spirals (which constitute half of the sample). Hence the deprojection was applied only to: MCG-02-02-030, NGC2410, NGC2916, NGC4644, NGC5378, NGC5957, NGC5971, NGC6394 and UGC09110.

Normalization by the Effective Radius

All galactocentric distances for the maps and radial profiles have been normalized to the effective radius *Re* of the galaxies, as reported in the CALIFA DR3 dataproducts. This has the advantage of having a measure of distance relative to the intrinsic stellar properties of the galaxy, independent of its size.

3.7 BPT Maps and BPT Limits Redefiniton

The BPT81 diagrams elaborated with the spaxels of each galaxy of our sample show an interesting anomaly: the Ke06 and the Ci10 lines that divide Seyfert AGN from LINER AGN, does not appear to separate clearly the two groups, not even in the case of BPT-OI and BPT-SII (see figure 3.6). Most spaxels appear to follow a sequence along the right wing of the BPT, but this sequence is divided by the Ke06 line. As we know, our sample galaxies have exclusively Seyfert 2 AGN, so in principle there should be no LINER ionized spaxels at all. We now propose that all those LINER-like spaxels along the right wing must be ionized by the Seyfert 2 AGN. This is an indication that the Ke06 line, which was initially proposed for individual galaxies, does not work properly in the case of individual spaxels within the same galaxy. This tendency is observed in all the galaxies of our sample. A first solution would be to label all spaxels beyond the Ke01 line as AGN, but things are not that simple: in many galaxies we find some spaxels with high values of low-ionization line ratios and low $\log_{10}([\text{O III}]/\text{H}\beta)$ values. These spaxels are clearly separated from the right wing, well into the LINER zone, and also in the maps they tend to be spatially at further radial distances than the bulk of Seyfert/LINER-like spaxels (although not in all cases). All this makes evident that these spaxels are anomalous and have an ionization source or a set of physical conditions not related to that of the rest of the spaxels. Therefore, we need to establish a limit to separate them from the right wing AGN-ionized spaxels in order to measure properly the influence radius.

BPT81 diagrams with all the spaxels from the galaxies in the sample are shown in figure 3.6. The Ke06 lines and Ci10 line are represented with black dotted lines in their respective diagrams. A Kernel Density Estimation (KDE, see appendix B) was applied to all the spaxels. The density contours at 0.5, 1, 1.5, 2, 2.5, 3 and 4 standard deviations are plotted. As can be seen, in BPT-NII and BPT-SII diagrams the right wing is clearly delimited and the anomalous LINER-like spaxels are observed far apart. Since there is no clear overdensities of these anomalous spaxels (as can be seen from the contours), we cannot apply directly the method used by Kewley et al. (2006) to establish the limit between the two groups. We developed our own empirical method, that in essence is based on the same idea: to use the density of spaxels in the BPT81 diagrams as a criteria.

We selected some points along the right side of a selected line contour. We took the 2.5σ contour in the case of BPT-NII and the 2σ contour for the BPT-SII, and fitted a second order polynomial function with the coordinates of these points. The fitting parameters are shown in table 3.3. Since the [O I] λ 6300 line is in general very faint, we did not obtain enough spaxels to clearly delimit the right wing, as no clear pattern is seen in the contours, see figure 3.6 (c). Anyway, there is presence of anomalous LINER-like spaxels with very high values of the $\log_{10}([\text{O I}]/\text{H}\alpha)$ line ratio. Our proposed new limits between Seyfert and anomalous spaxels are shown as purple dashed lines in figure 3.7. The proposed new limits are:

For the BPT-NII:

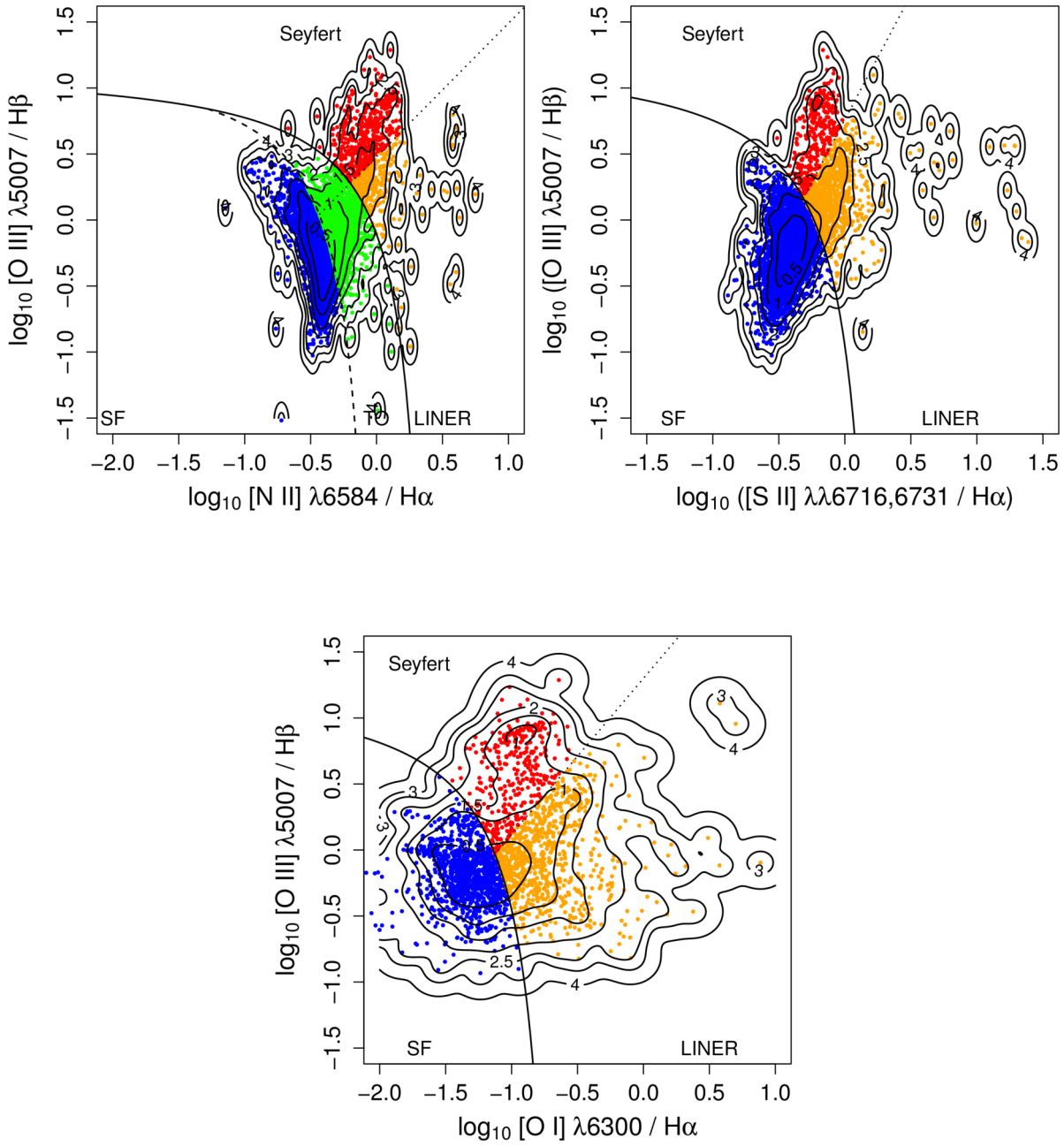

Fig. 3.6: BPT81 diagrams including all spaxels from the 18 galaxies of the sample, with the usual Ke01 (solid curve), Ka03 (dashed curve), Ke06 and Ci10 (dotted lines) limits. The contours mark the resulting densities from the KDE at 0.5, 1, 1.5, 2, 2.5, 3 and 4 sigmas. (a) BPT-NII, (b) BPT-SII, (c) BPT-OI.

Table 3.3: Fitting parameters for the new proposed divisions for the BPT-NII and BPT-SII diagrams.

Diagram	Number of points used	p-value
BPT-NII	7	6.326×10^{-5}
BPT-SII	7	1.299×10^{-5}

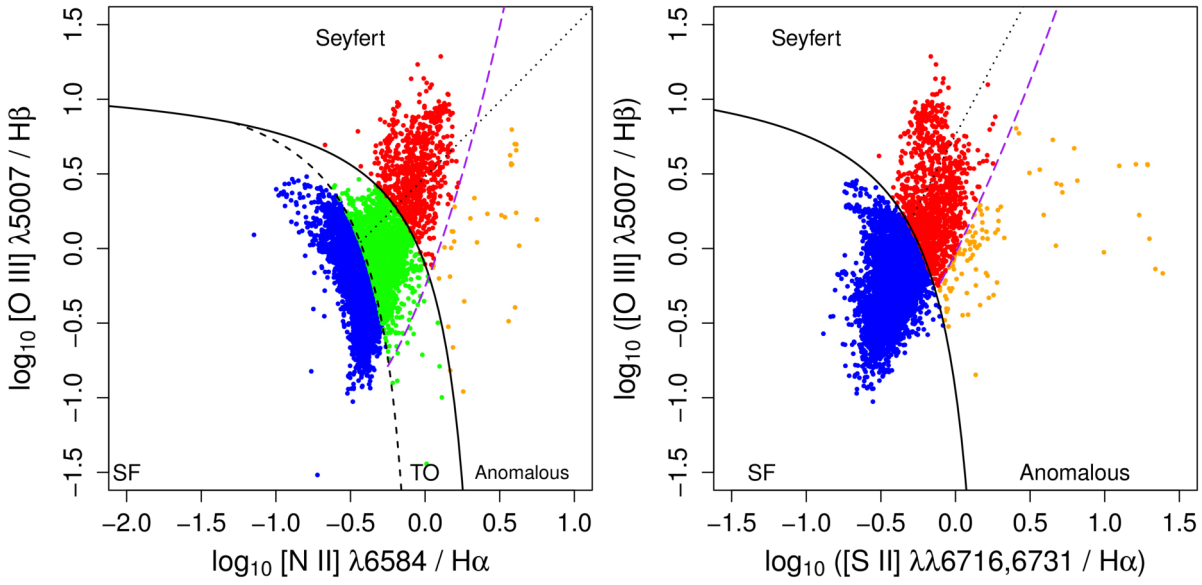

Fig. 3.7: BPT81 diagrams including all spaxels from the 18 galaxies of the sample, with the usual Ke01 (solid black curve), Ka03 (dashed black curve), Ke06 and Ci10 (dotted black lines) limits, but including our new proposed limit for Seyfert and anomalous LINER-like spaxels as a purple dashed line. Also the colours correspond to our proposed division. (a) BPT-NII, (b) BPT-SII.

$$\log_{10}\frac{[\text{O III}]}{\text{H}\beta} = 1.80282\left(\log_{10}\frac{[\text{N II}]}{\text{H}\alpha}\right)^2 + 2.58101\left(\log_{10}\frac{[\text{N II}]}{\text{H}\alpha}\right) - 0.25599 \tag{3.26}$$

For the BPT-SII:

$$\log_{10}\frac{[\text{O III}]}{\text{H}\beta} = 0.56115520\left(\log_{10}\frac{[\text{S II}]}{\text{H}\alpha}\right)^2 + 0.02573341\left(\log_{10}\frac{[\text{S II}]}{\text{H}\alpha}\right) - 0.02954284 \tag{3.27}$$

3.8 Physical parameters of the Black Hole

In order to get a better insight of the underlying physics behind the influence radius of the AGN, we looked for correlations between this parameter and two of the main physical parameters in an AGN: the black hole mass and its accretion rate.

3.8.1 Determination of the Black Hole Mass

For this we used the relation between the central stellar velocity dispersion $\sigma^\star$ and the black hole mass M_{BH}, with the calibration given by McConnell & Ma (2013):

$$\log_{10} M_{BH} = \alpha + \beta \left(\frac{\sigma^\star}{200\,[\text{km s}^{-1}]} \right) \tag{3.28}$$

with the coefficients:

$$\alpha = 8.32 \pm 0.05 \tag{3.29}$$

$$\beta = 5.64 \pm 0.32 \tag{3.30}$$

The central stellar velocity dispersions were taken from the CALIFA DR3 dataproducts. There were no available $\sigma^\star$ for the galaxies NGC0681 and NGC5957 as both galaxies have their bulges almost completely hidden behind the lanes of dust of their disks. Therefore the statistics that need the M_{BH} parameter do not include these two galaxies. The uncertainties are propagated from the reported error for $\sigma^\star$ and the ones in the coefficients α and β as:

$$\sigma^2_{M_{BH}} = \sigma^2_\alpha + \left(\log_{10} \frac{\sigma^\star}{200\,[\text{km s}^{-1}]} \right)^2 \sigma^2_\beta + \left(\frac{\beta}{\sigma^\star \ln 10} \right)^2 \sigma^2_{\sigma^\star} \tag{3.31}$$

3.8.2 Determination of the Accretion Rate

The accretion rate determines the bolometric luminosity L_{bol} emitted by the accretion disk. We can resolve spatially up to the central spaxel in order to avoid stellar light contamination. In the case of type 1 AGN where the accretion disk is exposed to the line-of-sight, we can estimate directly the bolometric luminosity from the flux of the continuum at a wavelength where there is no contamination by emission or absorption lines. Usually that wavelength is 5100 Å, with the assumption that the continuum at this position is dominated by that from the accretion disk.

In type 2 AGN, since the observed continuum is contaminated with the stellar one, we cannot apply that technique to them. Since most galaxies in our sample are Seyfert 2, we used a relation involving the luminosity $L_{[O\ III]}$ of the [O III] λ5007 emission line to estimate the bolometric luminosity. This can be done because $L_{[O\ III]}$ depends directly on the UV continuum.

Determination of $L_{[O\ III]}$

$L_{[O\ III]}$ is estimated from the previously determined surface specific intensity of the line:

$$L_{[O\ III]} = 4\pi\kappa D^2 I_{[O\ III]} F_{\text{H}\beta} \tag{3.32}$$

where D is the distance to the galaxy in [cm], $I_{[O\ III]}$ is the dereddened and normalized specific intensity of the [O III] λ5007 line in units of [erg s^{-1} cm^{-2} sr^{-1} Å^{-1}] (see section 3.5), $F_{\text{H}\beta}$ is the observed surface specific intensity of Hβ in units of [erg s^{-1} cm^{-2} arcsec^{-2} Å^{-1}] and κ is a factor to account for unit conversions:

$$\kappa = \frac{(\lambda)(2.3504 \times 10^{-11})\left[\text{arcsec}^2\ \text{sr}^{-1}\right]}{100} \tag{3.33}$$

with $\lambda = 5007$ Å being the rest wavelength of the emission line.

The distance D to the galaxy is calculated using the Hubble law $D = cz/H_0$, with c being the speed of light, z the redshift from SDSS DR7, and with a value for the Hubble constant $H_0 = 70$ [km s^{-1}Mpc^{-1}]. The uncertainty in the distance is propagated from the uncertainty of the SDSS DR7 redshift as:

$$\sigma_D^2 = \left(\frac{c}{H_0}\right)^2 \sigma_z^2 \tag{3.34}$$

The terms inside the parenthesis on the right-hand side must be multiplied by a factor of 3.085×10^{24} in order to convert from Mpc to cm.

The uncertainty in $L_{[O\ III]}$ is then propagated from the uncertainties in D, $I_{[O\ III]}$ and $F_{\mathrm{H}\beta}$:

$$\sigma^2_{L_{[O\ III]}} = \left(8\pi\kappa I_{[O\ III]} F_{\mathrm{H}\beta} D\right)^2 \sigma_D^2 + \left(4\pi\kappa F_{\mathrm{H}\beta} D^2\right)^2 \sigma^2_{I_{[O\ III]}} + \left(4\pi\kappa I_{[O\ III]} D^2\right)^2 \sigma^2_{F_{\mathrm{H}\beta}} \tag{3.35}$$

Determination of L_{bol} from $L_{[O\ III]}$

This is achieved multiplying $L_{[O\ III]}$ by a correction factor, which was calibrated by Lamastra et al. (2009):

$$L_{bol} = C_{[O\ III]} L_{[O\ III]} \tag{3.36}$$

where $C_{[O\ III]}$ is the correction factor. Lamastra et al. (2009) found that this correction factor is dependent on the values of $L_{[O\ III]}$. When the range of $\log_{10} L_{[O\ III]}$ is $38-40$, $40-42$ and $42-44$, the value of $C_{[O\ III]}$ is 87, 142 and 454 respectively. The propagated uncertainty in L_{bol} is:

$$\sigma^2_{L_{bol}} = C^2_{[O\ III]} \sigma^2_{L_{[O\ III]}} \tag{3.37}$$

The Accretion Rate

Finally the accretion rate $\dot{m}$ is determined using the equation from Peterson (1997):

$$\dot{m} = 1.8 \times 10^{-3} \left(\frac{L_{bol}}{1 \times 10^{44}}\right) \frac{1}{\eta} \tag{3.38}$$

where $\eta = 0.1$ is the assumed efficiency of the accretion disk in converting matter into energy. The uncertainty of $\dot{m}$ is:

$$\sigma^2_{\dot{m}} = \left(\frac{1.8 \times 10^{-3}}{1 \times 10^{44}} \frac{1}{\eta}\right)^2 \sigma^2_{L_{bol}} \tag{3.39}$$

3.9 Shifted Components and Outflows

A search for possible outflows was made for the whole sample by searching for shifted components of the Hα and [O III] λ5007 emission lines. For this we used the package FitSpec developed by Torres-Papaqui and Mullaney (University of Sheffield), written in IDL, which fits different Gaussian components to the emission lines. An example of such displaced components for the central regions of NGC0681 is shown in figure 3.8 (a) for Hα and in figure 3.8 (b) for [O III] λ5007.

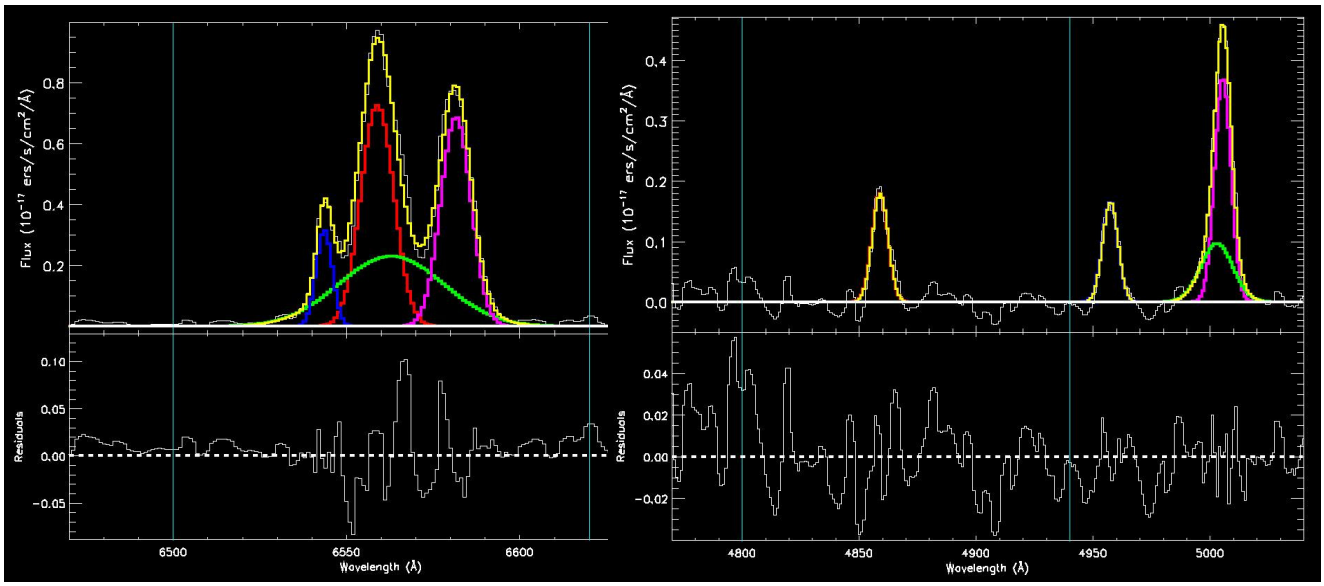

(a) (b)

Fig. 3.8: Gaussian components fit for the central region of NGC0681 (a)Hα (b) O III λ5007. The found shifted and broader component is shown in green colour.

Chapter 4

Results and discussion

The results of the analysis and a discussion of their implications are presented in this chapter.

4.1 Analysis of Kinematic Maps and Determination of the Centres

Kinematic maps were produced for all the galaxies in the sample (see section 3.6.1). Also, radial profiles of rotation velocity v_{rot} and velocity dispersion σ_{gas} were made. The aim was to determine the kinematic centres to compare them with the photometrically determined centres by the CALIFA collaboration, in order to correctly estimate the position of the SMBH, assuming that it should be located at the galactic centre. None of the kinematic maps are deprojected because the localization of the centre is a previous requirement for deprojection, therefore the scale is the same as in the optical images of figure A.1 in appendix A, allowing for direct comparison. Figure A.2 shows rotation velocity maps corrected for inclination and pressure as explained in section 3.6.1. Figure A.3 shows the rotation velocity profiles using spaxels contained between the red lines of the maps in figure A.2, tracing the rotation curves along the major axis. Dispersion velocity maps are shown in figure A.4, as well as the correspondent velocity dispersion profiles in figure A.5. The v_{rot}/σ_{gas} maps are shown in figure A.6.

We can compare these maps to decide which centre determination to use for each galaxy. Despite some of the galaxies having high inclination and presenting prominent dust bands in the plane of the disk, generally rotation-velocity determined centres do coincide well within less than 1 arcsec with the ones determined by CALIFA. The velocity dispersion maps mostly show centres not compatible with those of CALIFA. This discrepancy can be explained by looking at the v_{rot}/σ_{gas} maps. The position of the bulge is clearly identified in these maps, and in most cases they are compatible with both the rotation velocity and photometric centres.

Table 4.1 shows the coordinates of the centres determined with both methods relative to the CALIFA centres (which have coordinates $0, 0$). As can be seen, velocity rotation centres in general are in very good agreement with the ones photometrically determined by CALIFA. The reported uncertainties correspond to the spatial sampling of the CALIFA datacubes of 1 arcsec. Other observational contributions to the uncertainties, such as the seeing, are very complicated to propagate since the datacubes suffered a dithering process (see section 1.2.1) so we do not include them here.

Some galaxies that showed significant discrepancies between the three methods and required special attention were:

Table 4.1: Offsets of the centres determined with line-of-sight velocity maps (columns 2 and 3) and with velocity dispersion maps (columns 4 and 5) relative to the CALIFA centre (which has coordinates $0, 0$) in arcseconds.

Galaxy	$\Delta\alpha$ (v_{rot})	$\Delta\delta$ (v_{rot})	$\Delta\alpha$ (σ_{gas})	$\Delta\delta(\sigma_{gas})$
IC0485	(0.0 ± 1.0)"	(0.0 ± 1.0)"	(-3.0 ± 1.0)"	(-2.0 ± 1.0)"
IC0540	(0.0 ± 1.0)"	(0.0 ± 1.0)"	(-2.0 ± 1.0)"	(0.0 ± 1.0)"
IC2247	(0.0 ± 1.0)"	(0.0 ± 1.0)"	(-1.0 ± 1.0)"	(-2.0 ± 1.0)"
IC4215	(0.0 ± 1.0)"	(0.0 ± 1.0)"	(4.0 ± 1.0)"	(0.0 ± 1.0)"
MCG-02-02-030	(0.0 ± 1.0)"	(0.0 ± 1.0)"	(3.0 ± 1.0)"	(2.0 ± 1.0)"
MCG-02-08-014	(2.0 ± 1.0)"	(2.0 ± 1.0)"	(0.0 ± 1.0)"	(3.0 ± 1.0)"
NGC0681	(0.0 ± 1.0)"	(0.0 ± 1.0)"	(-3.0 ± 1.0)"	(-2.0 ± 1.0)"
NGC2410	(0.0 ± 1.0)"	(0.0 ± 1.0)"	(-3.0 ± 1.0)"	(-2.0 ± 1.0)"
NGC2916	(-1.0 ± 1.0)"	(0.0 ± 1.0)"	(-2.0 ± 1.0)"	(3.0 ± 1.0)"
NGC3160	(0.0 ± 1.0)"	(0.0 ± 1.0)"	(0.0 ± 1.0)"	(1.0 ± 1.0)"
NGC3182	(-3.0 ± 1.0)"	(-3.0 ± 1.0)"	(0.0 ± 1.0)"	(3.0 ± 1.0)"
NGC4644	(0.0 ± 1.0)"	(-1.0 ± 1.0)"	(2.0 ± 1.0)"	(-1.0 ± 1.0)"
NGC5216	(3.0 ± 1.0)"	(0.0 ± 1.0)"	(2.0 ± 1.0)"	(3.0 ± 1.0)"
NGC5378	(-1.0 ± 1.0)"	(0.0 ± 1.0)"	(2.0 ± 1.0)"	(0.0 ± 1.0)"
NGC5957	(0.0 ± 1.0)"	(0.0 ± 1.0)"	(-1.0 ± 1.0)"	(3.0 ± 1.0)"
NGC5971	(-4.0 ± 1.0)"	(2.0 ± 1.0)"	(-2.0 ± 1.0)"	(-3.0 ± 1.0)"
NGC6394	(0.0 ± 1.0)"	(0.0 ± 1.0)"	(-2.0 ± 1.0)"	(0.0 ± 1.0)"
UGC09110	(0.0 ± 1.0)"	(0.0 ± 1.0)"	(-2.0 ± 1.0)"	(3.0 ± 1.0)"

1. MCG-02-08-014: Both rotation velocity and velocity dispersion centres disagree between them and with the CALIFA one. As we can see in figure A.1 (f) this is an edge-on spiral with the north part of the bulge heavily obscured by dust lines. The photometric determination would then be biased to the south. Both rotation velocity and velocity dispersion put the centre to the north of the CALIFA one, but disagree in the horizontal coordinate, that is parallel to the disk. Since the velocity dispersion centre should be determined by the bulge, which is partly obscured by the dust lanes and contaminated with the plane of the disk because we see it edge-on, the rotation velocity appears to be the less biased of the three, therefore we take it as the real centre.

2. NGC2410: The velocity dispersion map shows a very clear maximum displaced from the position given by CALIFA and rotation velocity. The v_{rot}/σ_{gas} map shows a pressure dominated region of a very irregular form and an inspection of the optical image in figure A.1 (h) shows that it has a bar. The presence of the bar can affect greatly both photometric and kinematic determinations, as we discussed in section 3.6. Then, in this case we took the velocity-dispersion determined centre as the true one due to its clear maximum.

3. NGC5216: This is an interacting elliptical galaxy, part of the Arp104 pair, also known as *The Keenan System*. It shows a large tidal tail that connects NGC5216 to its companion NGC5218 (see figure 4.1). The rotation velocity and the velocity dispersion maps of NGC5216 show an irregular distribution that indicates that the galaxy is affected by the interaction and no rotation or pressure centre can be clearly determined: when we attempted to do that, no determination was compatible with each other nor with the

CALIFA one. It is remarkable that, although it is an elliptical galaxy, a noticeable rotation movement is evident in the rotation velocity map. It is very difficult then to stablish a centre to measure the influence radius, as the SMBH could be located almost anywhere, displaced from the geometrical centre by the interaction. The v_{rot}/σ_{gas} map shows an extended and non-symmetric pressure dominated zone not perfectly centred and compatible with the three centres we have. We decided to use the CALIFA centre, as it is the most centrally located respect to the projected area of the galaxy, although caution is needed when extracting conclusions about the influence radius in this galaxy.

4. NGC5957: This is an almost face-on spiral. As can be seen in the rotation velocity map, the black line that should trace the direction of the position angle along the major axis does not appear to be perpendicular to the isovelocities (spaxels of the same colour), following the direction with the greater gradient. As mentioned in section 3.6, the position angle is difficult to determine for face-on galaxies, as the differences between the major and minor axes are small. This affects the photometric determination even more. The photometrically determined position angle is probably wrong, but, being, face-on, to characterize it kinematically is complicated as well. This is evident in the clumpy appearance of the map in the central regions, which in turn are also not clearly dominated by rotation nor pressure ($v_{rot}/\sigma_{gas} \approx 1$ to an extent beyond 0.5 R_e). Given the galaxy is face-on, the deprojection does not really affect the distance measurements that much, so wee kept on with the CALIFA determined position angle.

5. NGC5971: The rotation velocity map shows a centre displaced from the CALIFA photometric one. The SDSS image in figure A.1 (p) shows that it is a spiral, and the *bumpy* rotation profile seen in figure A.3 (p) indicates that the measurement of the rotation velocity is probably affected by the spiral structure. The velocity dispersion centre is close to the CALIFA centre. Finally we decided to use the CALIFA centre due to this coincidence.

Given the centres determined by rotation velocity and by CALIFA agree for all the other galaxies, we take the CALIFA coordinates for them.

4.2 BPT Diagrams and Maps

4.2.1 Comments on the BPT Diagrams and Their Limits

As we saw in section 3.7, the original limits for the BPT diagrams were designed to classify spectra of individual galaxies, and not spectra coming from spatially resolved regions of the same galaxy[1]. In that section, we proposed a new limit to classify spaxels of Seyfert galaxies according to their BPT81 emission-line ratios. We separated regions ionized by the Seyfert AGN from those ionized by other sources which we called Anomalous, and for which the determination of their nature is beyond the scope of this work.

In this section we present some statistics in order to evaluate the consequences of applying our new limits to the spaxels of our whole sample, compared to the classic limits. Here we use 7019 spaxels from all the galaxies that fulfill the requirement of SNR > 3 in all the emission lines involved in the compared line ratios. Table 4.2 shows the number of spaxels that change their BPT-type when we pass from the BPT-NII to the BPT-SII, both with the Ke06/Ci10

[1]Althouh in literature, usually BPT81 diagrams are constructed with spectra coming from the central regions, e.g. the SDSS spectra are taken with a fibre of 3" in radius around the nucleus.

Fig. 4.1: The Arp104 pair of interacting galaxies. North is up and east is left. NGC5216 is the southern elliptical galaxy. A large tidal tail connects it with NGC5218, the big spiral at the north that also shows signs of tidal disruptions. Both galaxies are included in the CALIFA survey. In principle a detailed kinematic and dynamic analysis of the IFS data the pair could give us some insight on merging and interaction of galaxies, but that goes beyond the scope of this work. Credit: Adam Block, Mt. Lemmon SkyCenter, U. Arizona.

limits and our own. We would expect that very few spaxels would cross the Ke01 line, and this is the case: Most TO spaxels in the BPT-NII are now SF in the BPT-SII, in agreement with them being below the Ke01 line. The clearer effect of our proposed limit is that while some of the TO spaxels that crossed the Ke01 line became LINER type in the classic Ke06 limit, most of them became Seyfert with our new limit, as the limit was displaced toward lower ionization values. It makes sense to the purpose of the new limit since we do know that we have no LINER AGN in our sample. Also many of the spaxels that changed from SF to LINER in the classic limits, changed now from SF to Seyfert. In summary, our new proposed limit effectively classifies correctly the spaxels ionized by the AGN as Seyfert and only leaves the anomalous LINER-like spaxels with high values of low-ionization line ratios classified as the anomalous cases they are.

Tables 4.3 and 4.4 show the spaxels that change the BPT type when applying our proposed limit within the same diagram for BPT-NII and BPT-SII respectively. As expected, the SF and TO spaxels remain the same, and a considerable part of the LINER spaxels become Seyfert type.

4.2.2 Results on BPT-NII Diagrams and Maps

The results are shown in appendix A, figures A.7 through A.10: Figure A.7 shows the BPT-NII diagrams for all galaxies in the sample, figure A.8 shows the corresponding BPT-NII maps used to measure the influence radii and figures A.9 and A.10 show the radial profiles of the $\log_{10}$([O III] λ5007/Hβ) and $\log_{10}$([N II] λ6583/Hα) line ratios, respectively. The colours, both in the maps and the profiles, correspond to the colour of each spaxel according to the classification by the

Table 4.2: Number of spaxels that change the BPT type when we change from BPT-NII to BPT-SII, both for the original BPT limits (second column) and the one with our proposed modification for the Seyfert/Anomalous limit (third column). The first column indicates the change of BPT type. The BPT types are Seyfert (Sy), Star Forming (SF), Transition Object (TO) and LINER/Anomalous.

Change in BPT Type	Original	Modified
SF to Sy	37	240
SF to LINER/Anomalous	284	81
TO to SF	1508	1508
TO to Sy	57	251
TO to LINER/Anomalous	253	59
Sy to SF	0	156
Sy to LINER/Anomalous	71	23
LINER/Anomalous to SF	607	451
LINER/Anomalous to Sy	62	248
Total	2879	3017

Table 4.3: Number of spaxels of each the BPT-NII type when we change the original Seyfert/Liner limit (Ci10) for the one we propose. The first column is the type of spaxel, the second column the number of spaxels of that type in the original BPT-NII, and the third the number of spaxes of that type of spaxel in the modified BPT-NII. The BPT types are Seyfert (Sy), Star Forming (SF), Transition Object (TO) and LINER/Anomalous.

Type of region	Original BPT-NII	Modified BPT-NII
SF	3852	3852
TO	1818	1818
Sy	264	608
LINER/Anomalous	1085	741

Table 4.4: Number of spaxels of each BPT-SII type when we change the original Seyfert/Liner limit (Ke06) for the one we propose. The first column is the type of spaxel, the second column the number of spaxels of that type in the original BPT-NII, and the third the number of spaxels of that type in the modified BPT-NII.

Type of region	Original BPT-SII	Modified BPT-SII
SF	5646	5646
Sy	349	1168
LINER/Anomalous	1024	205

BPT-NII diagrams. Since deprojection was applied to some of these maps in order to present the real distances on the plane of the disk of the galaxies instead of the ones projected on the plane of the sky (see section 3.6.2), in general they cannot be compared directly with the SDSS images in figure A.1 nor with the kinematic maps.

The first thing that we can notice in the BPT-NII maps of figure A.8, especially for the edge-on deprojected galaxies is that there is an almost concentric distribution of the BPT type of the spaxels: at the centres we have a high concentration of red spaxels corresponding to Seyfert type ionization of the gas; around them, we have most of the green spaxels, corresponding to transition objects (TOs), which could be due to a mixture of AGN ionization and star-formation ionization. Finally, in the outer parts dominate the blue spaxels, which correspond to star forming (SF) regions, with some green spaxels between them. The most representative galaxies of this concentric distribution are MCG-02-02-030, NGC2410, NGC3182 and NGC6394.

A particular case that stands out by itself is a small elliptical galaxy, NGC3182 which has a ring of star formation at only ≈ 400 pc from the Seyfert 2 nucleus. This ring can even be seen in the optical SDSS image on figure A.1(k) as a bluish ring. We made a search in the literature and found no in-detail studies for this object and the nature of its star-formation ring. Future detailed studies could reveal interesting information on the AGN-starburst connection. Also, it is remarkable a concentration of Seyfert and Anomalous type spaxels directly to the east and aour of the SF dominated ring.

Another special case is that of UGC09110, which shows the Seyfert spaxels far from the nucleus (see figure A.8(r)), and the nuclear region covered in SF spaxels, despite the kinematic maps showing the bulge clearly at the CALIFA-determined centre. A closer look at the kinematic map in figure A.6(r) shows a region with values of $v_{rot}/\sigma_{gas} \sim 1$ which coincides with the position of the Seyfert spaxels. This is very hard to explain. One possibility is that the SMBH is located outside the galactic bulge causing the Seyfert emission and the relatively high velocity dispersion in that zone. Another possibility is that the star formation rate in this galaxy is very high and the AGN very weak so the first one dominates except for the small region where the Seyfert spaxels are located. This could be the case given the extension of the SF regions and the outstandingly bluish colour in which the galaxy appears on the SDSS image in figure A.1(r), even for regions close to the bulge. An in depth future study of the stellar kinematics and the star formation rate distribution could help to solve this matter, but it is beyond the scope of this work. Here we take the position of the CALIFA centre as that of the SMBH and the influence radius as the distance from there to the farthest Seyfert spaxels, as with the other galaxies in the sample. We assume that the displaced location of the Seyfert spaxels is due to the high absorption and dominance of SF emission lines in the other regions, being that location a special place with lower star formation rate that the rest of the galaxy, allowing for the AGN ionization to prevail, revealing a portion of the ionization cone far from the ionizing source.

Other face-on galaxies also show the concentric distribution, but they have a poorer coverage of the central regions, so the distribution of the AGN influenced zone is less clear. These galaxies are: NGC2916, NGC4644, NGC5957 and NGC5971.

For two of the edge-on galaxies, IC2247 and NGC0681, shown in figures A.8 (c) and (g), there are also interesting features revealed by the BPT-NII maps: we see the same concentric Seyfert-TO-SF distribution of the edge-on galaxies, but the Seyfert and the surrounding TO spaxels appear to be tracing the shape of the ionization cones of the NLR. The suspected cones have their vertices located approximately at the hosts galactic centres, as expected had they originated in the AGN. We see evidence of the presence of two of these cones, both on each side of the galactic planes in IC2247, while in NGC0681 there is evidence only for the cone in the south part of the map, although there are some Seyfert and TO spaxels also in the north

part. If we assume that the green TO spaxels include ionization from the AGN, we can see how the cones become broader but still conserving the cone shape. This is relevant, since those TO spaxels are located mostly in the plane of the disk, this could be evidence of their composite nature: AGN ionization in the background going through the star formation of the disk.

4.2.3 On the Geometry of the AGN Radiation Fields: Hints From the BPT-NII Maps

The concentric distribution is what we would expect from a scenario with a central ionization source: the gas is being ionized by the AGN in the central regions, and star formation progressively dominating outwards as the flux of the AGN radiation diminishes with distance, passing through TO dominated zones to finally SF dominated zones. The ionization cones in IC2247 and NGC0681 are what we would expect in a galaxy hosting an AGN as described by the Unified Model (UM). We would not expect that conditions can exist inside the cones that allow the presence of star forming regions close to the galactic centre, and we would expect to see a clear cone shape in every case, which we do not. In order to explain this discrepancies, we consider three scenarios:

- **Scenario A** The AGN radiation field is isotropically radiated from a central source, decaying with the distance squared, eventually becoming weak enough so that the conditions for star formation are more favourable the farther we go from the centre, transitioning gradually from a Seyfert-dominated ionization region to a mixed TO region, and finally to regions dominated by massive young stars radiation in the SF regions. See figure 4.2(a).

- **Scenario B1** The AGN radiation field propagates only inside ionization cones which are mostly perpendicular to the disk, and the regions with star formation are geometrically outside of the ionization cones, even if they are relatively close to the AGN. See figure 4.2(b).

- **Scenario B2** The AGN radiation field propagates only inside the ionization cones, but at least one of them intersects the disk, so in a limited region of the disk, we have the concentric ionization similar to that of scenario A. See figure 4.2(c).

The concentric distribution of the BPT types of spaxels appears to support scenarios A and B1. Nevertheless, we have to remember that in disk galaxies most of the dense gas is contained in a disk with a width between a few tens to hundreds of parsecs, so the emission lines hat we can measure come mainly from there, even if the source radiation escapes also perpendicular to it. If we had the ionization cones present, and they were oriented in a way that allows most AGN radiation to escape perpendicularly to the galactic plane (scenario B1), we could have star forming conditions relatively close to the nucleus, as it appears to be the case with UGC09110, because most of the disk would be out of the AGN radiation path. In cases for which the star formation occurs at greater galactocentric distances, that should be because the cones are oriented along the galactic plane (scenario B2), but in that case we would see clearly the conical shape of the Seyfert spaxels region, which we do not[2].

Here it seems important to question the nature of the TO-classified regions. For scenario A, with an isotropically radiating central source, implications are that TO regions are inside

[2]All this is assuming that SF should be inhibited inside the ionization cones, or at least in the inner parts of them.

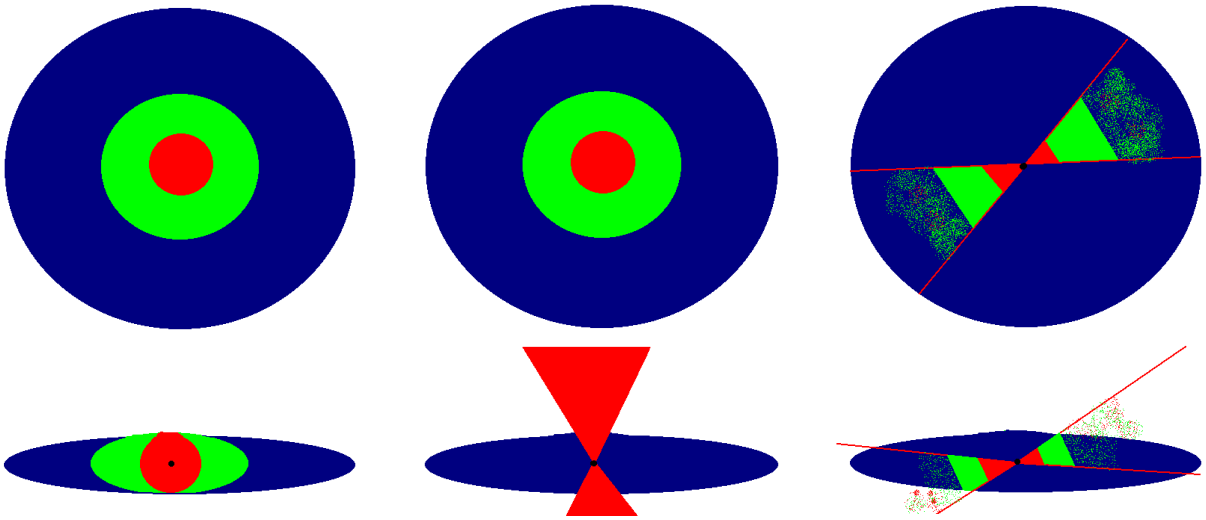

(a) (b) (c)

Fig. 4.2: Schematic representation of the proposed scenarios. Colours correspond to the BPT-NII types: blue for SF, green for TO and red for Seyfert. Below we have a cross-section of the galactic disk and above we have the view that would have an external observer who is viewing the galaxy perpendicularly to the disk plane (face-on). The black dot represent the position of the central ionization source: the SMBH and the accretion disk. (a) Scenario A, an isotropic central source. (b) Scenario B1, ionization cones with their axes perpendicular to the galactic disk, the observer sees SF regions close to the disk and "below" the ionization cones as TO. (c) Scenario B2, at least part of the ionization cones pass through the galactic plane, the TO regions are true composite regions with gas ionized both by the AGN and SF.

the galactic disk and that the gas there are exposed directly to the AGN radiation field. There, conditions would be favourable to star formation inside some molecular clouds shielded from the AGN radiation field, which still ionizes the diffuse gas and the outer parts of the clouds. Progressively, as we go radially out, the AGN radiation becomes weaker and star formation gradually begins to dominate. In this case, it would be difficult to explain the presence of TO spaxels beyond the SF dominated regions, as in the cases of MCG-02-02-030, NGC2916 and NGC5957, or even for UGC09110. This first scenario would also imply a low covering factor of the dust and molecular clouds that would allow some AGN radiation to reach farther away and dominate into regions where the star formation is no longer very high. An observation against scenario A is that for the radiation to be isotropic, we should see the AGN as type 1, at least for face-on galaxies, but all galaxies in our sample are type 2.

In scenario B1, the explanation for the TO regions would be that the ionization cones are perpendicular to the disk, and pointing roughly along our line-of-sight, see figure 4.2 (b). In that case we would see both the underlying star formation in the galactic disk plus the superposed emission from the AGN-ionized gas inside the cones above, which becomes weaker the farther away we are from the central source, given the gas density decreases and the radiation field strength diminishes with distance squared inside the cones. In this case, we would also see the concentric distribution for face on galaxies and the ionization cones for edge-on galaxies, but the implication is that we would have always the cones perpendicular to the disk, implying that the orientations of the planes of the accretion disk, and especially of the dusty torus, are always

aligned to that of the galactic disk, despite the enormous difference in size and mass of these structures, and that the concentric distribution in face-on galaxies would be almost circular.

The two cases of edge-on galaxies with enough spaxel coverage to see the shape of the ionization cones appear to support this second scenario. Also this would imply that the cones are roughly aligned with our line-of-sight also in the case of the elliptical galaxy NGC3182, which has no disk. Therefore, in scenario B1, TO objects would not be really regions containing SF regions and AGN ionized gas in the same volume, but a superposition in the line-of-sight of SF regions in the disk, and AGN-ionized gas inside the ionization cones above. This means that SF can occur closer to the nucleus than in scenario A, as the intense AGN radiation would not affect that much the galactic disk. Again, this means that we should see face-on galaxies with the concentric distribution as type 1 AGN, and all galaxies in our sample are type 2.

We must not forget about the mentioned TO spaxels far from the centre behind the large SF regions. The B1 scenario would also have problems explaining these as the AGN-ionized gas emission comes from greater distances inside the ionization cones (remember that we would be seeing them in projection on the galactic plane) where the density of the gas is even lower and the AGN radiation field even weaker than for the TOs closer to the centre. Scenario A in this case has the advantage of having a greater gas density and shorter distances from the centre as the line-emitting regions would only be inside the disk.

Radial profiles in figures A.9 and A.10 show that we have both TO spaxels and SF spaxels at the same distances from the galactic centres. This can happen only in scenario B2, see figure 4.2 (c). Anyway, the concentric distribution is a lot less clear in the radial profiles than when we just see at the maps. From the profiles alone, we can only assure that the Seyfert spaxels dominate completely the central regions, and at larger distances from the nucleus, we have a mixture of both TOs and SFs.

Remarkably when we see the maps (figure A.8), MGC-02-02-030 and NGC2410 and NGC6394 present concentric but elongated Seyfert central regions, not circular, apparently aligned with also somewhat elongated but less clearly defined TO regions. This could be an indication that there is a preferred orientation of the AGN radiation and hence of the presence of ionization cones along the galactic plane, like in the B2 scenario. Nevertheless, the classic UM predicts that this elongated regions should be smaller towards the central source, like the cones in IC2247 and NGC0681, but they are too wide for this (of the order of kpc in their shortest cross-section for NGC2410 and NGC6394). This could be evidence that the dusty torus does not exist and that the elongated shape is due to other structures at kpc distances from the centre (Coziol 2017, private communication). Also we must mention that this observations are compatible with which was reported by Storchi-Bergmann et al. (2009) on IFS observations of Seyfert galaxies (see also the observational studies by Riffel et al. 2009; Storchi-Bergmann et al. 2010 and the theoretical models by Elitzur & Shlosman 2006), which attributed this to a clumpy torus which allows some radiation to pass through the equatorial plane, but not all (hence, the smaller radius reached in that direction). From this results, and given all the evidence in favour of the existence of a torus (Antonucci 1993) we are eager to discard scenario A and to support scenario B1 in some cases (NGC2247, NGC0681) and scenario B2 (including a clumpy torus) in others (MCG-02-02-030, NGC2410, NGC6394). For the other galaxies, as we have an incomplete spaxel coverage of the central regions, it is very difficult to state any conclusion.

It is also worth to remember that we cannot really see the true three-dimensional geometry of the ionization cones, just their projections on the plane of the sky in the case of edge-on spirals and ellipticals, and on the plane of the disk in the case of deprojected face-on and inclined galaxies. Neither can we assure that such ionization cones exist at all for every case (we have only two clear enough cases: IC2247 and NGC0681). Also we have not enough spatial resolution

to directly study structures of the size of the torus, in order to confirm if it really exists or how is it structured; we are supposing that at least to first approximation, the UM is right. We cannot give a definitive answer on this matter, but just remark that the geometry of the AGN ionizing radiation field is as important as its power in shaping the ionized gas and star formation in the AGN-host galaxies. Implications are deep for the AGN-starburst connection problem, as isotropic central source ionization would imply greater zones of the disk with limited or completely neglected star formation than in the case of ionization cones perpendicular to the galactic plane and out of it. An in depth multiwavelength study of the spatial distribution of the molecular clouds and the diffuse ionized gas in combination with the IFS data presented here, could throw some light to solve this complex problem.

4.2.4 Comparing BPT-NII and BPT-SII Diagrams and Maps

Although they were not used to determinate the influence radii, we constructed and plotted BPT-SII diagrams, maps and line-ratio profiles. The BPT-SII diagrams are shown in figure A.11, the corresponding BPT-SII maps are shown in appendix A, figure A.12. Figures A.13 and A.14 show the radial profiles for $\log_{10}([\text{O III}]\ \lambda 5007/\text{H}\beta)$ and $\log_{10}([\text{S II}]\ \lambda\lambda 6716, 6731/\text{H}\alpha)$ line ratios, respectively, using the colours that each spaxel has in the corresponding BPT-SII diagrams.

Tables 4.5 and 4.6 present the number of spaxels of each BPT type for each galaxy in the BPT-NII and BPT-SII diagrams respectively. It is clear that we have less spaxels available in the BPT-SII maps; in most of them there is no clear coverage of the AGN dominated region, as it is in the BPT-NII maps. Therefore, we did not measure the influence radius using the BPT-SII maps, although they can be useful for comparison with the BPT-NII maps. Given that deprojection was applied to some of these maps in order to present the real distances in the plane of the disk of the galaxies instead of the ones projected in the plane of the sky (see section 3.6.2), in general they cannot be compared directly with SDSS images in figure A.1 nor with the kinematic maps.

The comparison of BPT-NII diagrams and maps with their BPT-SII counterparts shows many similarities, even though despite the fact the fact that BPT-SII maps contain less spaxels. We can notice that in general for face-on and inclined deprojected galaxies, most TO spaxels have become now SF spaxels, as we would expect since they are below the Ke01 line in the BPT-NII diagrams (see section 4.2.1), but in the case of the two edge on spirals showing defined ionization cones (IC2247 and NGC0681), most TO spaxels became Seyfert-type spaxels, making the shape of the ionization cones even more evident in figures A.12 (c) and (g) and therefore, tracing more clearly the AGN-influenced region than in their BPT-NII counterparts.

This observational result throws some light on the nature of the TO spaxels discussed in the previous section: we are seeing ionization cones perpendicular to the galactic disk, and out of it, where there is no star formation, conforming to the proposed B1 scenario of the previous section: the AGN continuum inside the classical ionization cones of the UM ionizes the gas inside the cones to create the Narrow Line Region (NLR).

We have now to ask the question: Why the BPT-NII diagrams show some spaxels inside the ionization cones as TO instead of as Seyfert? Here we have to account for the background star formation of the disk projected into our line-of-sight, given the galaxies are not perfectly edge-on and their disks are not infinitesimally thin. In both galaxies we detect some Seyfert spaxels out of the galactic plane farther away than most TO spaxels, which tend to concentrate in the galactic plane. This can be interpreted as follows: First the AGN radiation closer to the centre is very strong and dominates over the projected background star formation of the disk, hence

Table 4.5: Number of spaxels per galaxy corresponding to each BPT type of object in the BPT-NII diagram: Seyfert (Sy), Star Forming (SF), Transition Object (TO) and Anomalous (An). In the last column is the total number of spaxels per galaxy and in the last row the totals for the whole sample.

Galaxy	Sy	SF	TO	An	Total
IC0485	49	0	44	0	93
IC0540	52	9	40	3	104
IC2247	79	199	105	0	383
IC4215	48	0	28	24	100
MCG-02-02-030	57	382	228	12	679
MCG-02-08-014	29	0	103	5	137
NGC0681	66	871	370	4	1311
NGC2410	81	235	387	1	704
NGC2916	13	1185	291	8	1497
NGC3160	20	0	1	18	39
NGC3182	17	80	120	12	229
NGC4644	5	173	84	0	262
NGC5216	103	0	32	2	137
NGC5378	31	19	31	18	99
NGC5957	11	954	302	2	1269
NGC5971	17	160	14	8	199
NGC6394	46	117	97	0	260
UGC09110	9	1108	224	0	1341
Sample	733	5492	2501	117	8843

we detect those spaxels as Seyfert. Second, the AGN radiation field gets weaker with distance while the (projected) background star formation becomes more important at greater distances from the centre. Here we have a superposition in our line-of-sight of line emission from both the ionization cones and the background disk SF regions. Finally, with no galactic-disk emission in the line-of-sight, we have only the emission by the ionized gas inside the ionization cones with no star formation in the background so we have Seyfert spaxels again, even if the AGN ionizing continuum is weaker there.

This interpretation now seems to explain the concentric distribution and the presence of both TO and SF spaxels beyond the central, Seyfert-dominated zone for NGC0681 BPT-NII maps. For IC2247 we have TO emission through the centre (which again appears as Seyfert in the BPT-SII map), as if the AGN radiation travels through the SF regions in the line of sight and we see again a composite of both, but this time in the plane of the disk.

This has implications for our interpretation of the influence radius R_i, for if the B1 scenario applies in every case and the BPT81 classification of spaxels in face-on and deprojected maps is only caused by a projection of different types of regions in the line-of-sight (Seyfert from within the ionization cones plus background star formation from the disk) we cannot say that the TO extended regions are regions of the disk where the AGN radiation has an influence. This is very different from the A scenario where the radiation is isotropically radiated or the B2 scenario in which the ionization cones intersect the galactic disk and the latter directly receives their

Table 4.6: Number of spaxels per galaxy corresponding to each BPT-type of object in the BPT-SII diagram: Seyfert (Sy), Star Forming (SF) and Anomalous (An). In the last column is the total number of spaxels per galaxy and in the last row the totals for the whole sample.

Galaxy	Sy	SF	An	Total
IC0485	21	23	1	45
IC0540	58	34	2	94
IC2247	116	233	9	358
IC4215	74	11	4	89
MCG-02-02-030	1	26	118	145
MCG-02-08-014	15	30	3	48
NGC0681	375	861	47	1283
NGC2410	92	460	6	558
NGC2916	6	1120	1	1127
NGC3160	31	0	0	31
NGC3182	34	166	6	206
NGC4644	10	190	0	200
NGC5216	107	0	0	107
NGC5378	34	21	1	56
NGC5957	25	1121	1	1147
NGC5971	55	71	3	129
NGC6394	52	190	3	245
UGC09110	62	1089	0	1151
Sample	1168	5646	205	7019

radiation. In this last case we would have true TO regions with both AGN and SF ionization in the same volume.

Because of our definition of R_i, we somewhat avoid these complications as we are not considering TO spaxels, but we cannot be sure also if the Seyfert spaxels that we see come from gas ionized in the galactic plane or from above it. If we are only interested in characterizing the size of the Narrow-Line Region (NLR) and the global reach of the AGN ionizing power, as is the case in this work, we would desire in fact to have Seyfert signal from the cones at the farthest distance possible from the SMBH. Therefore we stick to the definition of R_i taking into account the Seyfert spaxels out of the galactic plane for IC2247 and NGC0681. For face-on and deprojected galaxies, we can only take the R_i values of the central regions as lower limits. There is a possibility that the faraway Seyfert spaxels that we discarded as outliers and the TO spaxels are really part of the ionization cones, but again, we cannot be sure as we do not know the true three-dimensional shape of the cones.

4.3 Influence Radii From BPT-NII Maps

We determined the influence radii from the deprojected BPT-NII maps. As explained in the previous section, there were not enough spaxels with $SNR > 3$ in the required emission lines to determine the influence radius using the BPT-SII maps for most galaxies. The influence radius R_i, is defined as the distance from the centre to the farthest spaxel classified as Seyfert by the

Galaxy	R_i [arcsec]	R_i $[R/R_e]$	R_i [kpc]
IC0485	9.0 ± 1.0	0.3 ± 0.2	5.0 ± 2.0
IC0540	10.0 ± 1.0	0.5 ± 0.2	1.3 ± 0.8
IC2247	16.0 ± 1.0	0.7 ± 0.2	4.0 ± 1.0
IC4215	12.0 ± 1.0	0.7 ± 0.2	2.0 ± 1.0
MCG-02-02-030*	20.0 ± 1.0	1.1 ± 0.2	4.0 ± 1.0
MCG-02-08-014	14.0 ± 1.0	0.5 ± 0.2	4.0 ± 1.0
NGC0681	30.0 ± 1.0	0.9 ± 0.2	3.1 ± 0.8
NGC2410*	16.0 ± 1.0	0.6 ± 0.2	5.0 ± 1.0
NGC2916*	17.0 ± 1.0	0.6 ± 0.2	4.0 ± 1.0
NGC3160	8.0 ± 1.0	0.4 ± 0.2	4.0 ± 1.0
NGC3182	12.0 ± 1.0	0.5 ± 0.2	1.5 ± 0.8
NGC4644*	3.0 ± 1.0	0.2 ± 0.2	1.0 ± 1.0
NGC5216	17.0 ± 1.0	0.6 ± 0.2	3.0 ± 1.0
NGC5378*	15.0 ± 1.0	0.5 ± 0.2	3.0 ± 1.0
NGC5957*	10.0 ± 1.0	0.4 ± 0.2	1.1 ± 0.7
NGC5971*	9.0 ± 1.0	0.4 ± 0.2	2.0 ± 1.0
NGC6394	17.0 ± 1.0	0.7 ± 0.2	9.0 ± 2.0
UGC09110	18.0 ± 1.0	0.8 ± 0.2	6.0 ± 1.0

Table 4.7: Influence radii R_i as determined from the BPT-NII maps. The first column shows the name of the galaxy, with an * symbol signaling those which have outlier Seyfert spaxels. The second, third and fourth columns are the R_i in arcsec, normalized by the effective radius and in kpc, respectively.

BPT81 diagrams. The results are shown in table 4.7. There were galaxies (marked with an * symbol in the table) with outlier spaxels: those among them classified as Seyfert by the BPT-NII maps at large distances from the centre of their galaxies and not connected with the other Seyfert spaxels. Since these distant spaxels are frequently isolated as most spaxels around them were discarded because they have not enough signal-to-noise ratio both in the continuum or in any of the BPT emission lines (that is to say, they tend to be isolated in the maps), it is possible that they are just statistical noise (or that we cannot determinate their origin in any case, see the discussion in sections 4.2.3 and 4.2.4), so we treat them as outliers and exclude them of the influence radius estimation. We have to take the values of the measured influence radius as lower limits, especially for those galaxies with big gaps without spaxels close to the centre and those edge-on galaxies for which the BPT Seyfert spaxels extend out of the galactic planes, tracing the ionization cones.

The mean R_i of the sample is 3.5 kpc or 0.6 times the effective radii. This shows that in general, the AGN dominates the ionization of gas in kpc scales, comparable in magnitude to the effective radius, which implies that they can affect the physical conditions of their host galaxies far away from the nuclear regions, even for LLAGN (Seyfert 2).

Table 4.8: Results of the physical parameters of the SMBHs for each galaxy. In the second column there is the black hole mass, in the third column the luminosity of the [O III] λ5007 emission line, in the fourth column the bolometric luminosity and in the fifth column the accretion rate. The values for the black hole mass for NGC0681 and NGC5957 were not determined (see text).

Galaxy	$\log_{10}(M_{BH}/M_\odot)$	$\log_{10} L_{[O\ III]}$ [erg s^{-1}]	$\log_{10} L_{bol}$ [erg s^{-1}]	$\log_{10} \dot{m}$ [$M_\odot$ yr^{-1}]
IC0485	7.02 ± 0.22	41.81 ± 0.06	43.96 ± 0.06	-1.78 ± 0.06
IC0540	6.46 ± 0.28	41.02 ± 0.06	43.19 ± 0.06	-2.55 ± 0.06
IC2247	7.24 ± 0.24	41.69 ± 0.06	43.84 ± 0.06	-1.90 ± 0.06
IC4215	5.97 ± 0.29	41.59 ± 0.06	43.74 ± 0.06	-2.00 ± 0.06
MCG-02-02-030	6.90 ± 0.26	40.76 ± 0.06	42.91 ± 0.06	-2.83 ± 0.06
MCG-02-08-014	6.54 ± 0.26	40.57 ± 0.06	42.72 ± 0.06	-3.02 ± 0.06
NGC0681		40.37 ± 0.06	42.52 ± 0.06	-3.22 ± 0.06
NGC2410	7.28 ± 0.22	42.66 ± 0.06	45.32 ± 0.06	-0.42 ± 0.06
NGC2916	6.74 ± 0.24	41.56 ± 0.06	43.71 ± 0.06	-2.03 ± 0.06
NGC3160	7.76 ± 0.20	42.14 ± 0.06	44.80 ± 0.06	-0.94 ± 0.06
NGC3182	5.94 ± 0.33	41.49 ± 0.06	43.64 ± 0.06	-2.10 ± 0.06
NGC4644	6.32 ± 0.29	41.32 ± 0.06	43.47 ± 0.06	-2.27 ± 0.06
NGC5216	5.95 ± 0.31	40.88 ± 0.06	43.03 ± 0.06	-2.72 ± 0.06
NGC5378	5.22 ± 0.36	40.75 ± 0.06	42.90 ± 0.06	-2.84 ± 0.06
NGC5957		40.77 ± 0.06	42.92 ± 0.06	-2.82 ± 0.06
NGC5971	7.17 ± 0.23	40.97 ± 0.06	43.12 ± 0.06	-2.62 ± 0.06
NGC6394	6.89 ± 0.26	42.73 ± 0.06	45.39 ± 0.06	-0.36 ± 0.06
UGC09110	6.01 ± 0.33	41.00 ± 0.06	43.16 ± 0.06	-2.59 ± 0.06

4.4 Influence Radii and SMBH Physics

Table 4.8 shows the resulting physical parameters of the SMBHs and their activity, determined as explained in section 3.8. Masses could not be determined for NGC0681 nor NGC5957, for there were no available data in the CALIFA DR3 data products for their stellar velocity dispersions. Figure 4.3(a) characterizes the activity of the SMBHs. On the vertical axis we have the black hole mass M_{BH} and on the horizontal axis the bolometric luminosity L_{bol}. The diagonal lines represent different fractions of the *Eddington limit* which is a measure of the activity of the AGN: the actual luminosity (activity) respect to the maximum possible in order to maintain accretion equilibrium for a given value of M_{BH}. Most black holes in our sample are accreting matter at less than 10% of the Eddington limit, with only one case in the super-Eddington regime (on the right side of the solid-black diagonal line, which corresponds to galaxy NGC6394).

Figure 4.3(b) compares R_i with $\log_{10} M_{BH}$. Performing a least squares fitting, we obtained the relation:

$$\frac{R_i}{\text{kpc}} = (0.94 \pm 0.80) \left(\log_{10} \frac{M_{BH}}{\text{M}_\odot} \right) - (2.4 \pm 5.3) \tag{4.1}$$

with a high p-value $p = 0.2577$, which along with the extremely high uncertainties in the fitted slope and intercept, tells us that there is probably no relation between the mass of the SMBH

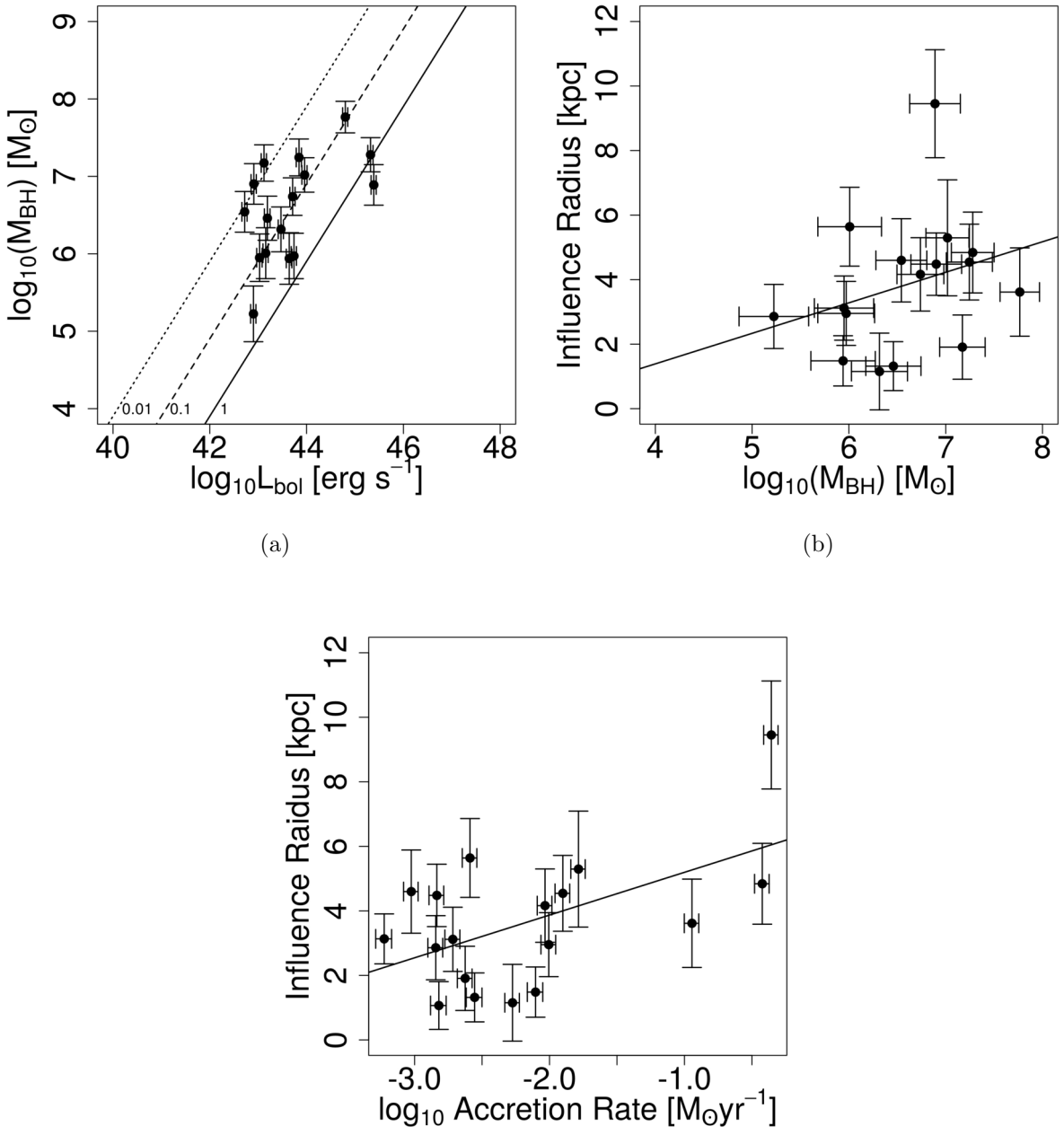

(a) (b)

(c)

Fig. 4.3: Characterization of the SMBH physical parameters and comparison with the influence radius. (a) Black hole mass *vs* bolometric luminosity. The Eddington limit, along with 0.1 and 0.01 fractions of it are represented by the black solid, dashed, and dotted lines, respectively. (b) Influence radius *vs* SMBH mass. The black line represents the least squares fitting result. (c) Influence radius *vs* SMBH accretion rate. The black line represents the least squares fitting result. The error bars in all plots represent 1σ uncertainties.

and R_i. This is expected since the AGN activity is related directly to the quantity of material being actually accreted per unit time (the accretion rate $\dot{m}$), which does depend of the available matter and not of the mass of the black hole itself.

Figure 4.3(c) compares R_i with the logarithm of the accretion rate ($\log_{10} \dot{m}$). For this we obtain the relation:

$$\frac{R_i}{\text{kpc}} = (1.32 \pm 0.51) \left(\log_{10} \frac{\dot{m}}{\text{M}_\odot \text{ yr}^{-1}} \right) + (6.52 \pm 1.88) \tag{4.2}$$

with a p-value $p = 0.01992$, which is a much more reasonable fit with also reasonable uncertainties for the fitted slope and intercept than in the case of R_i *vs* M_{BH}. This suggests, as one would expect, that a correlation might exist between the AGN activity, (i.e. the SMBH accretion rate) and R_i.

Let us now consider the implications of the kpc scales that R_i reaches. The fact that the latter correlation is reasonable but not perfect (the p-value is still somewhat high), could be a consequence of low-number statistics, but also can be related to the fact that in general AGN activity tends to be variable. Variability effects could affect the ionization of gas at the distances of the ionizing radius after tens of thousands of years of light-travel time, so the activity that we measure with the bolometric luminosity of the central spaxels may not be the same as the activity that the AGN had when the photons that are currently at the distance of the influence radius (and all the way in between) were emitted. In this scenario, the influence radius should be a variable quantity dependent on the AGN ionizing continuum luminosity L_{ion}, with a delay time of the variation in the radius respect to variations in the continuum proportional to the radius size.

It is remarkable the case of NGC5378, with $M_{BH} = 5.22 \pm 0.36$ M$_\odot$, is compatible with the upper limit of what would be considered an *intermediate-mass black hole (IMBH)*, which is $M_{BH} \approx 10^5$ M$_\odot$ (see Mediavilla et al. 2017 and Ebisuzaki et al. 2001). Since they are objects with an interest on their own, being considered possible precursors of SMBHs (Zwart et al. 1999; Oka et al. 2017), this IMBH candidate should be addressed in future works in order to verify the value of M_{BH} with independent methods.

4.5 Influence Radius and Host Galaxy Morphology

Here we compare the influence radii with two of the host galaxies morphological parameters: the morphological type and the effective radius. Based initially on the Hubble-type classification in the CALIFA DR3 dataproducts (see table 2.1), we regrouped the sample into broader categories, which are defined as follows by Morales et al. (in preparation), based on Sandage et al. (1970) and Sandage (1975): Hubble types E0 to E7 are classified as *ellipticals* (E); *lenticular* S0 galaxies maintain the same designation; spirals from Sa up to Sb and the correspondent barred SBa to SBb are classified as *early spirals* (ES and ESB respectively); finally Hubble types Sbc and later, and the correspondent SBb and later barred spirals, are classified as *late spirals* (LS and LSB respectively). There are no irregular nor peculiar galaxies in the sample. The resulting classification for each galaxy is shown in table 4.9.

In figure 4.4(a) we show the influence radius vs morphology. An apparent trend of the influence radius getting higher towards latter Hubble types can be seen. We have to worry here about low-number statistics, because besides the fact that we have a small sample (only 18 galaxies), most of them are early spirals, with only two ellipticals and two late spirals, and no S0s. Therefore we cannot make firm conclusions from this plot, but certainly this is a motivation to explore this possibility with a larger sample in the future.

Table 4.9: Classification by morphology. Categories are: E (elliptical), S0 (lenticular), ES (early spiral), ESB (barred early-spiral), LS (late spiral) and LSB (barred late-spiral). See text for a more complete description.

Galaxy	Morphology
IC0485	ESB
IC0540	ESB
IC2247	ES
IC4215	ES
MCG-02-02-030	ESB
MCG-02-08-014	ES
NGC0681	ESB
NGC2410	ESB
NGC2916	LS
NGC3160	ESB
NGC3182	E
NGC4644	ES
NGC5216	E
NGC5378	ESB
NGC5957	ESB
NGC5971	ESB
NGC6394	LSB
UGC09110	ESB

Another important aspect of morphology is the presence or absence of bars. It has been suggested since the 1970s (see the review by Kormendy & Kennicutt Jr 2004, and references there in) that bars can contribute to transport gas from the disk into the central regions, allowing for the presence of rings of intense nuclear star formation. One of the best known examples is that of NGC1512 for which the material introduced by the bar forms a starburst ring (Ma et al. 2017). If this material manages to get inside the SMBH gravitational zone of influence, it can get accreted and in consequence, the luminosity of the accretion disk can be increased. In figure 4.4(a), we can see that the four galaxies with the largest influence radii are all barred spirals (in colour red). Figure 4.4(b) compares morphology with the accretion rate $\dot{m}$, which as we saw in the previous section, is directly related to the size of R_i. We can see that barred spirals (again, in red) can reach $\dot{m}$ values more than one order of magnitude above other morphological types. The result is compatible with figure 4.4(a): the four galaxies with the larger accretion rates are all barred.

It seems that due to the presence of a bar, barred spirals have the possibility to feed the SMBH with more gas than non-barred galaxies, and hence, can produce larger R_i. Again, we are dealing here with low number statistics, and there could be a bias given the fact that most spirals in the sample are barred (see table 4.9). Further analysis with a larger sample of galaxies of a larger variety of morphological types would be useful to confirm this trend.

In figure 4.5, we compare the influence radius with the *effective radius* R_e, defined as the radius that contains half of the total flux of the galaxy (in general, for a given photometric band, in our case the SDSS DR7 r band). Applying a least squares fit,we find the relation:

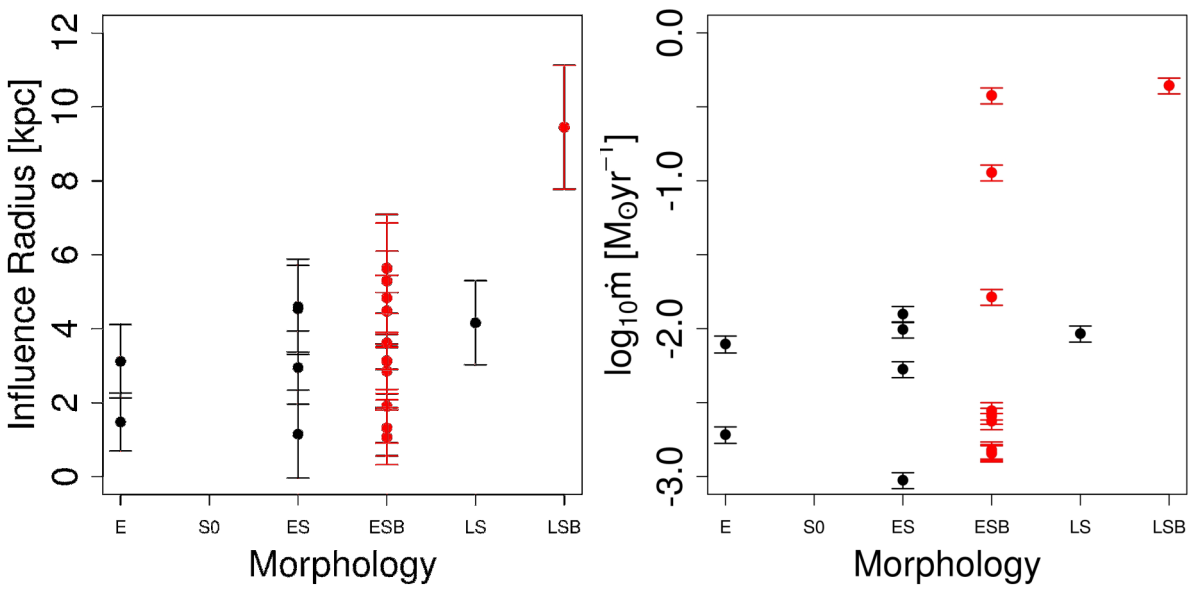

(a) (b)

Fig. 4.4: (a) Influence radius vs morphology. (b) Accretion rate vs morphology. Red dots are barred galaxies.

$$\frac{R_i}{\text{kpc}} = (0.342 \pm 0.087)\frac{R_e}{\text{kpc}} + (1.34 \pm 0.69) \tag{4.3}$$

with a p-value $p = 0.001184$. This indicates a clear correlation, but interpretation of causality and physics is a tricky one. We know from the well established scaling relations that the mass of the SMBH is related to the mass of the bulge (see Häring & Rix 2004). The bulge is a great contributor to the stellar radiation flux of galaxies and hence, dominating within the effective radius, especially for early type spirals. Therefore, there could be an indirect correlation of the black hole mass with effective radii. Nevertheless, we already saw that the SMBH mass is not determining (if it plays any role at all) for the size of R_i.

4.6 The Search for AGN-Driven Outflow Candidates

Here we present results of the search for candidates to AGN-driven outflows performed on the sample. As this is not the main aim of this thesis work (focused on the influence radii), we present here very briefly only preliminary (although very promising) results.

A search for blue-shifted components of the Hα and [O III] λ5007 emission lines was performed as explained in section 3.9. As a result, maps were produced of the specific surface flux and line-of-sight velocities of these blue-shifted components: the results for Hα are shown respectively in appendix A, figures A.15 and A.16. Figures A.17 and A.18 show the surface specific flux and line-of-sight velocity maps, respectively, for [O III] λ5007. Notice that the maps were not deprojected in order to compare them with the background SDSS pictures indicating the distribution of stars in each galaxy.

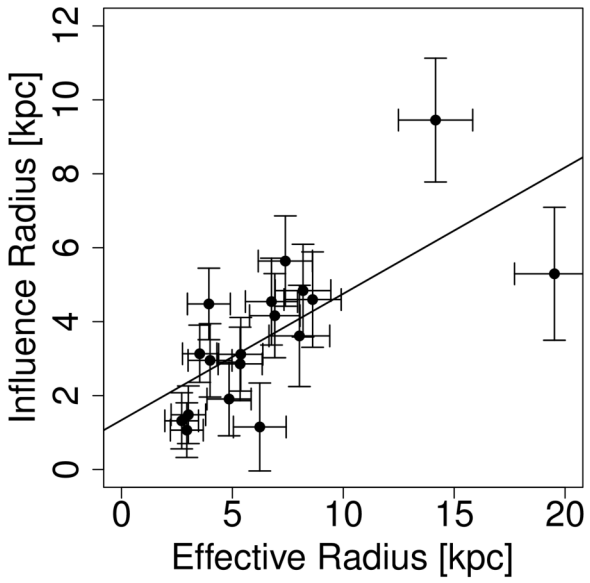

Fig. 4.5: Influence radius *vs* effective radius.

For all cases, the flux is stronger in the Hα line, which allows us to see the spatial distribution of the emission more clearly than for the [O III] λ5007 line, therefore we will use the Hα emission as our primary indicator. While many galaxies show some degree of blue-shifted component Hα emission, for many of them (e.g. IC2247, NGC2916, NGC4644, NGC5957) it just appears to follow the shape of the disk and the spiral arms. This could mean that we are seeing just a component of the interstellar gas rotating at a different velocity than the rest of the disk, or even in the opposite direction in the case of NGC5957, if we compare with the kinematic map in figure A.2(o). Even more interestingly, this disk emission could be associated to the presence of star-formation driven outflows. Despite this being an interesting possibility, which could be addressed in future work, we will focus here only on the AGN-driven outflow candidates.

To identify an AGN-driven outflow candidate, we require the Hα emission to be associated to the central regions. This is the case for IC0485, IC0540, IC4215, MCG-02-02-030, MCG-02-08-014, NGC0681 and IGC09110. Due to the low signal-to-noise ratio (SNR), we have very few spaxels available in some cases, so the shape of the supposed outflow cannot be traced.

Now we will focus on the cases of MCG-02-02-030 and NGC0681, our two more solid candidates. Both present large blue-shifted component emission regions that clearly extend (somewhat perpendicularly) out of the galactic disk (up to distances of $\approx$ 5 kpc in the case of MCG-02-02-030 and $\approx$ 3.5 kpc in the case of NGC0681). Both possible outflows present some knots with higher Hα fluxes than the surroundings. In the case of NGC0681, it is very straightforward to glimpse how the outflow is beam-shaped, from the galactic centre and out of the galactic plane. This is our most solid candidate. It possesses two emission knots, one located at a projected distance of $\approx$ 2 kpc and the other at $\approx$ 3 kpc from the galactic centre, both with line-of-sight velocities of ≈ -300 km s^{-1}. In the case of MCG-02-02-30, the knot is at a projected distance of $\approx$ 5 kpc from the galactic centre, also with a line-of-sight velocity of ≈ -300 km s^{-1}.

The presence of outflows is a very important factor in the feedback processes, injecting momentum into the interstellar medium and even into the intergalactic medium. Given our results for both the search of outflow candidates and the determination of influence radii reaching kiloparsec scales, future work should address the problem to separate effectively the contribution of both radiation and outflows (via shocks) to the ionization of gas in the host galaxies.

Chapter 5

Conclusions and Comments on Future Work

In this work, we measured the size of the region photoionized by Seyfert 2 AGN in their host galaxies using IFS data from the CALIFA survey. For this we defined the *influence radius* R_i as the distance from the galactic centre to the farthest spaxel classified as Seyfert by the BPT-NII diagrams as a proxy for the size of such region. In order to accomplish this we:

- Selected 18 galaxies from the CALIFA DR3 sample.
- Used STARLIGHT to fit synthetic spectra to each spaxel.
- Measured the fluxes and widths of the emission lines relevant for the BPT81 diagrams, including reddening corrections using the CCM89 extinction law.
- Used the Hα emission lines to elaborate kinematic maps in order to verify and correct positions of the galactic centres given by the CALIFA DR3, in order to locate the position of the SMBH.
- Proposed a new limit for the BPT-NII and BPT-SII diagrams in order to separate the AGN Seyfert 2 emission from anomalous low-ionization emission for IFS data of Seyfert 2 galaxies.
- Plotted (deprojected when it was possible) BPT-NII and BPT-SII diagrams, maps and radial profiles (of the emission-line ratios) for each galaxy in the sample, and used them to measure R_i.
- Compared R_i with physical parameters of the SMBH (mass of the black hole M_{BH} and accretion rate $\dot{m}$) and with morphological characteristics of the host galaxies (morphology and effective radius).
- Performed a search for possible AGN-driven outflows looking for blue-shifted components of the Hα and [O III] λ5007 emission lines.

As a result, our **main conclusions** are the following:

- Seyfert 2 AGN dominate the gas ionization of their host galaxies up to distances (R_i) of the order of kiloparsecs, with a mean of $R_i = 3.5$ kpc or $R_i/R_e = 0.6$ for the sample.

- We observed that the influence radius depends on the accretion rate $\dot{m}$ of the SMBH and might be related to the host galaxy morphology, with late type spirals and especially barred spirals potentially reaching higher values of R_i. Nevertheless, this is based on low-number statistics and a future study with a bigger sample is needed to confirm or reject this.

In the process, we also learned that:

- The limit between Seyfert and LINER class in BPT diagrams of Seyfert galaxies, when applied to spatially resolved data (i.e. IFU), must be modified in order to account for the presence of many spaxels with spectra showing ionization by the AGN, falling in the LINER region of the diagrams (because we do not have LINER), and to separate them from anomalous spaxels with high values of low-ionization line ratios which could be related to other physical processes or measurement errors. We proposed such limits for the BPT-NII and BPT-SII diagrams.

- Once such modifications are made, BPT81 maps can be effectively used to determine the zones dominated or influenced by Seyfert 2 AGN ionizing radiation over their host galaxies.

- In general, our results apparently favour the scenario with AGN ionizing radiation propagating inside ionization cones, in concordance with the unified model (scenarios B1 and B2), but including the presence of a clumpy structure for the dusty torus.

- It is important to understand the nature of the TO spaxels. They could be both a projection in the line-of-sight of the ionization cones over the galactic disk (in which case they could be included in R_i determinations), as presented in scenario B1 which is favoured by the BPT81 maps of the edge-on galaxies IC2247 and NGC0681, or a true region of the disk ionized both by stars and the AGN (scenario B2) which is favoured by the BPT81 maps of face-on/deprojected galaxies MCG-02-02-030, NGC2410, NGC6394. The situation appears to vary from galaxy to galaxy, depending on the orientation of the SMBHs accretion disk and the dusty torus with respect to the hosts galactic plane.

We also found the following issues that should be addressed in future works:

- A good coverage of the maps with spaxels with enough SNR is necessary in order to understand correctly the shape of the ionized region. The lack of enough coverage in the BPT-SII maps and in some of the BPT-NII maps, which is probably due to the limited sensitivity of the instrument, made us to discard the determination of R_i with the former, and take the ones determined with the latter as lower limits in many cases. Given that IFU data is limited by the two-dimensional projection into the plane of the sky, or (if deprojection is feasible) into the plane of the disk, we need more information (possibly from observations in other spectral ranges) in order to determine the true three-dimensional shape of this region and to reveal the true shape of the ionization regions.

- Related with the former, we lost a lot of spaxels in the search for blue-shifted components, due to very low SNR of the emission lines. This is due to a combination of limited spectral resolution and flux sensitivity; we were almost at the limit of what was possible with the data. For future work with outflows, data from bigger telescopes and higher spectral resolution instruments would be recommendable.

- Since we found some candidates for AGN-driven outflows, the outflow contribution to the gas ionization in those galaxies via shocks should be addressed in future work, in order to separate it from the direct AGN photoionization, which would help in getting a better understanding of the feedback processes.
- The central black hole in NGC5378, with a mass $M_{BH} = 5.22 \pm 0.36$ $M_{\odot}$ is a candidate for IMBH and as such, it should be studied further with other methods to confirm this result.

Bibliography

Abazajian, K. N., Adelman-McCarthy, J. K., Agüeros, M. A., et al. 2009, The Astrophysical Journal Supplement Series, 182, 543

Antonucci, R. 1993, Annual review of astronomy and astrophysics, 31, 473

Asari, N., Cid Fernandes, R., Stasińska, G., et al. 2007, Monthly Notices of the Royal Astronomical Society, 381, 263

Baldwin, J., Phillips, M., & Terlevich, R. 1981, Publications of the Astronomical Society of the Pacific, 5

Barnes, E. I., & Sellwood, J. A. 2003, The Astronomical Journal, 125, 1164

Blandford, R. 1993, Astrophysical Jets

Brocklehurst, M. 1971, Monthly Notices of the Royal Astronomical Society, 153, 471

Burkert, A., Genzel, R., Bouché, N., et al. 2010, The Astrophysical Journal, 725, 2324

Cardelli, J. A., Clayton, G. C., & Mathis, J. S. 1989, The Astrophysical Journal, 345, 245

Catalán-Torrecilla, C., Gil de Paz, A., Castillo-Morales, A., et al. 2015, Astronomy & Astrophysics, 584, A87

Cid Fernandes, R., Gu, Q., Melnick, J., et al. 2004, Monthly Notices of the Royal Astronomical Society, 355, 273

Cid Fernandes, R., Mateus, A., Sodré, L., Stasińska, G., & Gomes, J. M. 2005, Monthly Notices of the Royal Astronomical Society, 358, 363

Coziol, R., Andernach, H., Torres-Papaqui, J. P., Ortega-Minakata, R. A., & Moreno del Rio, F. 2017, Monthly Notices of the Royal Astronomical Society, 466, 921

Debuhr, J., Quataert, E., & Ma, C.-P. 2011, Monthly Notices of the Royal Astronomical Society, 412, 1341

DeBuhr, J., Quataert, E., & Ma, C.-P. 2012, Monthly Notices of the Royal Astronomical Society, 420, 2221

Ebisuzaki, T., Makino, J., Tsuru, T. G., et al. 2001, The Astrophysical Journal Letters, 562, L19

Elitzur, M., & Shlosman, I. 2006, The Astrophysical Journal Letters, 648, L101

Faucher-Giguère, C.-A., & Quataert, E. 2012, Monthly Notices of the Royal Astronomical Society, 425, 605

Fernandes, R. C., Stasińska, G., Schlickmann, M., et al. 2010, Monthly Notices of the Royal Astronomical Society, 403, 1036

Genzel, R., Schreiber, N. M. F., Übler, H., et al. 2017, Nature, 543, 397

Häring, N., & Rix, H.-W. 2004, The Astrophysical Journal Letters, 604, L89

Ho, L. C. 2008, Nuclear Activity in Nearby Galaxies, Tech. Rep. arXiv:0803.2268

Kaiser, C. R., & Alexander, P. 1997, Monthly Notices of the Royal Astronomical Society, 286, 215

Kara, E., Alston, W. N., Fabian, A. C., et al. 2016, Monthly Notices of the Royal Astronomical Society, 462, 511

Kauffmann, G., Heckman, T. M., Tremonti, C., et al. 2003, Monthly Notices of the Royal Astronomical Society, 346, 1055

Kewley, L. J., Dopita, M., Sutherland, R., Heisler, C., & Trevena, J. 2001, The Astrophysical Journal, 556, 121

Kewley, L. J., Groves, B., Kauffmann, G., & Heckman, T. 2006, Monthly Notices of the Royal Astronomical Society, 372, 961

Kormendy, J., & Kennicutt Jr, R. C. 2004, Annu. Rev. Astron. Astrophys., 42, 603

Koski, A. T. 1978, The Astrophysical Journal, 223, 56

Lamastra, A., Bianchi, S., Matt, G., et al. 2009, Astronomy & Astrophysics, 504, 73

López-Sánchez, Á. R., Mesa-Delgado, A., López-Martín, L., & Esteban, C. 2011, Monthly Notices of the Royal Astronomical Society, 411, 2076

Ma, C., de Grijs, R., & Ho, L. C. 2017, The Astrophysical Journal Supplement Series, 230, 7pp

Maiolino, R., Russell, H. R., Fabian, A. C., et al. 2017, Nature, 544, 202

McConnell, N. J., & Ma, C.-P. 2013, The Astrophysical Journal, 764, 184

Mediavilla, E., Jiménez-Vicente, J., Muñoz, J., Vives-Arias, H., & Calderón-Infante, J. 2017, The Astrophysical Journal Letters, 836, L18

Mejía-Restrepo, J. E., Trakhtenbrot, B., Lira, P., Netzer, H., & Capellupo, D. M. 2016, Monthly Notices of the Royal Astronomical Society, 460, 187

Mosquera, A. M., Kochanek, C. S., Chen, B., et al. 2013, The Astrophysical Journal, 769, 53

Netzer, H. 2013, The Physics and Evolution of Active Galactic Nuclei (Cambridge University Press)

Oka, T., Tsujimoto, S., Iwata, Y., Nomura, M., & Takekawa, S. 2017, Nature Astronomy

Ortega-Minakata, R. A., Torres-Papaqui, J. P., Andernach, H., & Islas-Islas, J. M. 2014, in IAU Symposium, Vol. 306, Statistical Challenges in 21st Century Cosmology, ed. A. Heavens, J.-L. Starck, & A. Krone-Martins, 362–364

Osterbrock, D. E., & Ferland, G. J. 2006, Astrophysics of gaseous nebulae and active galactic nuclei

Palunas, P., & Williams, T. B. 2000, The Astronomical Journal, 120, 2884

Peimbert, M., Peimbert, A., & Delgado-Inglada, G. 2017, arXiv preprint arXiv:1705.06323

Peterson, B. M. 1997, An Introduction to Active Galactic Nuclei

Riffel, R. A., Storchi-Bergmann, T., & McGregor, P. J. 2009, The Astrophysical Journal, 698, 1767

Ruiz, M., Efstathiou, A., Alexander, D., & Hough, J. 2001, Monthly Notices of the Royal Astronomical Society, 325, 995

Rupke, D. S., & Veilleux, S. 2011, The Astrophysical Journal Letters, 729, L27

Sánchez, S., García-Benito, R., Zibetti, S., et al. 2016a, Revista mexicana de astronomía y astrofísica

Sánchez, S. F., García-Benito, R., Zibetti, S., et al. 2016b, Revista mexicana de astronomía y astrofísica, A

Sandage, A. 1975, Classification and Stellar Content of Galaxies Obtained from Direct Photography, ed. A. Sandage, M. Sandage, & J. Kristian (the University of Chicago Press), 1

Sandage, A., Freeman, K. C., & Stokes, N. R. 1970, The Astrophysical Journal, 160, 831

Sarzi, M., Shields, J. C., Schawinski, K., et al. 2010, Monthly Notices of the Royal Astronomical Society, 402, 2187

Sharp, R. G., & Bland-Hawthorn, J. 2010, The Astrophysical Journal, 711, 818

Silverman, B. 1986, Density Estimation for Statistics and Data Analysis (Chapman & Hall/CRC), 48

Singh, R., Van de Ven, G., Jahnke, K., et al. 2013, Astronomy & Astrophysics, 558, A43

Storchi-Bergmann, T., Lopes, R. D. S., McGregor, P. J., et al. 2010, Monthly Notices of the Royal Astronomical Society, 402, 819

Storchi-Bergmann, T., McGregor, P. J., Riffel, R. A., et al. 2009, Monthly Notices of the Royal Astronomical Society, 394, 1148

Strauss, M. A., Huchra, J. P., Davis, M., et al. 1992, The Astrophysical Journal Supplement Series, 83, 29

Torres-Papaqui, J. P., Coziol, R., Andernach, H., et al. 2012, Revista mexicana de astronomía y astrofísica, 48, 275

Urry, C. M., & Padovani, P. 1995, Publications of the Astronomical Society of the Pacific, 107, 803

Uttley, P., Cackett, E. M., Fabian, A. C., Kara, E., & Wilkins, D. R. 2014, Astronomy & Astrophysics Reviews, 22, 72

Véron-Cetty, M.-P., & Véron, P. 2006, Astronomy & Astrophysics, 455, 773

Wada, K. 2012, The Astrophysical Journal, 758, arXiv:1208.5272v1

Wada, K., Schartmann, M., & Meijerink, R. 2016, The Astrophysical Journal Letters, 828, L19

Wuyts, S., Schreiber, N. M. F., Wisnioski, E., et al. 2016, KMOS 3D: Dynamical constraints on the mass budget in early star-forming disks

Zwart, S. P., Makino, J., McMillan, S. L. W., & Hut, P. 1999, Star cluster ecology III: Runaway collisions in young compact star clusters

Appendix A

Results: Diagrams and Maps

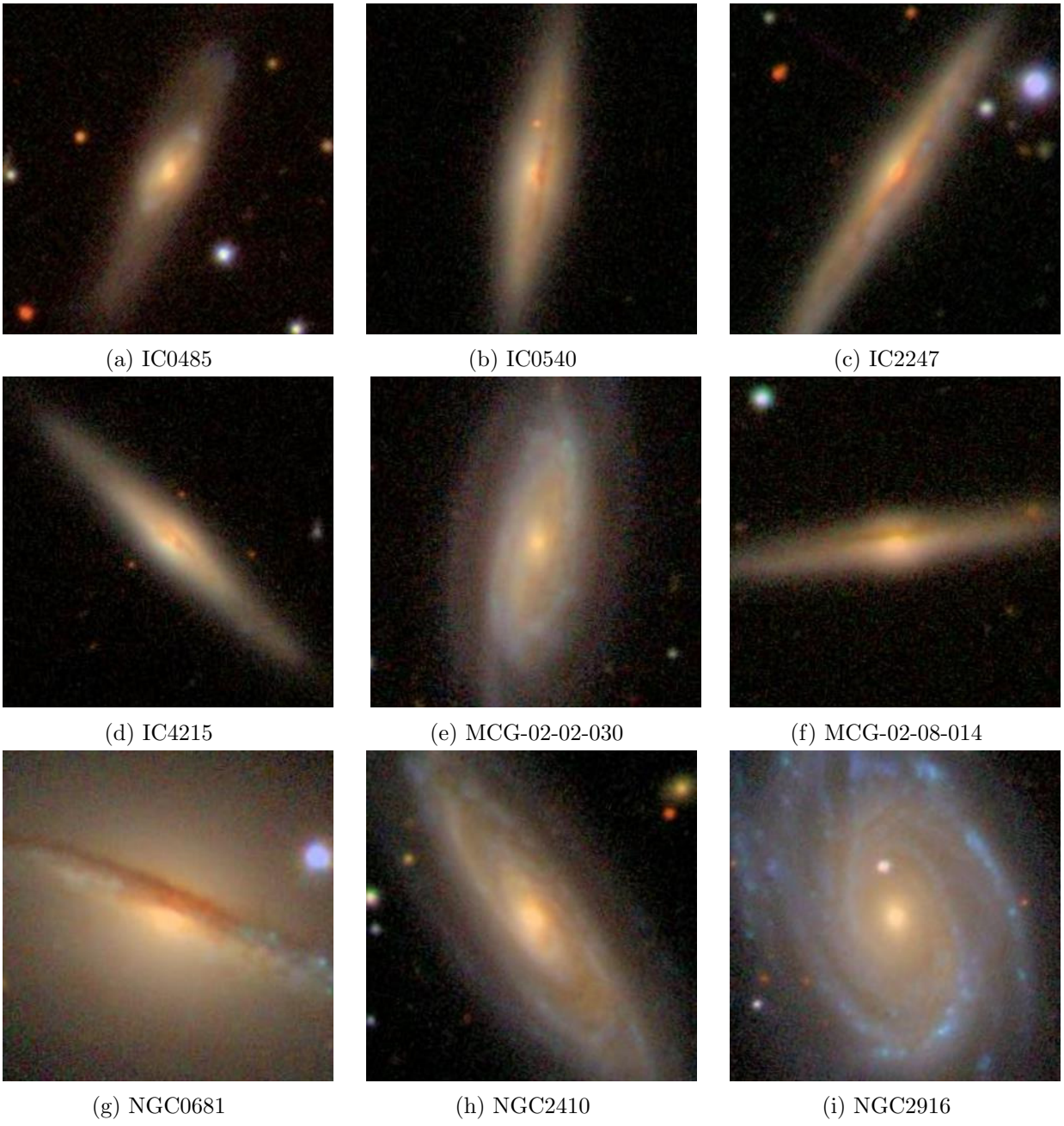

(a) IC0485 (b) IC0540 (c) IC2247

(d) IC4215 (e) MCG-02-02-030 (f) MCG-02-08-014

(g) NGC0681 (h) NGC2410 (i) NGC2916

Fig. A.1: Images of the galaxies in our sample from SDSS DR7. North is up and East is to the left. Each image is 80" on side.

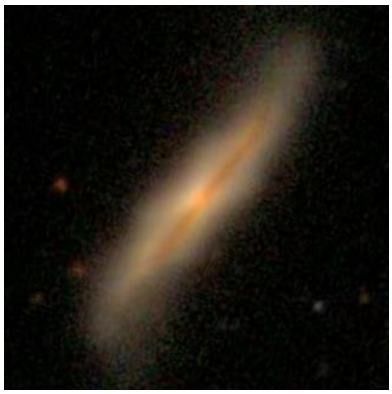

(j) NGC3160

(k) NGC3182

(l) NGC4644

(m) NGC5216

(n) NGC5378

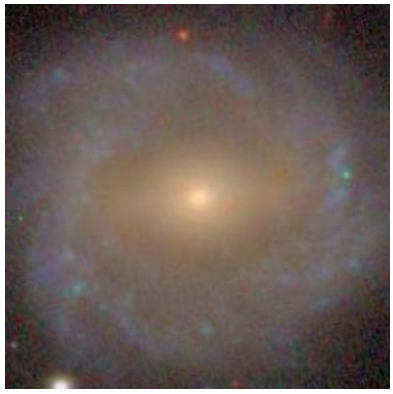

(o) NGC5957

(p) NGC5971

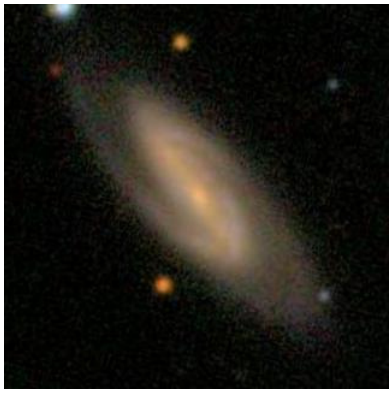

(q) NGC6394

(r) UGC09110

Fig. A.1: Images of the galaxies in our sample from SDSS DR7 (continued).

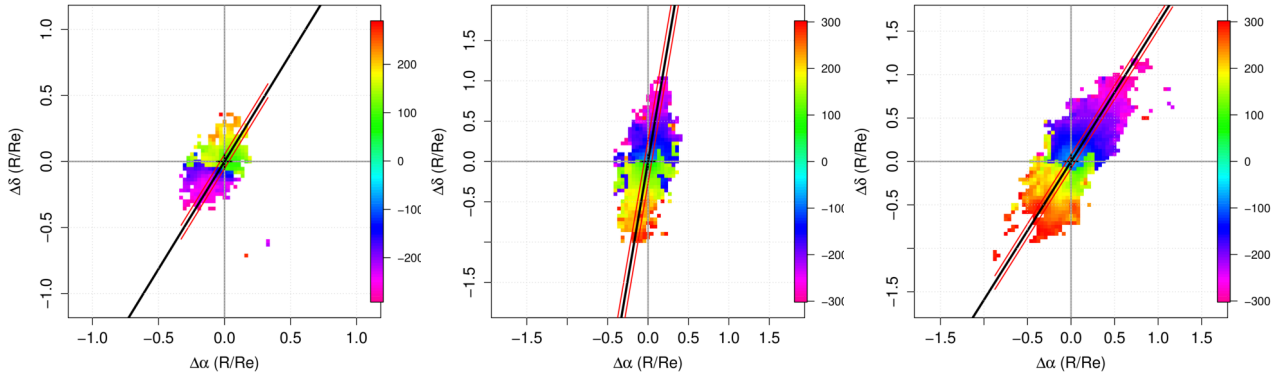

(a) IC0485 (b) IC0540 (c) IC2247

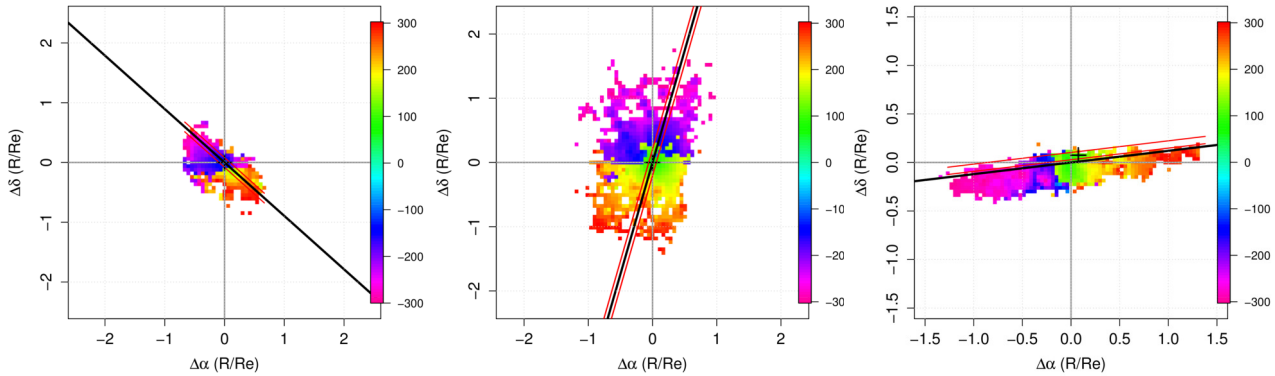

(d) IC4215 (e) MCG-02-02-030 (f) MCG-02-08-014

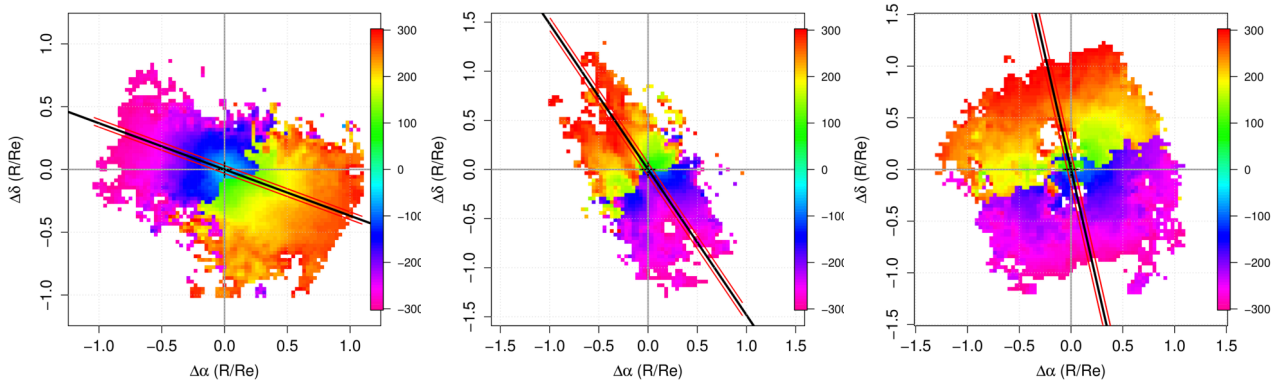

(g) NGC0681 (h) NGC2410 (i) NGC2916

Fig. A.2: Rotation velocity maps. The CALIFA photometric centre (from SDSS images) is at coordinates (0,0), and the found kinematic rotation centre is marked with a black cross. The black line is the diagonal associated with the major axis and the position angle, and the area between the red lines contain the spaxels used in the rotation velocity profile. Rotation velocity is in the rest frame of each galaxy, and in the colour scale are in km s^{-1} and distances in right ascension and declination are normalized to the effective radius.

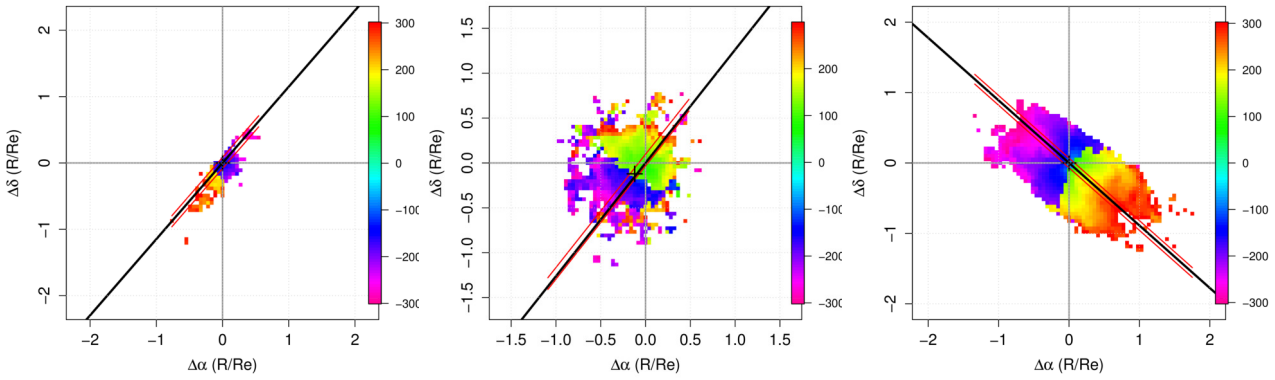

(j) NGC3160 (k) NGC3182 (l) NGC4644

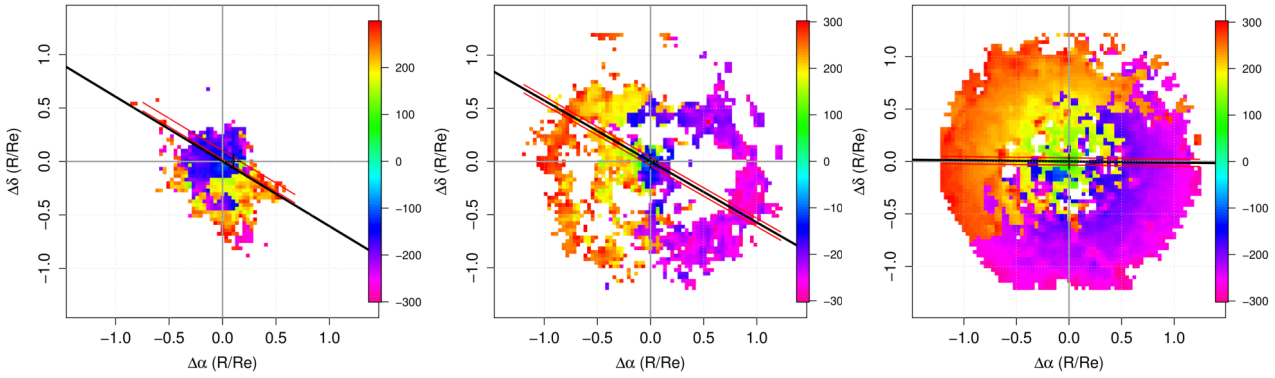

(m) NGC5216 (n) NGC5378 (o) NGC5957

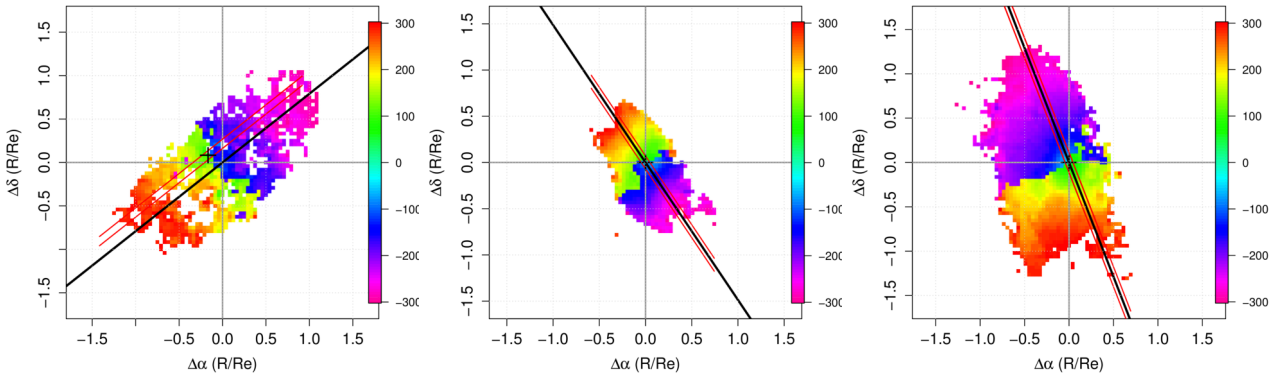

(p) NGC5971 (q) NGC6394 (r) UGC09110

Fig. A.2: Rotation velocity maps. Continued.

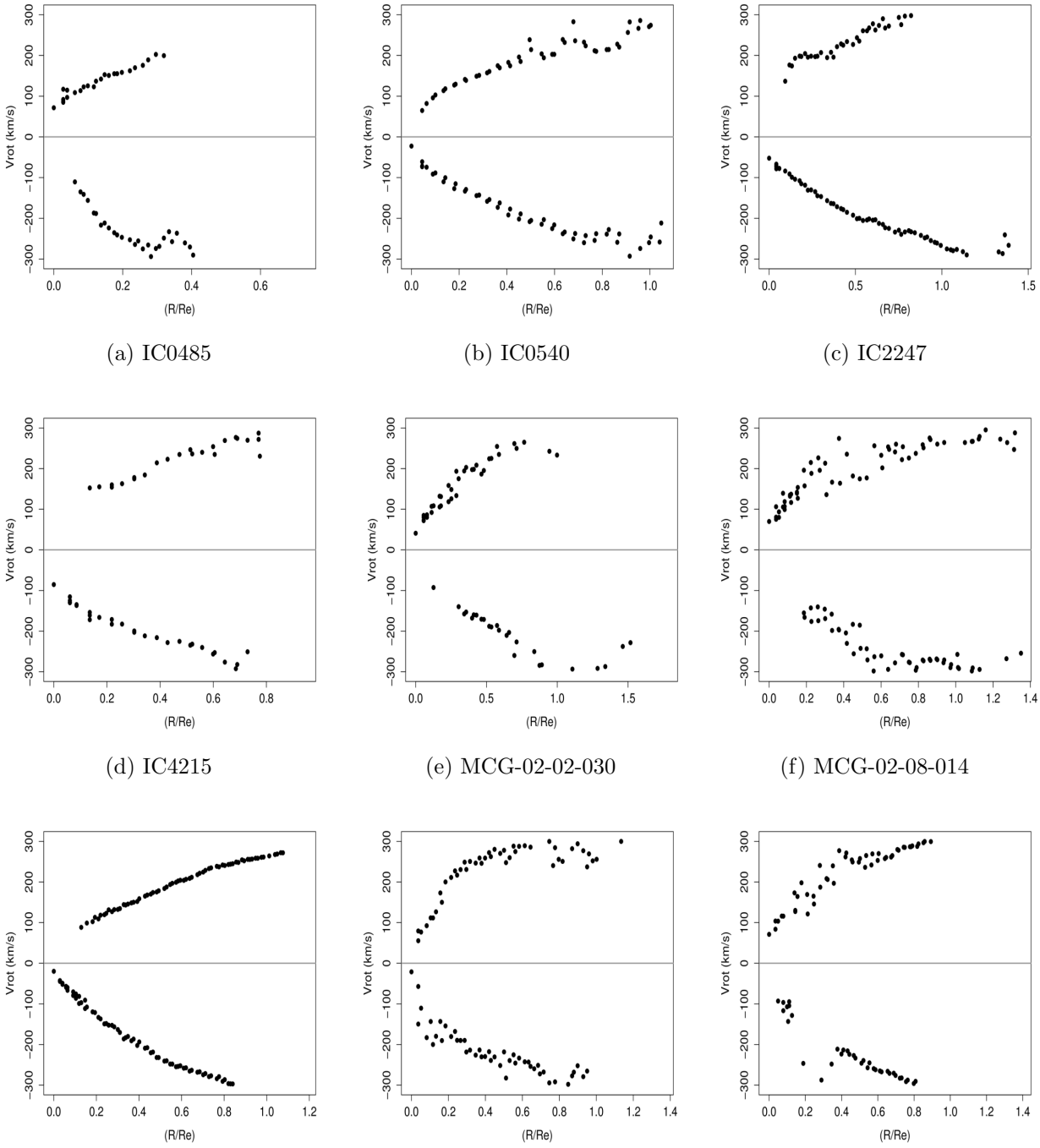

(a) IC0485 (b) IC0540 (c) IC2247

(d) IC4215 (e) MCG-02-02-030 (f) MCG-02-08-014

(g) NGC0681 (h) NGC2410 (i) NGC2916

Fig. A.3: Rotation velocity profiles along the major axis, tracing the rotation curves. The dots are the spaxels contained between the red lines in the maps of figure A.2.

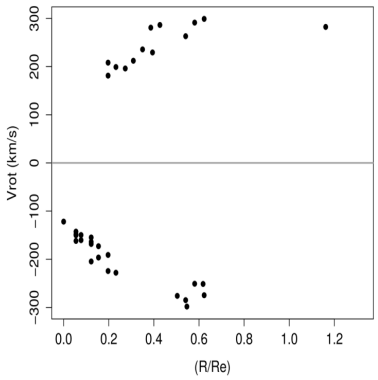

(j) NGC3160

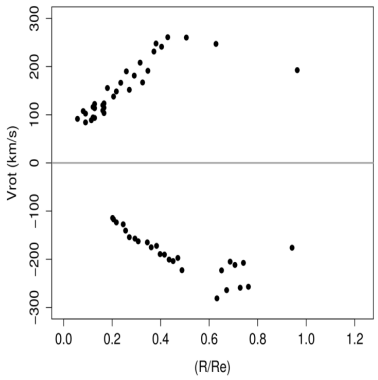

(k) NGC3182

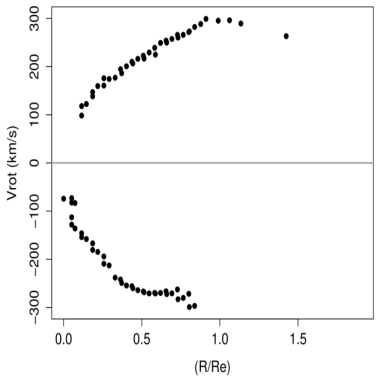

(l) NGC4644

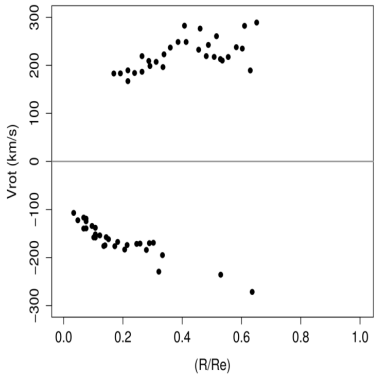

(m) NGC5216

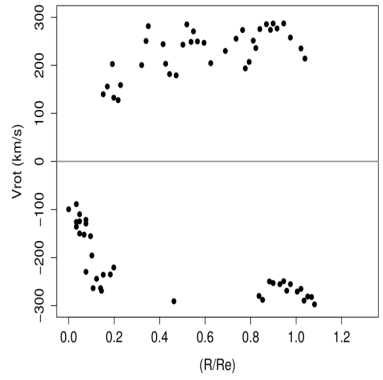

(n) NGC5378

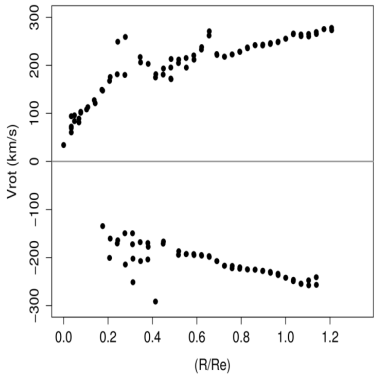

(o) NGC5957

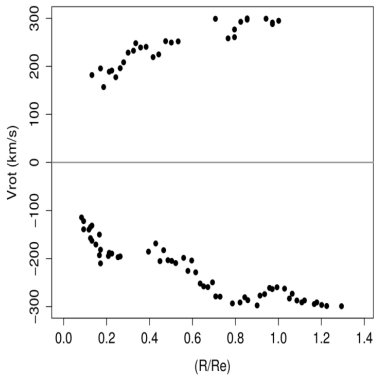

(p) NGC5971

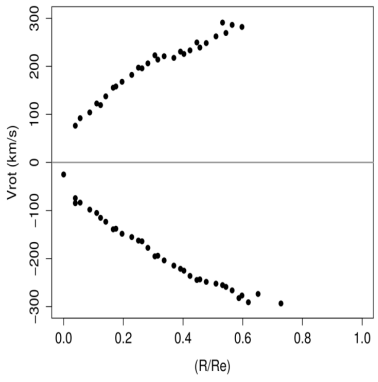

(q) NGC6394

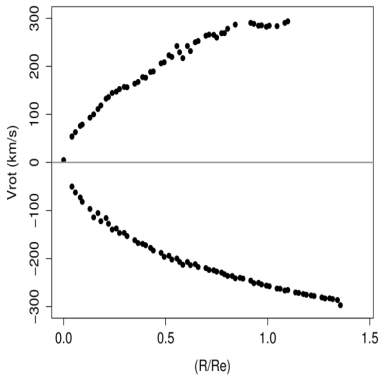

(r) UGC09110

Fig. A.3: Rotation velocity profiles along the major axis. Continued.

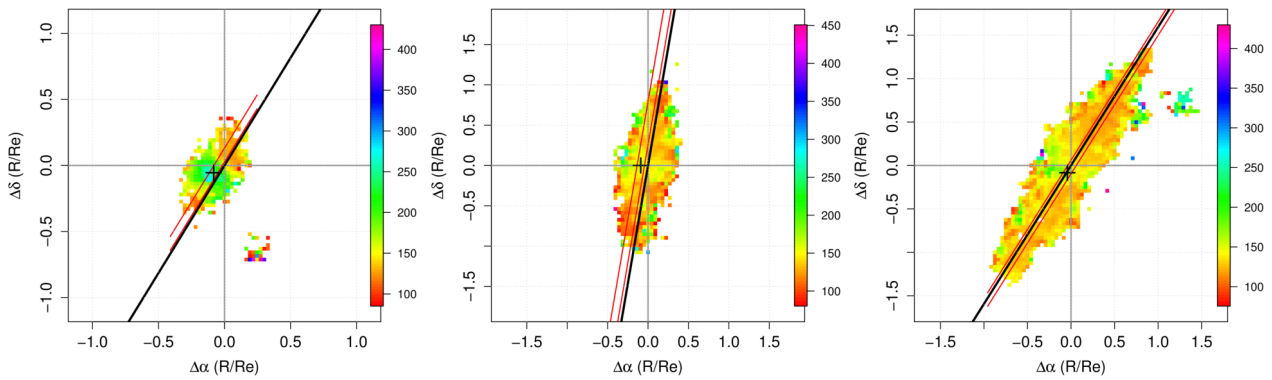

(a) IC0485 (b) IC0540 (c) IC2247

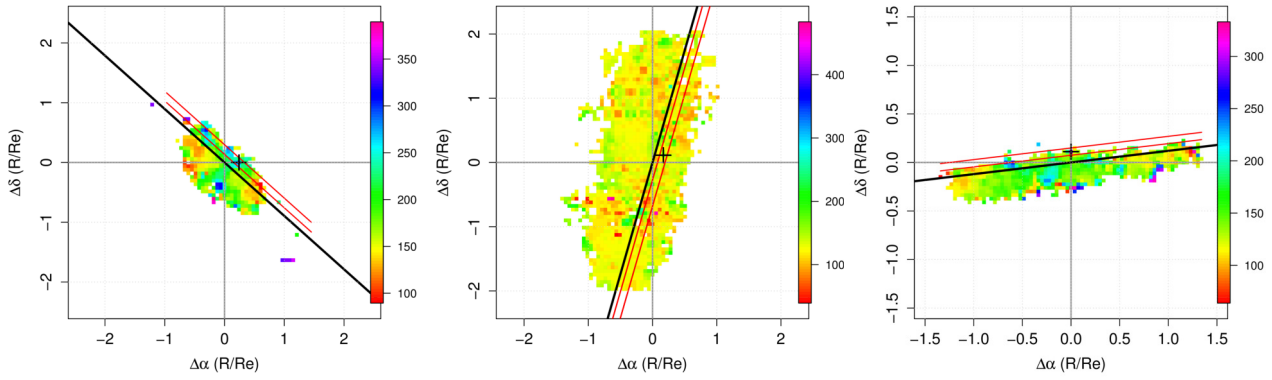

(d) IC4215 (e) MCG-02-02-030 (f) MCG-02-08-014

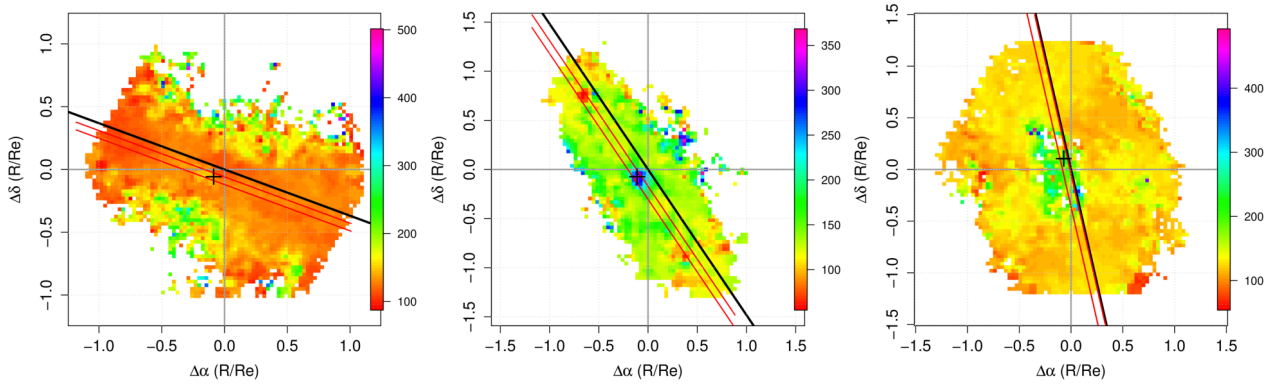

(g) NGC0681 (h) NGC2410 (i) NGC2916

Fig. A.4: Velocity dispersion maps. The black line marks the direction of the position angle along the major axis. The CALIFA photometrically determined centre (from SDSS) is at coordinates (0,0). The black cross marks the maximum velocity dispersion spaxel near the centre. The red lines contain the spaxels used for the velocity dispersion profiles in figure A.5

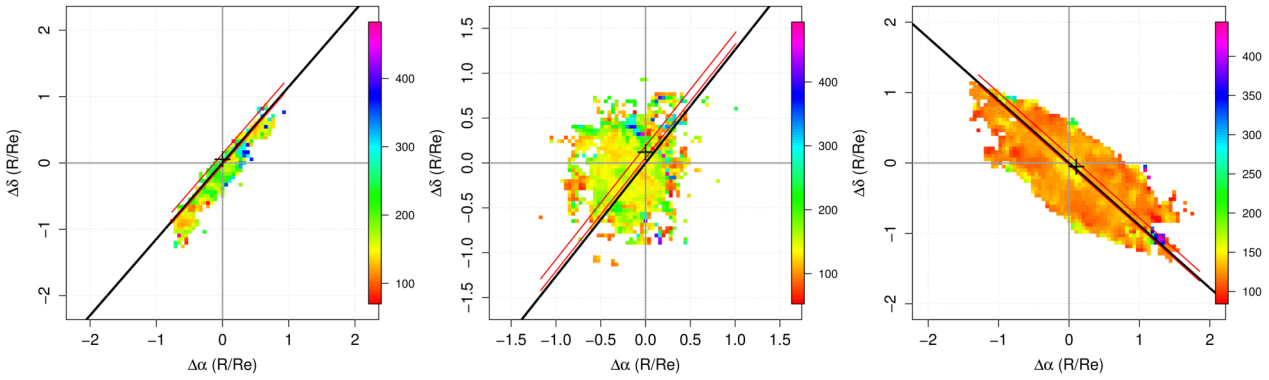

(j) NGC3160 (k) NGC3182 (l) NGC4644

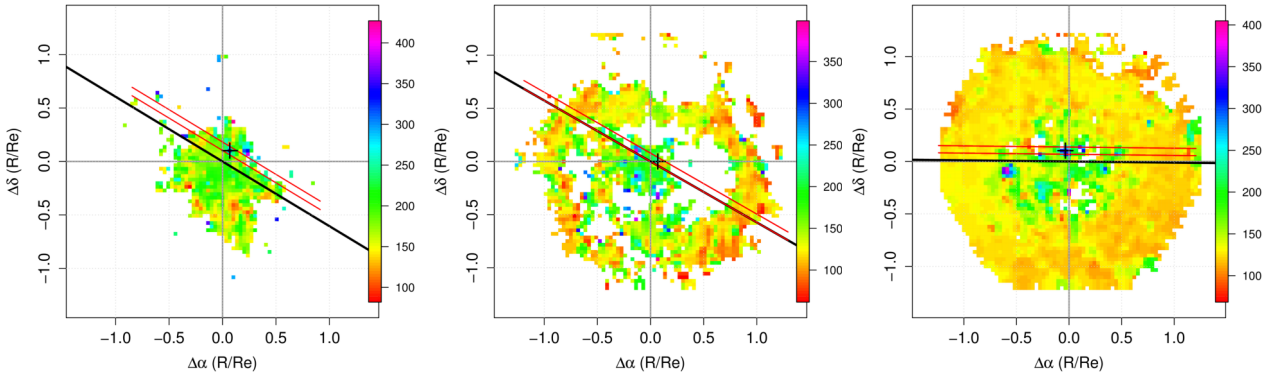

(m) NGC5216 (n) NGC5378 (o) NGC5957

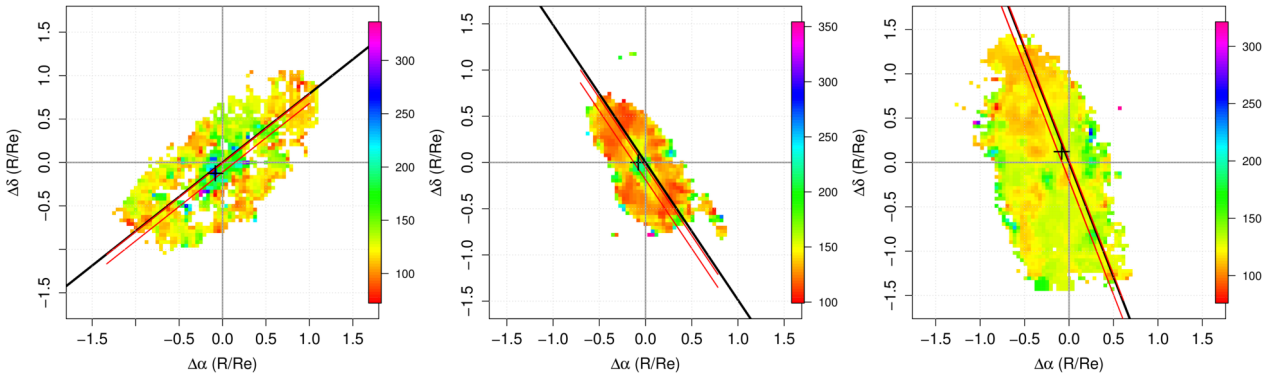

(p) NGC5971 (q) NGC6394 (r) UGC09110

Fig. A.4: Velocity dispersion maps. Continued.

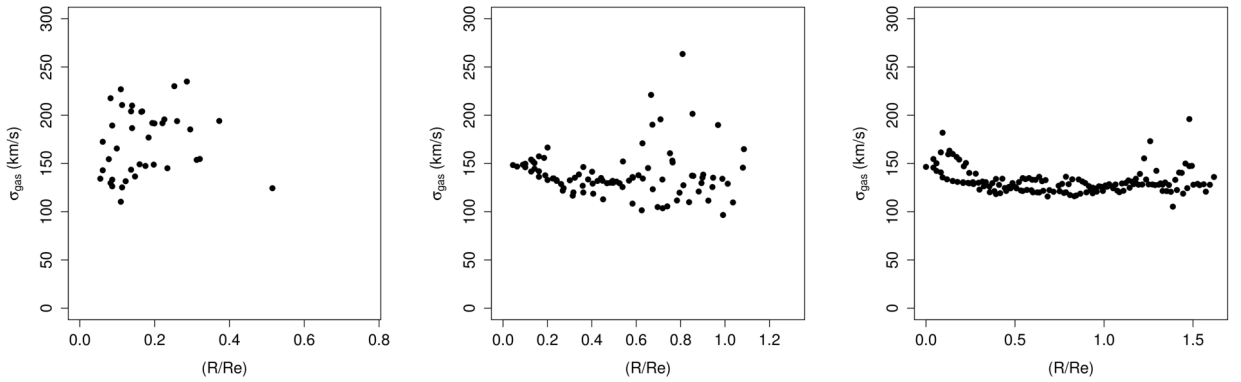

(a) IC0485 (b) IC0540 (c) IC2247

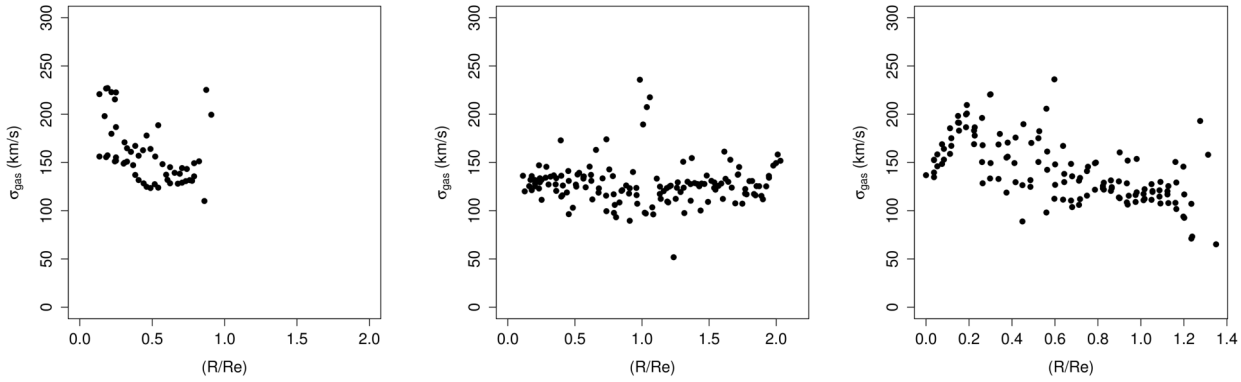

(d) IC4215 (e) MCG-02-02-030 (f) MCG-02-08-014

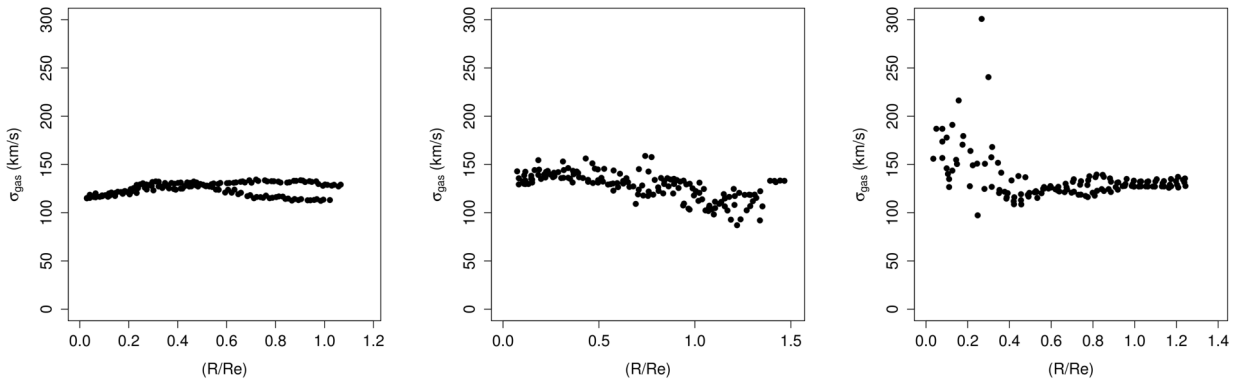

(g) NGC0681 (h) NGC2410 (i) NGC2916

Fig. A.5: Velocity dispersion Profiles with the spaxels contained between the red lines of the maps in figure A.4.

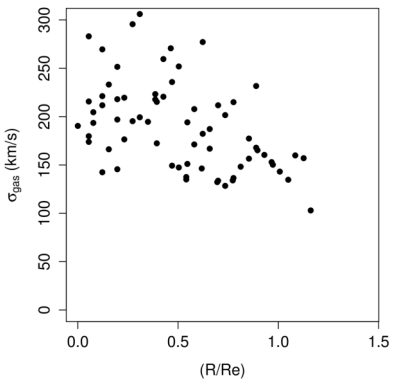

(j) NGC3160

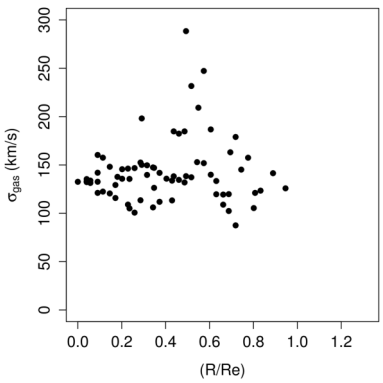

(k) NGC3182

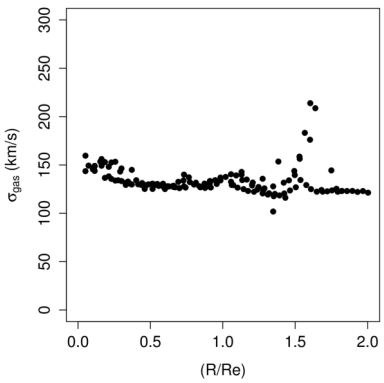

(l) NGC4644

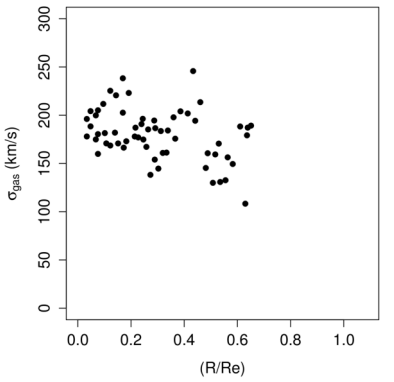

(m) NGC5216

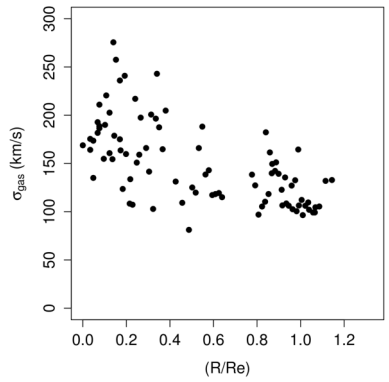

(n) NGC5378

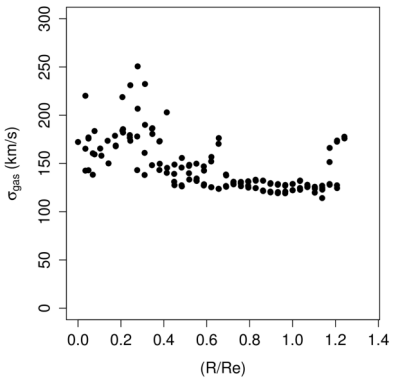

(o) NGC5957

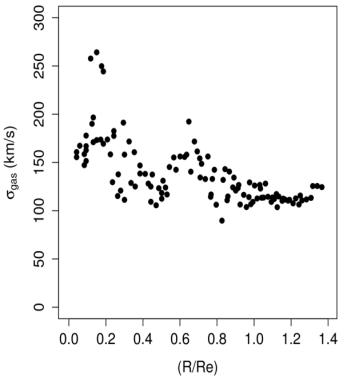

(p) NGC5971

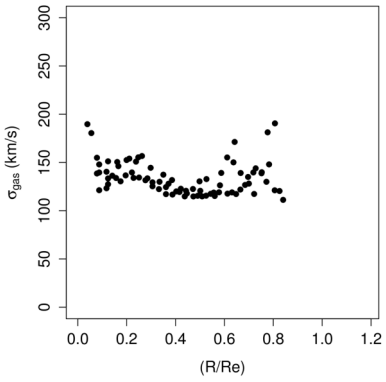

(q) NGC6394

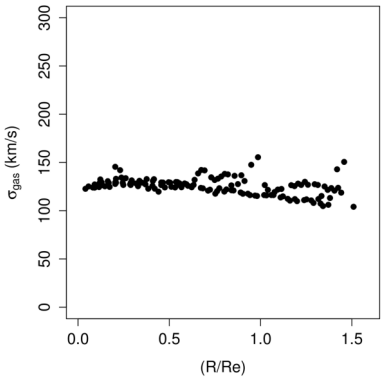

(r) UGC09110

Fig. A.5: Velocity dispersion Profiles. Continued.

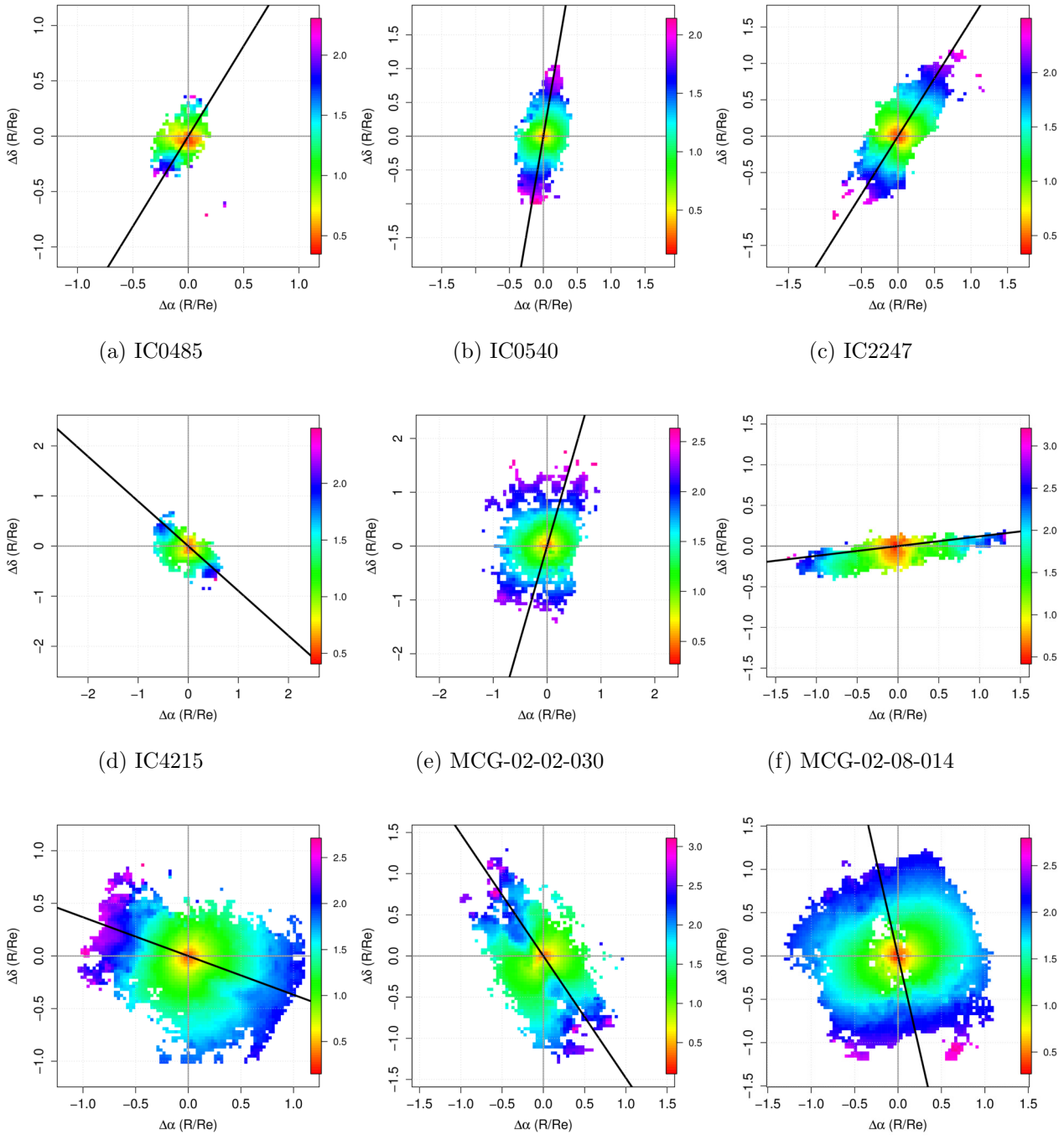

(a) IC0485 (b) IC0540 (c) IC2247

(d) IC4215 (e) MCG-02-02-030 (f) MCG-02-08-014

(g) NGC0681 (h) NGC2410 (i) NGC2916

Fig. A.6: v_{rot}/σ_{gas} maps. Spaxels with values above 1 are rotation dominated and the ones with values under 1 are pressure or turbulence dominated. As before, the CALIFA centre is at coordinates (0,0) and the black line marks the major axis and the position angle.

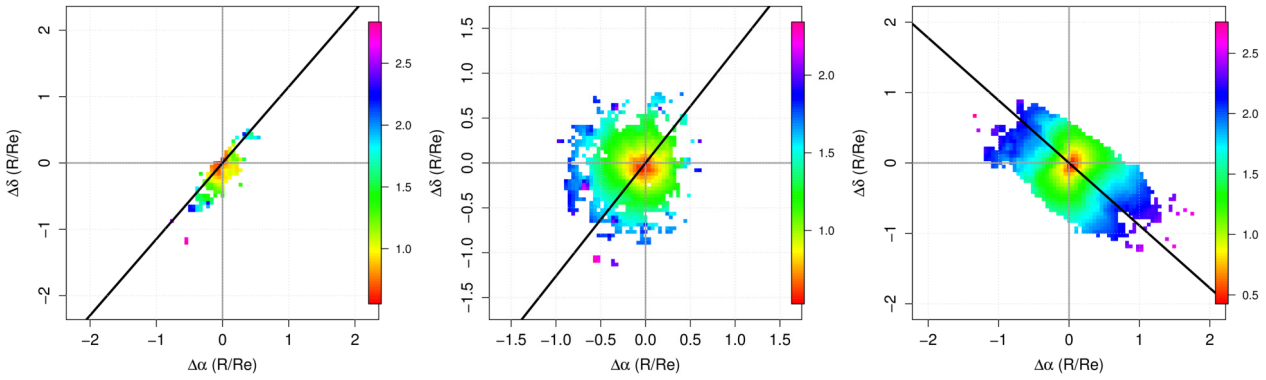

(j) NGC3160 (k) NGC3182 (l) NGC4644

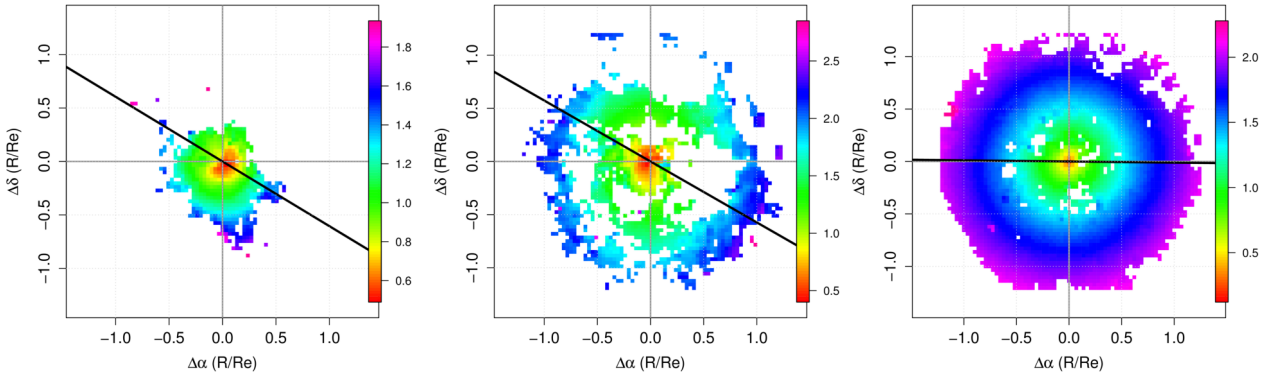

(m) NGC5216 (n) NGC5378 (o) NGC5957

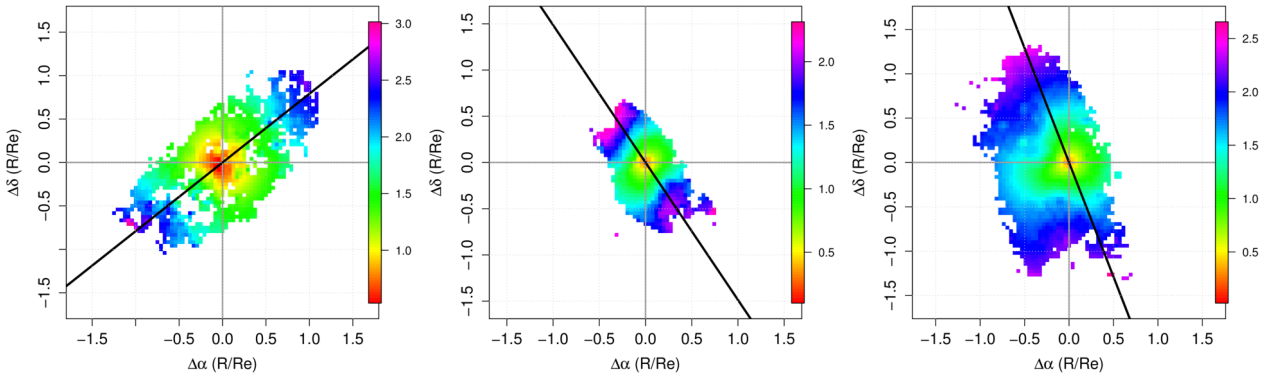

(p) NGC5971 (q) NGC6394 (r) UGC09110

Fig. A.6: v_{rot}/σ_{gas} maps. Continued.

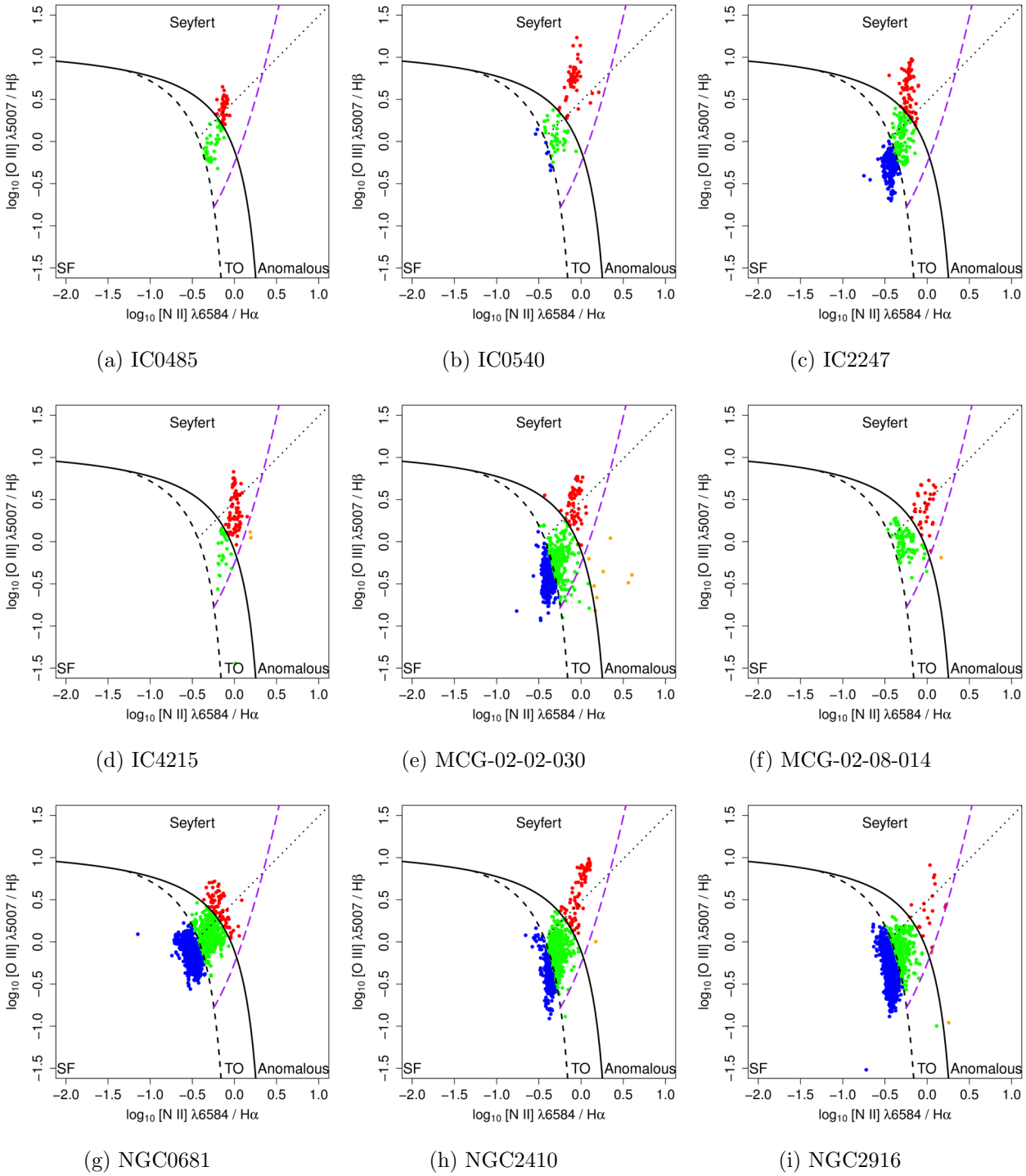

(a) IC0485 (b) IC0540 (c) IC2247

(d) IC4215 (e) MCG-02-02-030 (f) MCG-02-08-014

(g) NGC0681 (h) NGC2410 (i) NGC2916

Fig. A.7: BPT-NII diagrams. The solid-black line is the Ke01 limit, the dashed-black line is the Ka03 limit. The dashed-purpÄºe lines are our new proposed division between Seyfert and anomalous spaxels. The Ci10 line is indicated as a reference with a black dotted line.

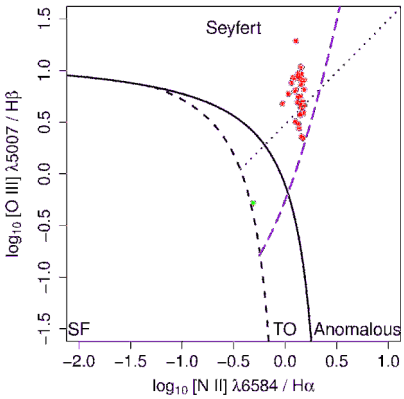

(j) NGC3160

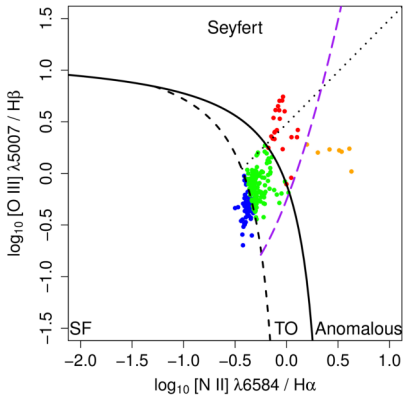

(k) NGC3182

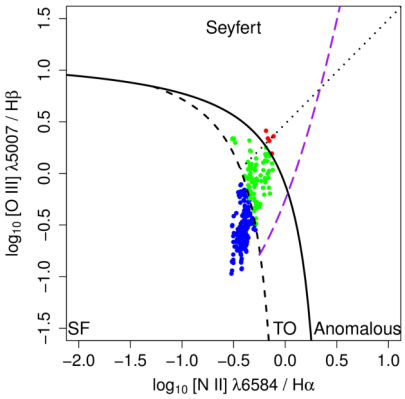

(l) NGC4644

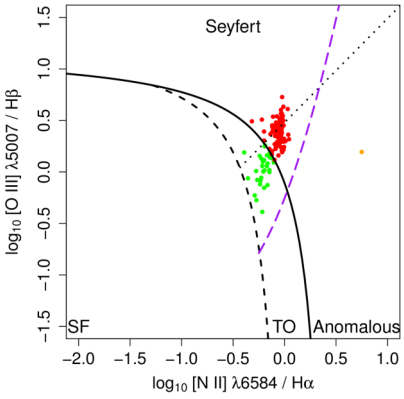

(m) NGC5216

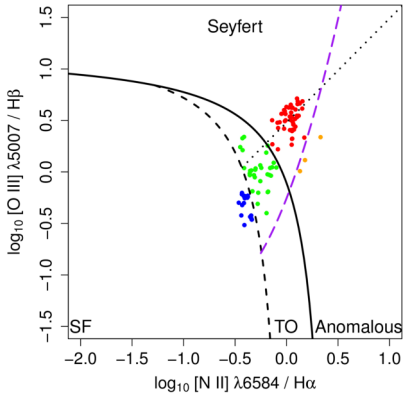

(n) NGC5378

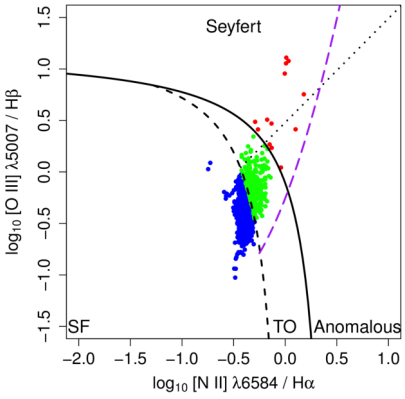

(o) NGC5957

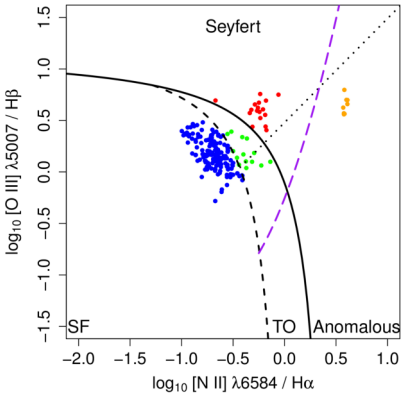

(p) NGC5971

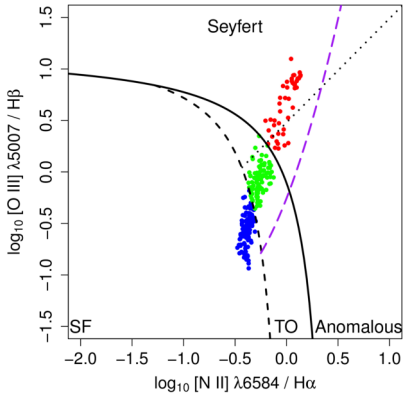

(q) NGC6394

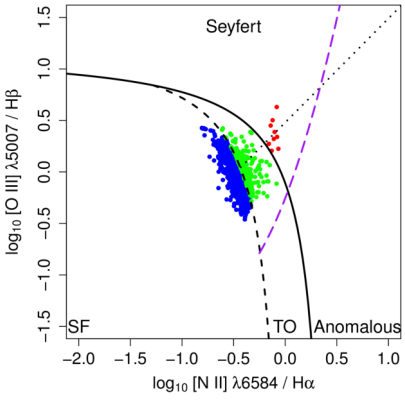

(r) UGC09110

Fig. A.7: BPT-NII diagrams. Continued.

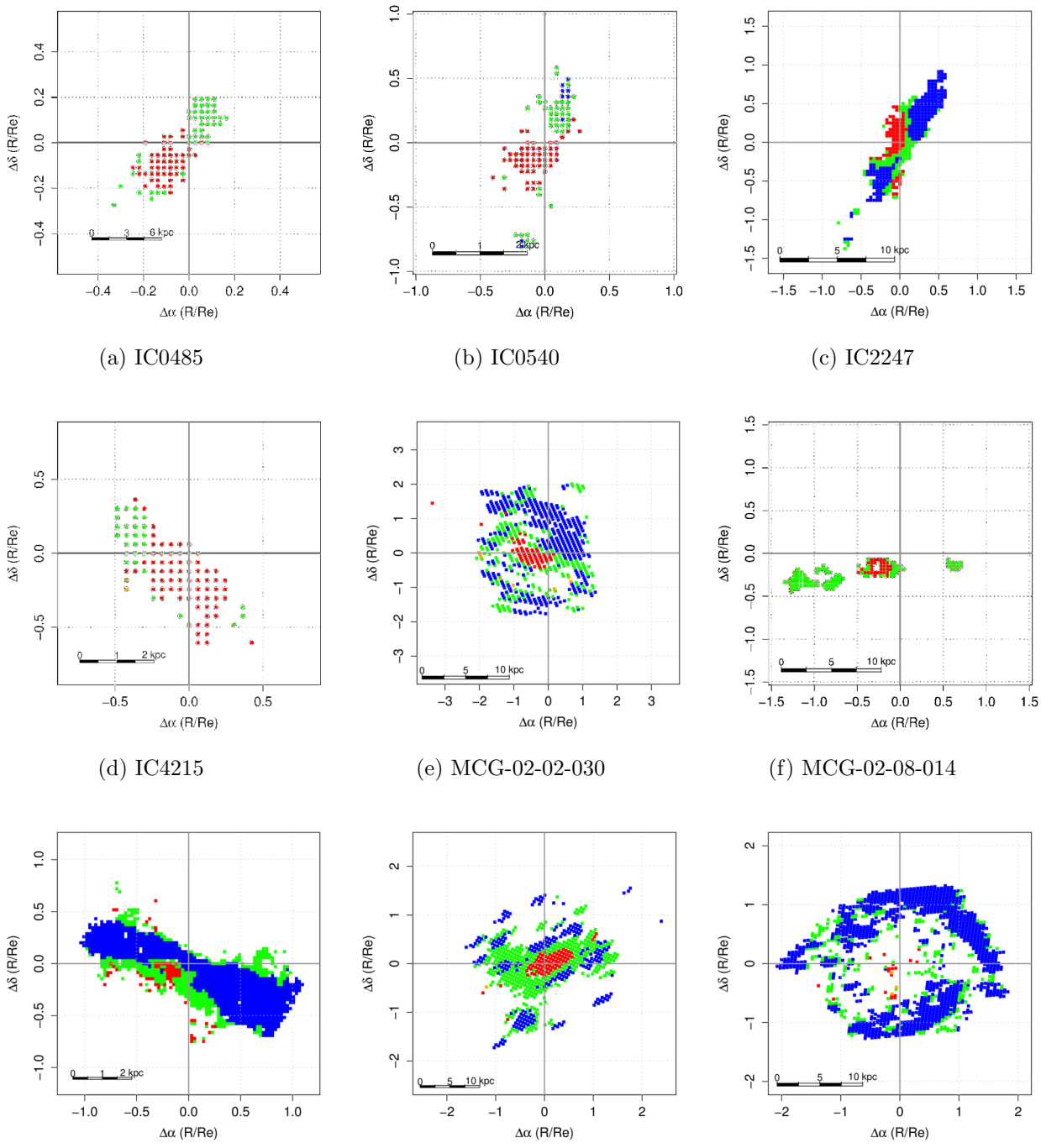

(a) IC0485 (b) IC0540 (c) IC2247

(d) IC4215 (e) MCG-02-02-030 (f) MCG-02-08-014

(g) NGC0681 (h) NGC2410 (i) NGC2916

Fig. A.8: . BPT-NII maps. The colours correspond with the ones used in figure A.7 to indicate the type of ionization source: Blue for star formation, green for transition object, red for Seyfert AGN and orange for anomalous.

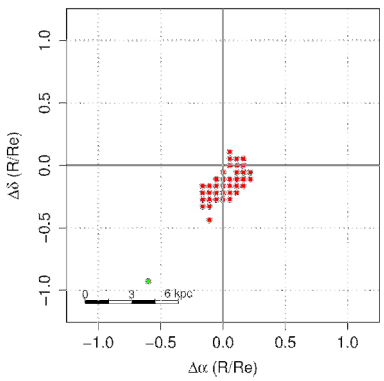

(j) NGC3160

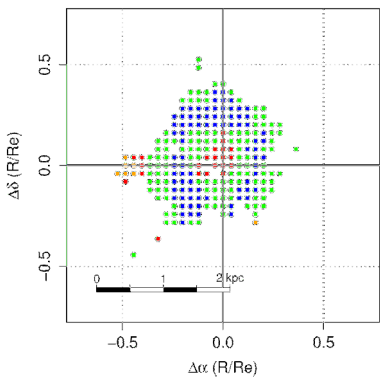

(k) NGC3182

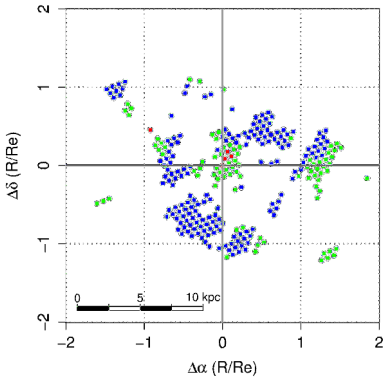

(l) NGC4644

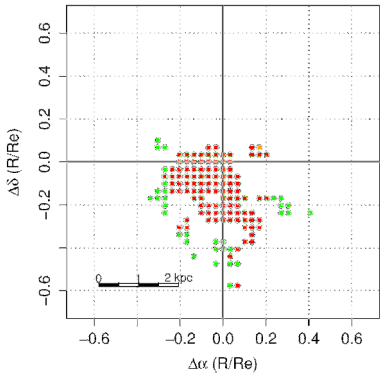

(m) NGC5216

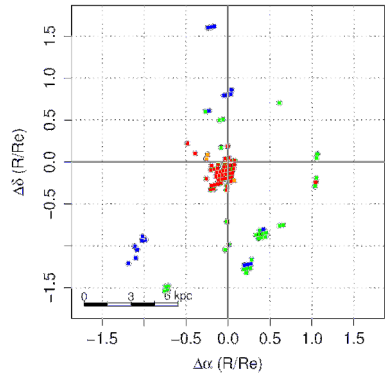

(n) NGC5378

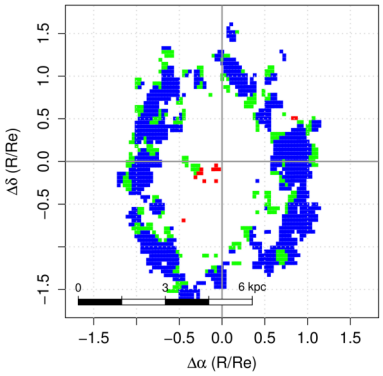

(o) NGC5957

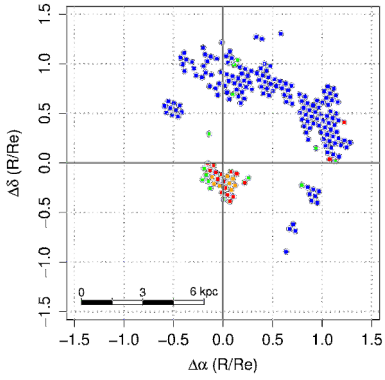

(p) NGC5971

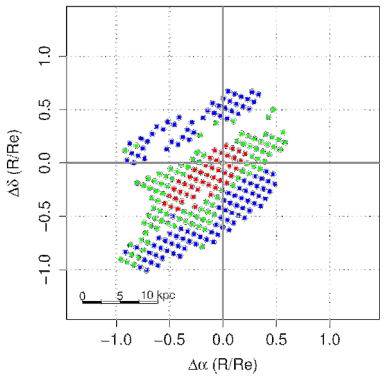

(q) NGC6394

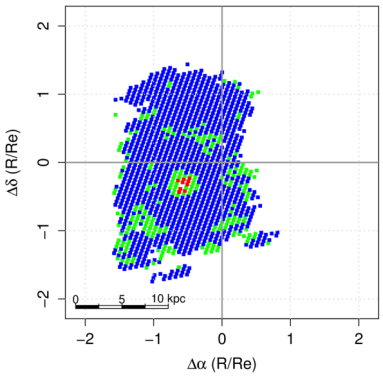

(r) UGC09110

Fig. A.8: BPT-NII maps. Continued.

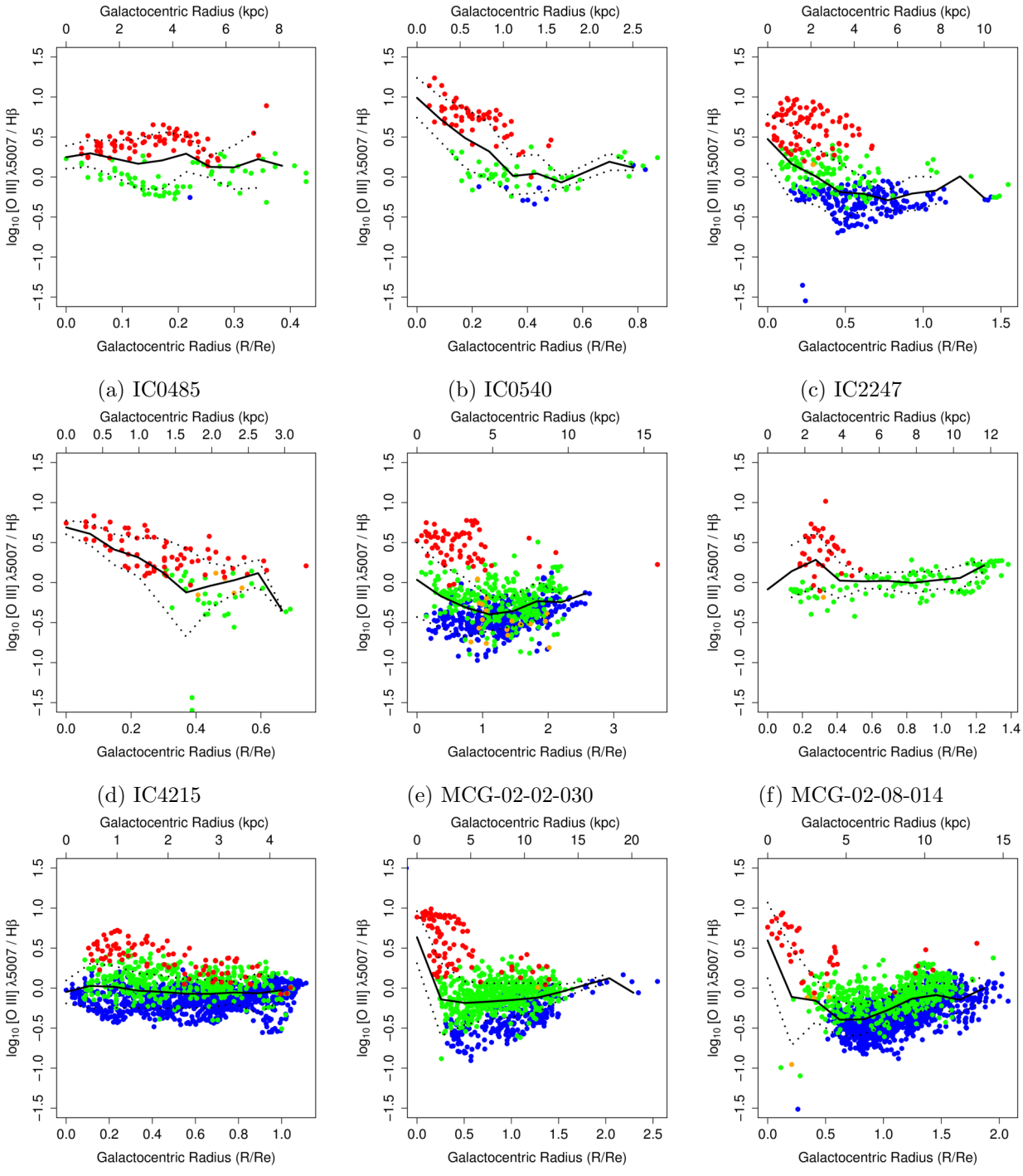

(a) IC0485 (b) IC0540 (c) IC2247

(d) IC4215 (e) MCG-02-02-030 (f) MCG-02-08-014

(g) NGC0681 (h) NGC2410 (i) NGC2916

Fig. A.9: $\log_{10}$ [O III] λ5007/Hβ radial profile. The colours correspond to those of the object types in the BPT-NII diagrams. The black line is the mean and the dotted lines are the 1σ dispersion around it.

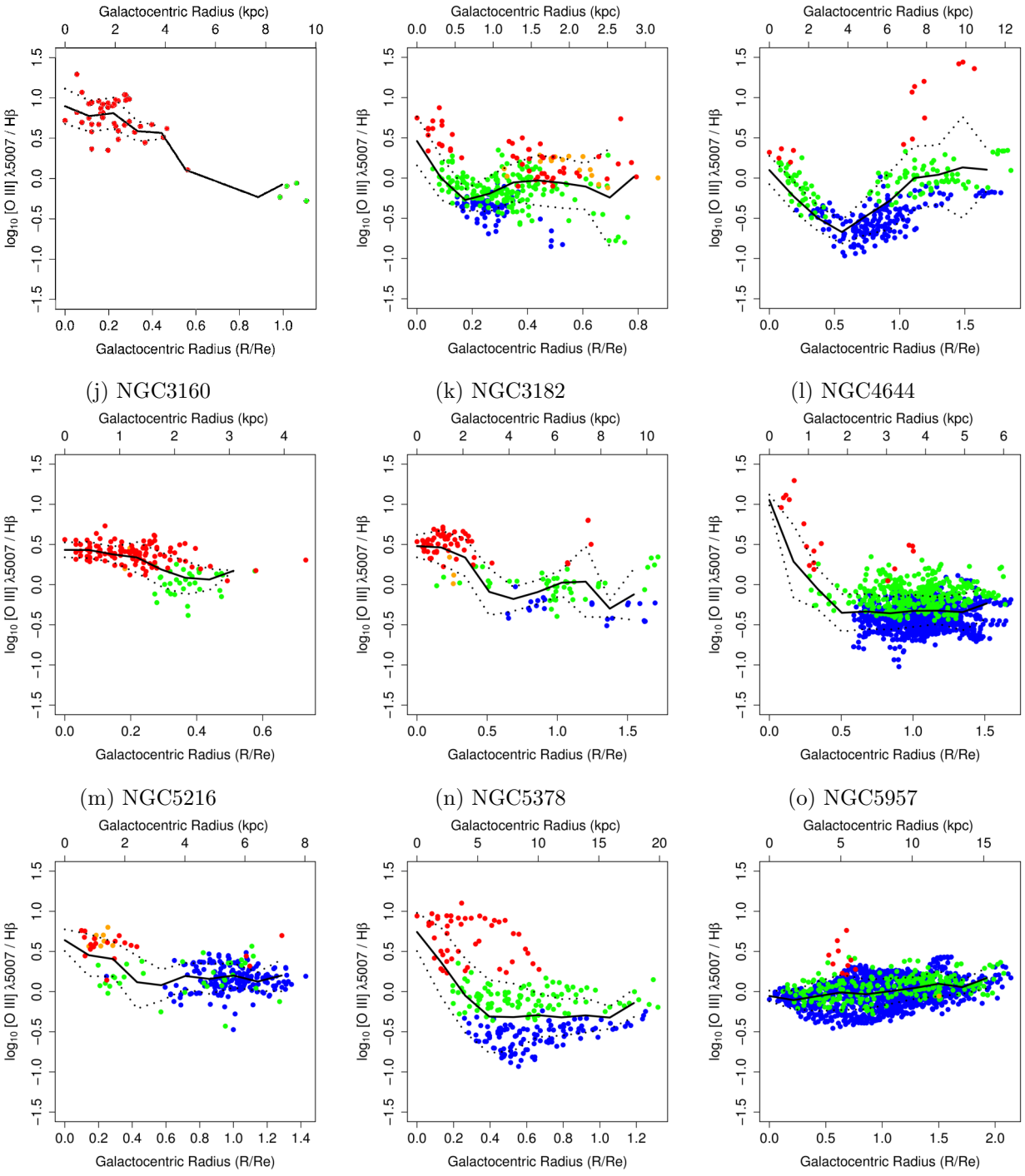

(j) NGC3160 (k) NGC3182 (l) NGC4644

(m) NGC5216 (n) NGC5378 (o) NGC5957

(p) NGC5971 (q) NGC6394 (r) UGC09110

Fig. A.9: $\log_{10}$ [O III] λ5007 / Hβ radial profile. Continued.

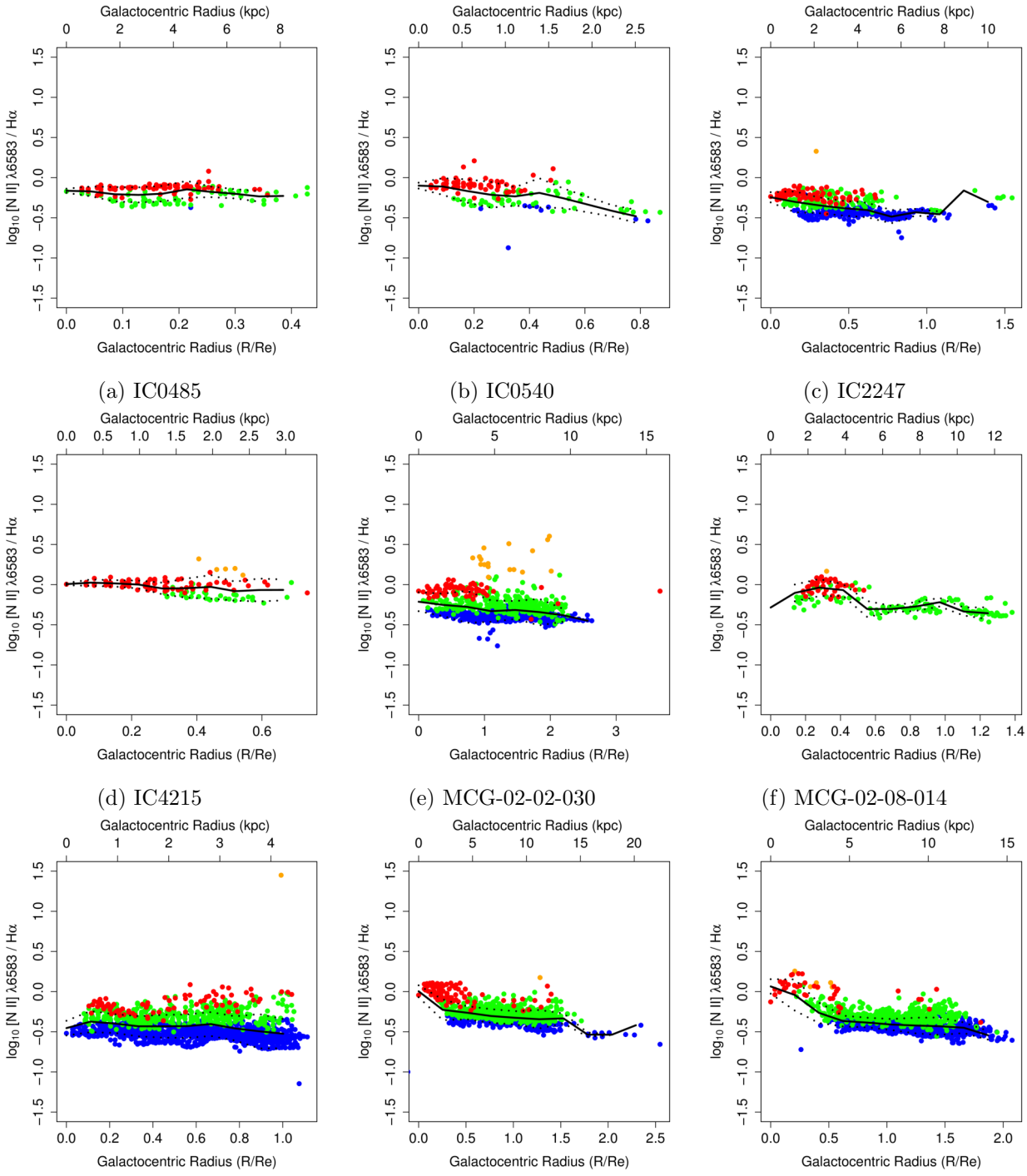

(a) IC0485 (b) IC0540 (c) IC2247

(d) IC4215 (e) MCG-02-02-030 (f) MCG-02-08-014

(g) NGC0681 (h) NGC2410 (i) NGC2916

Fig. A.10: $\log_{10}$ [N II] λ6583 / Hα radial profile. The colours correspond to those of the object types in the BPT-NII diagrams. The black line is the mean and the dotted lines are the 1σ dispersion around it.

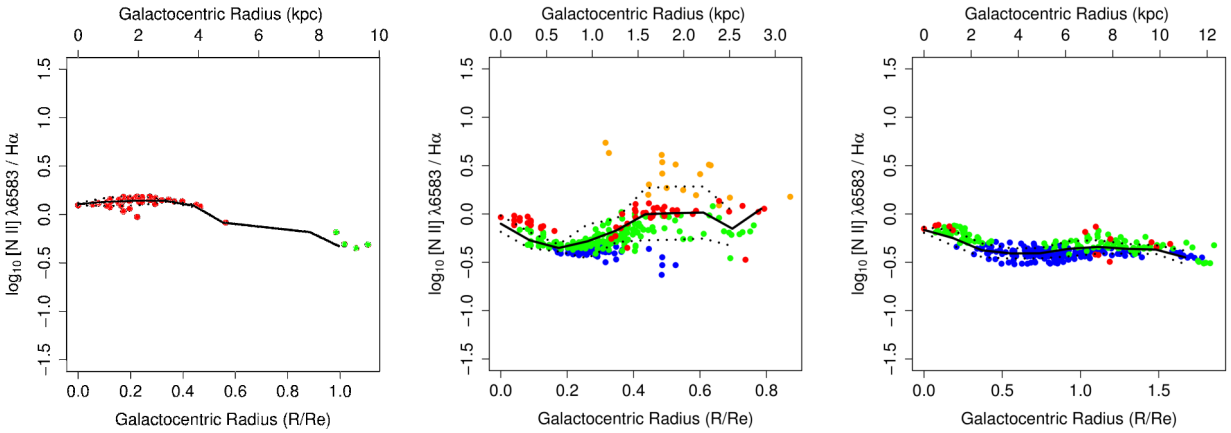

(j) NGC3160 (k) NGC3182 (l) NGC4644

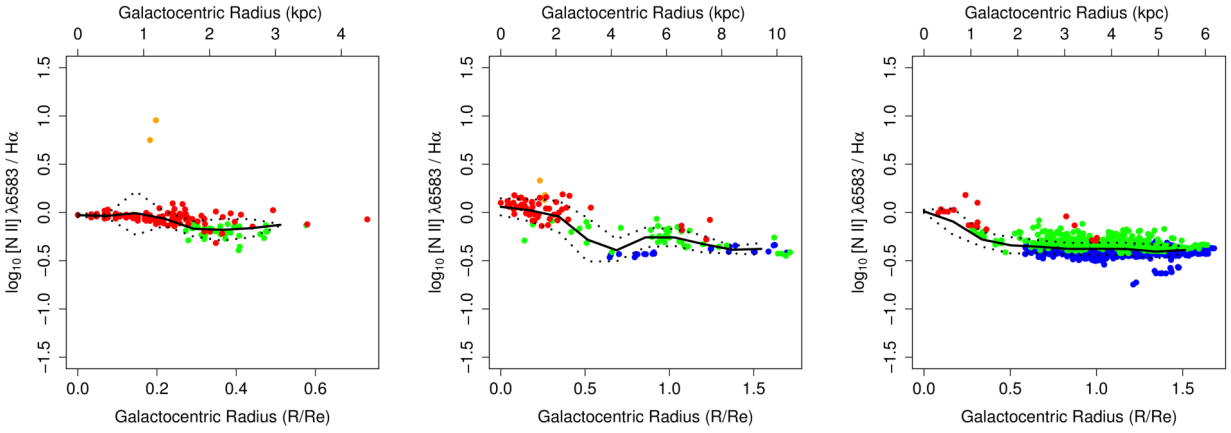

(m) NGC5216 (n) NGC5378 (o) NGC5957

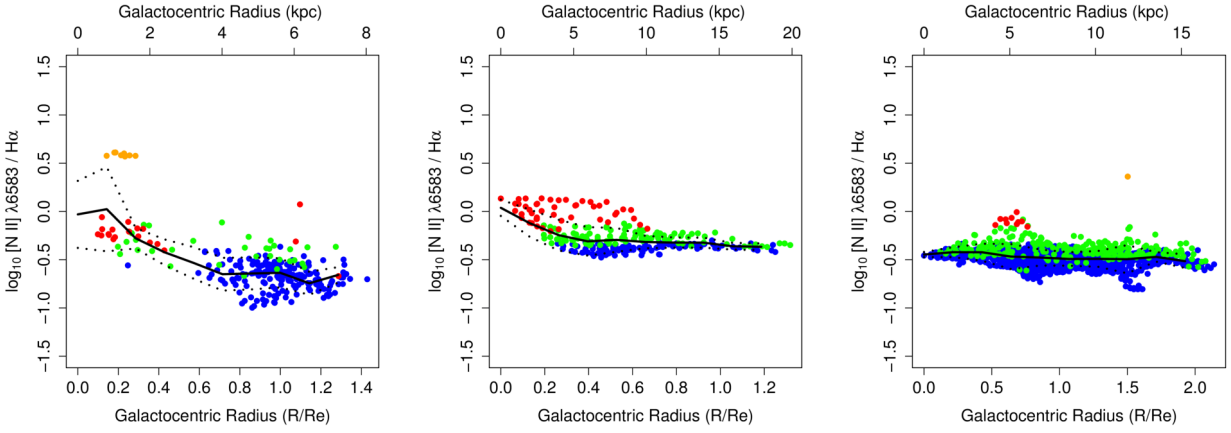

(p) NGC5971 (q) NGC6394 (r) UGC09110

Fig. A.10: $\log_{10}$ [N II] λ6583 / Hα radial profile. Continued.

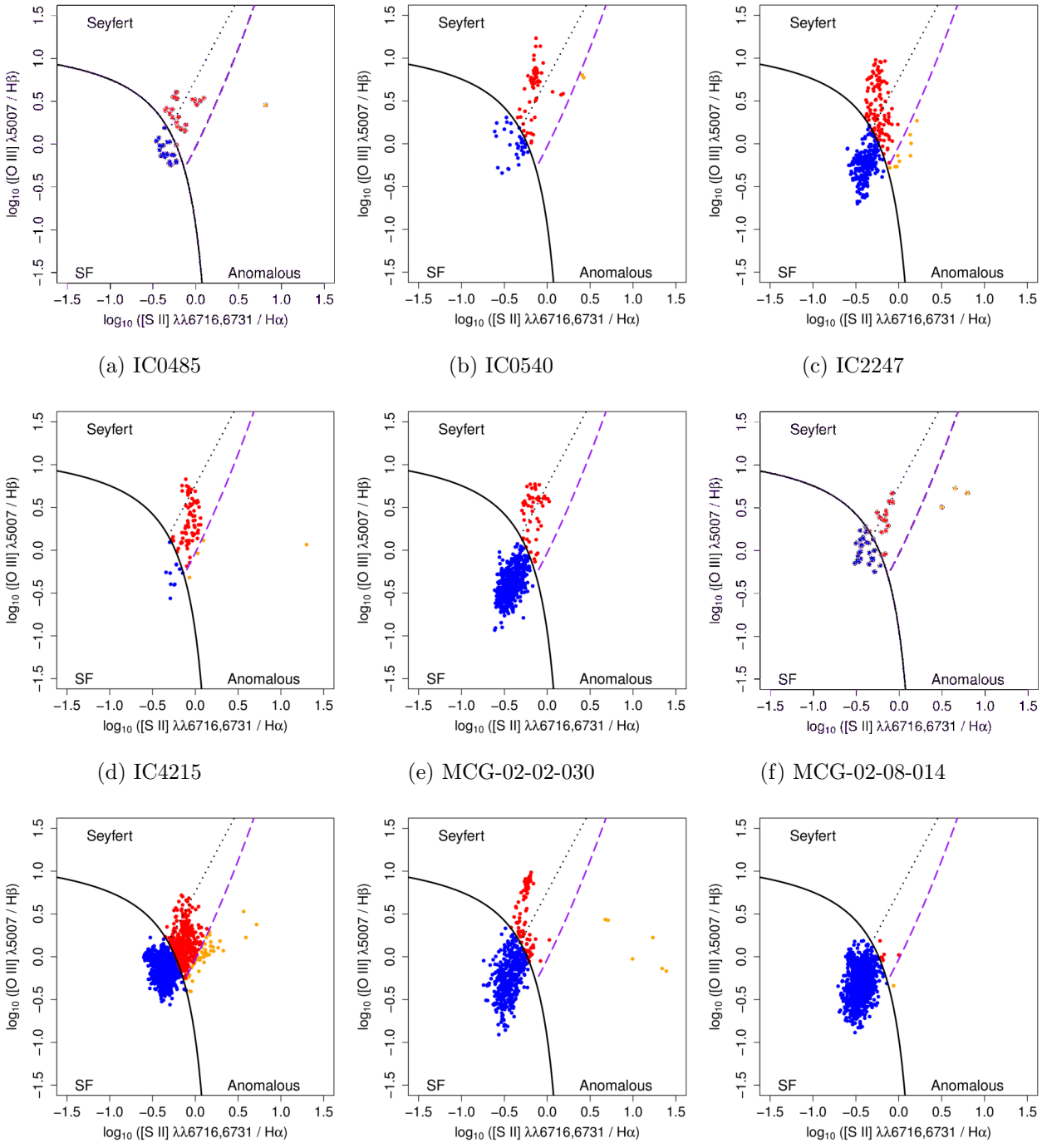

(a) IC0485 (b) IC0540 (c) IC2247

(d) IC4215 (e) MCG-02-02-030 (f) MCG-02-08-014

(g) NGC0681 (h) NGC2410 (i) NGC2916

Fig. A.11: BPT-SII diagrams for the first 9 galaxies of the sample. The purple dashed lines are our new proposed division between Seyfert and anomalous spaxels. The black solid curve and the black dotted line are the Ke01 and Ke06 limits respectively.

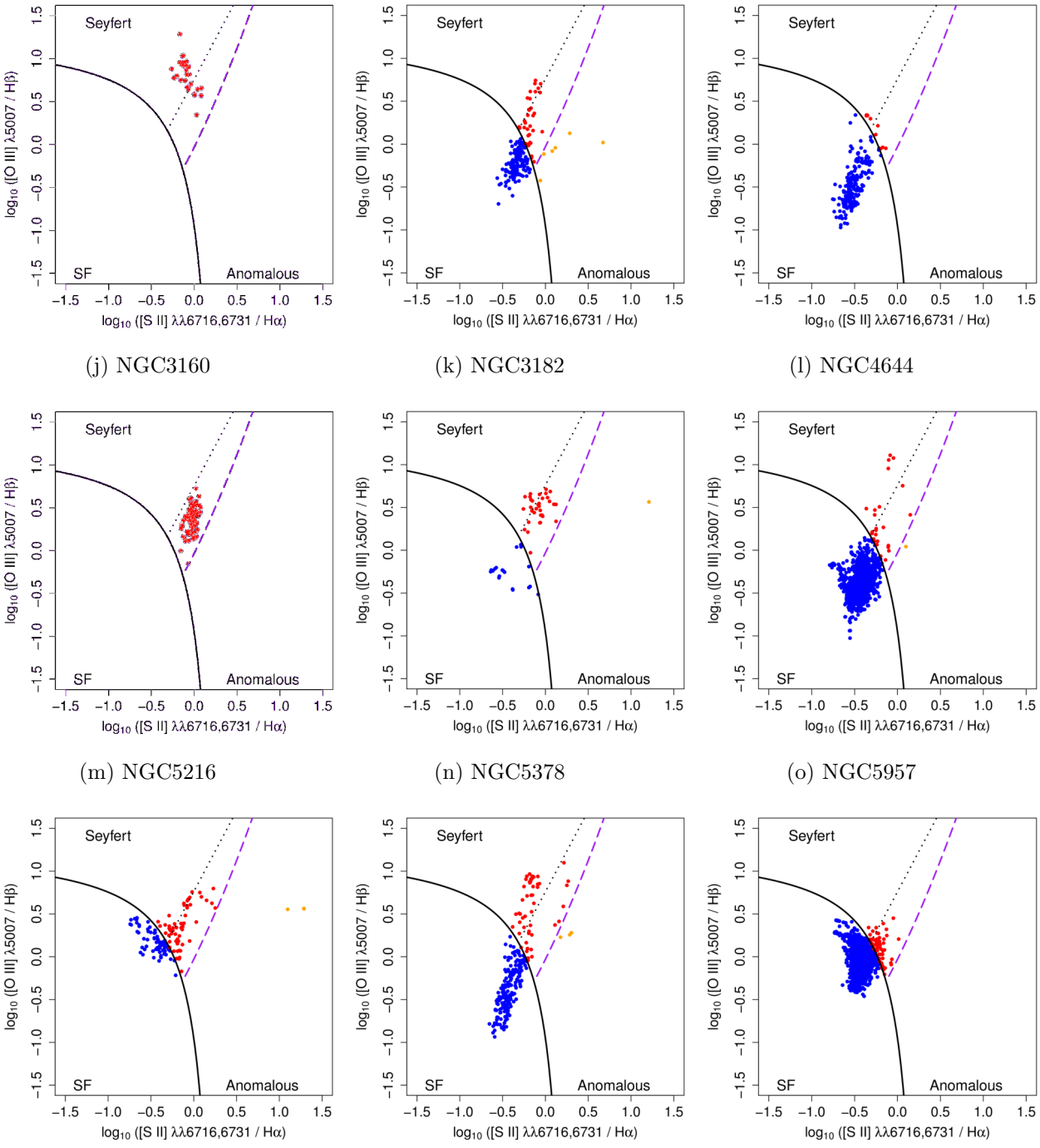

(j) NGC3160 (k) NGC3182 (l) NGC4644

(m) NGC5216 (n) NGC5378 (o) NGC5957

(p) NGC5971 (q) NGC6394 (r) UGC09110

Fig. A.11: BPT-SII diagrams. Contiued.

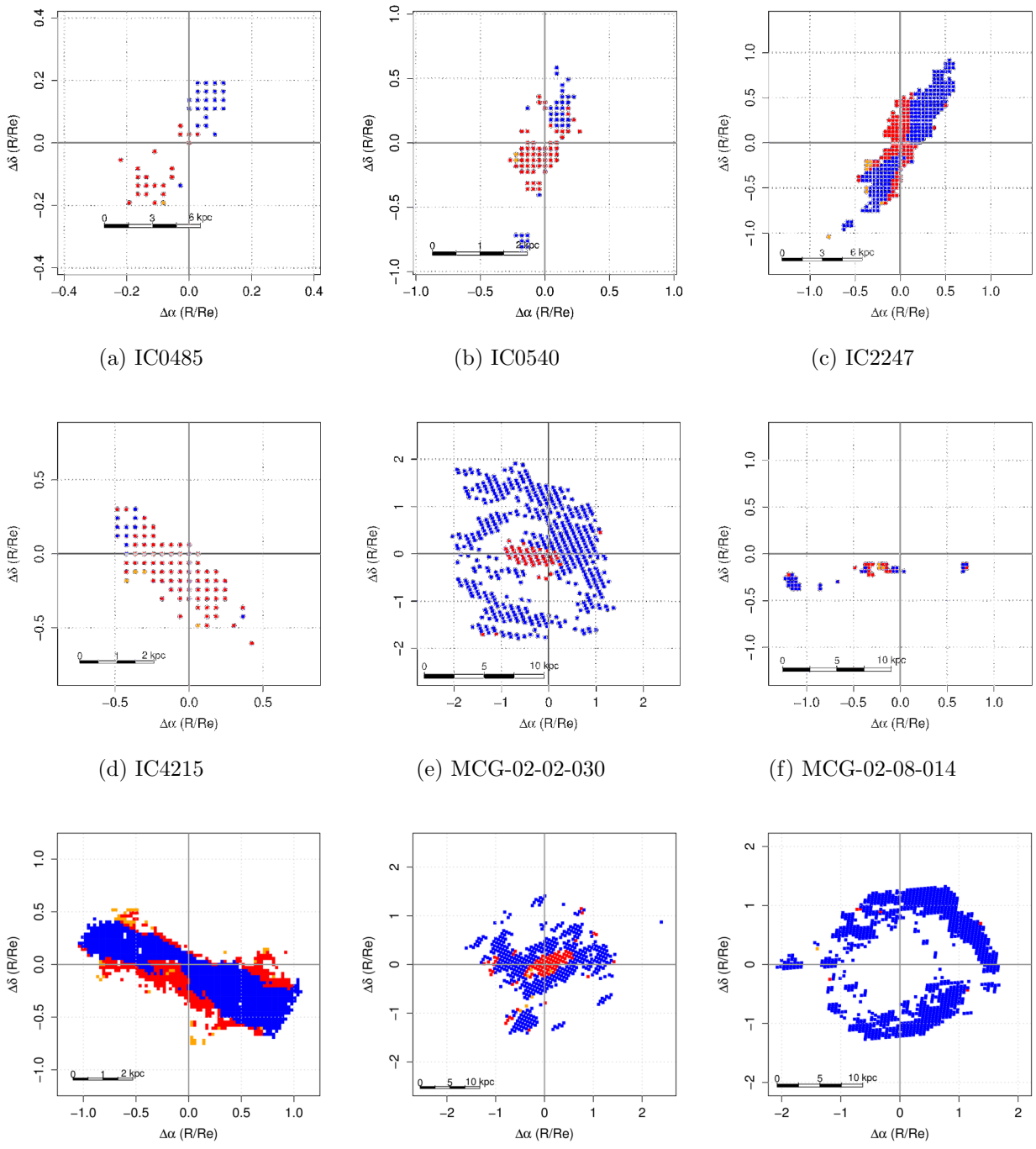

(a) IC0485 (b) IC0540 (c) IC2247

(d) IC4215 (e) MCG-02-02-030 (f) MCG-02-08-014

(g) NGC0681 (h) NGC2410 (i) NGC2916

Fig. A.12: . BPT-NII maps. The colours correspond with the ones used in figure A.11 to design the type of ionization source: Blue for star formation, red for Seyfert AGN and orange for anomalous.

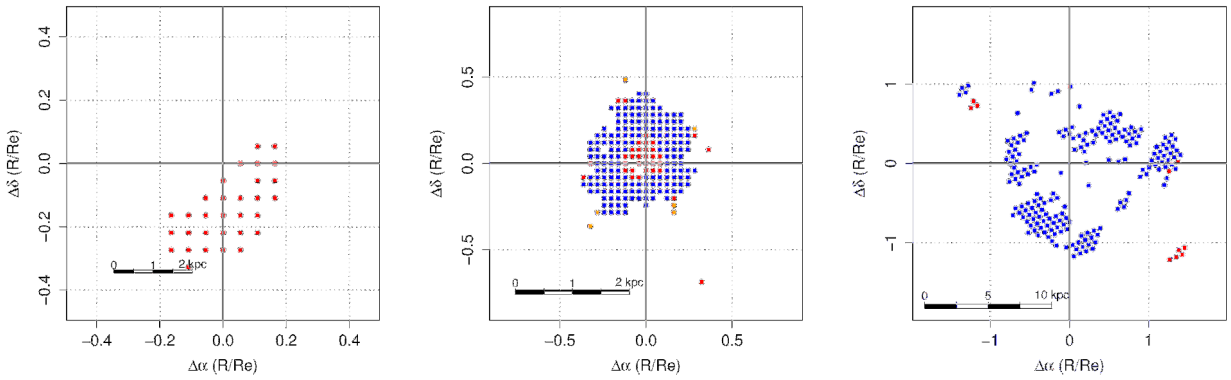

(j) NGC3160 (k) NGC3182 (l) NGC4644

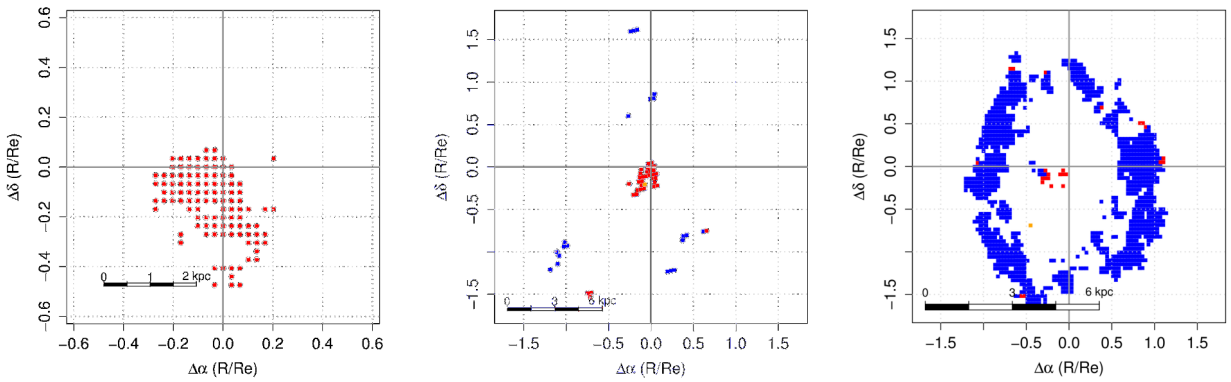

(m) NGC5216 (n) NGC5378 (o) NGC5957

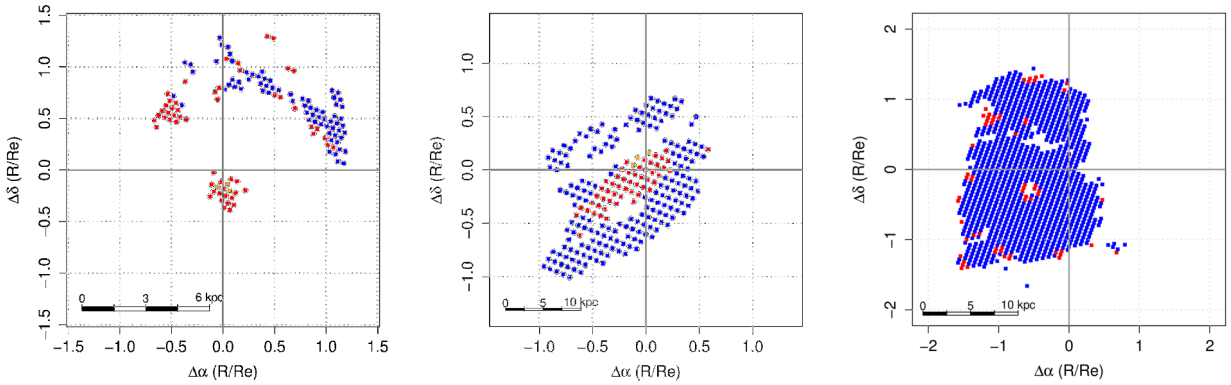

(p) NGC5971 (q) NGC6394 (r) UGC09110

Fig. A.12: BPT-SII maps. Continued.

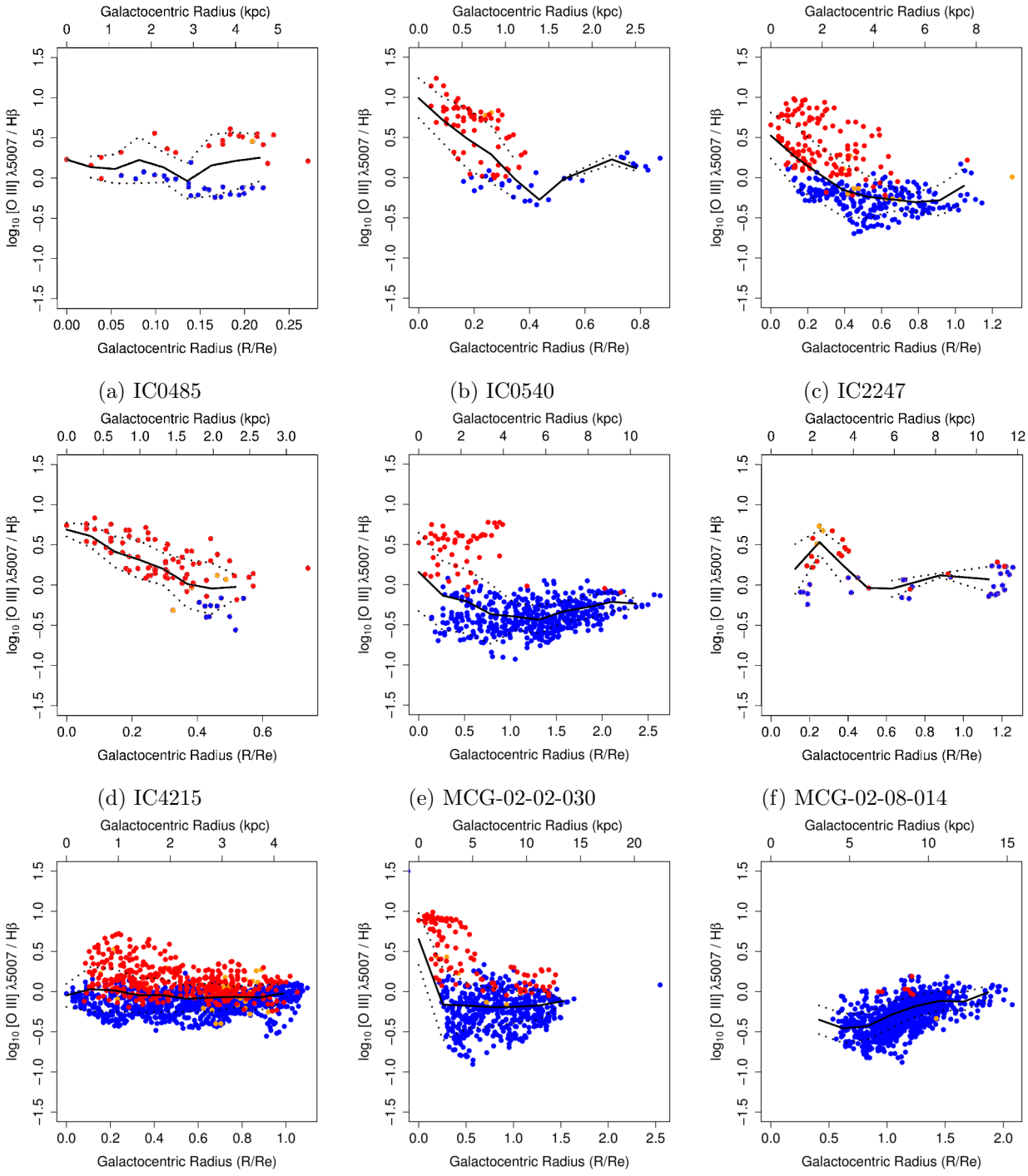

(a) IC0485 (b) IC0540 (c) IC2247

(d) IC4215 (e) MCG-02-02-030 (f) MCG-02-08-014

(g) NGC0681 (h) NGC2410 (i) NGC2916

Fig. A.13: $\log_{10}$ [O III] λ5007 / Hβ radial profile.The colours correspond to those of the object types in the BPT-SII diagrams (figure A.11). The black line is the mean and the dotted lines are the 1σ dispersion around it.

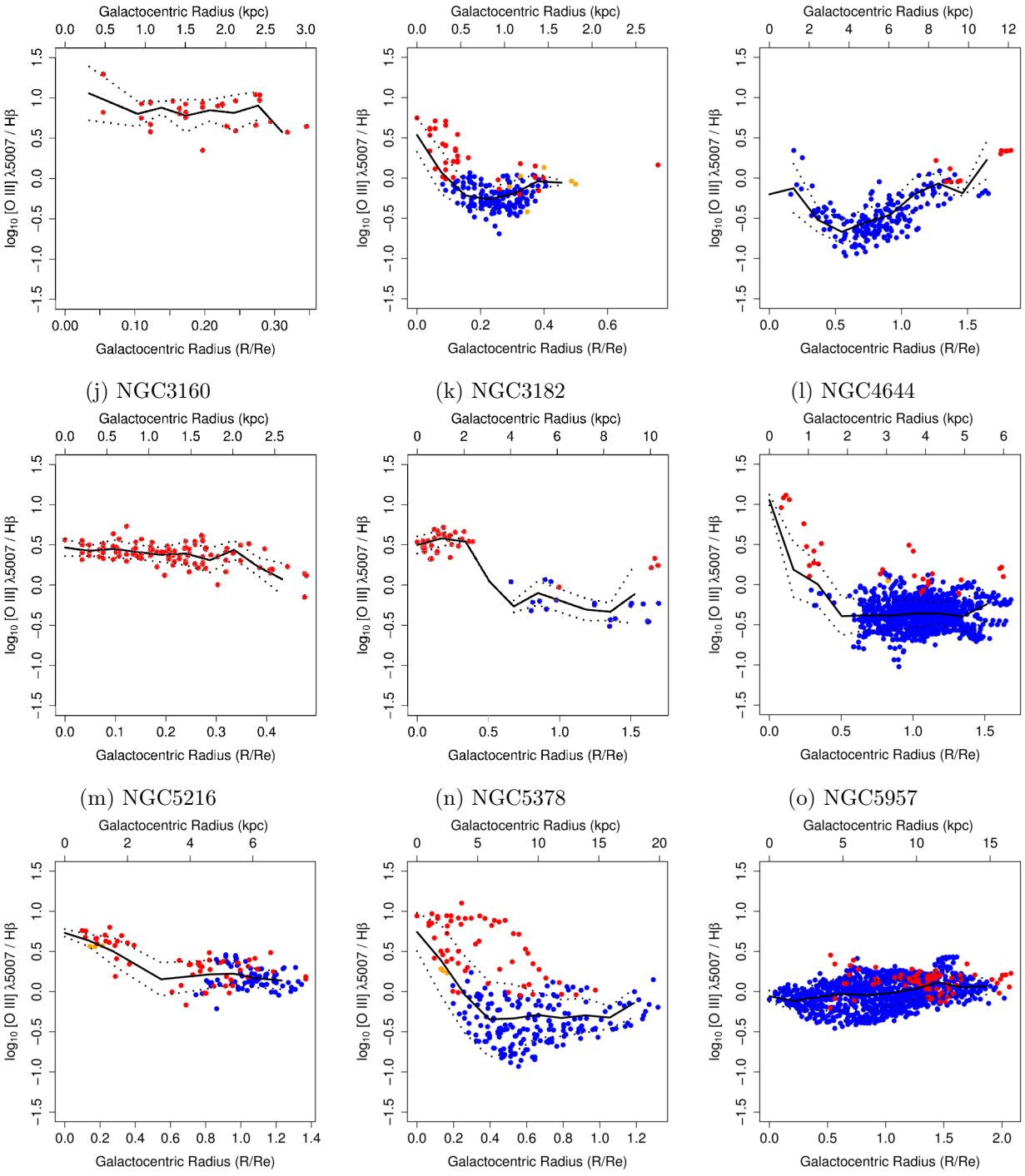

(j) NGC3160 (k) NGC3182 (l) NGC4644

(m) NGC5216 (n) NGC5378 (o) NGC5957

(p) NGC5971 (q) NGC6394 (r) UGC09110

Fig. A.13: $\log_{10}$ [O III] λ5007 / Hβ radial profile. Continued.

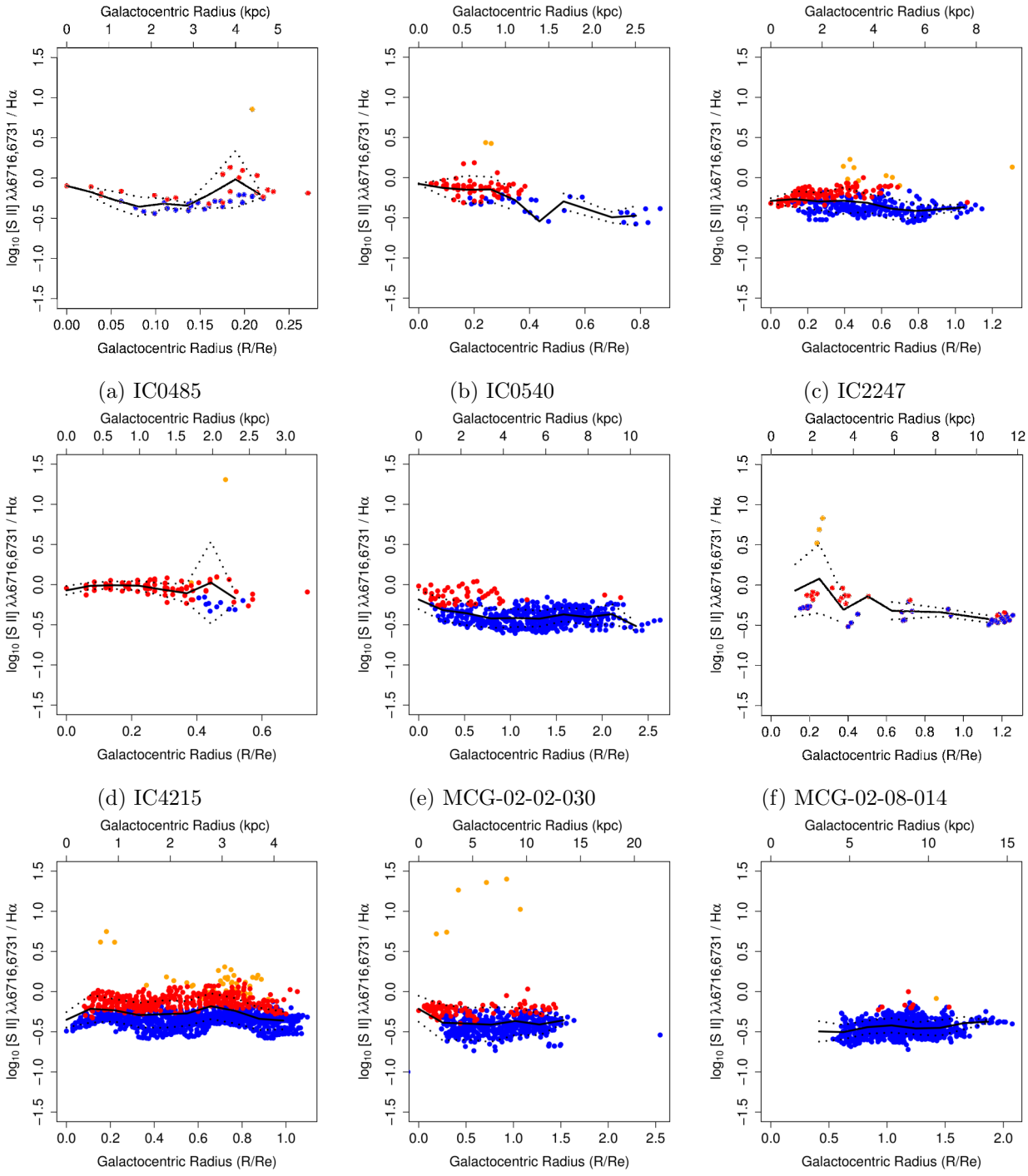

(a) IC0485 (b) IC0540 (c) IC2247

(d) IC4215 (e) MCG-02-02-030 (f) MCG-02-08-014

(g) NGC0681 (h) NGC2410 (i) NGC2916

Fig. A.14: $\log_{10}$ [S II] $\lambda\lambda 6716, 6731$ / Hα radial profile.The colours correspond to those of the object types in the BPT-NII diagrams. The black line is the mean and the dotted lines are the 1σ dispersion around it.

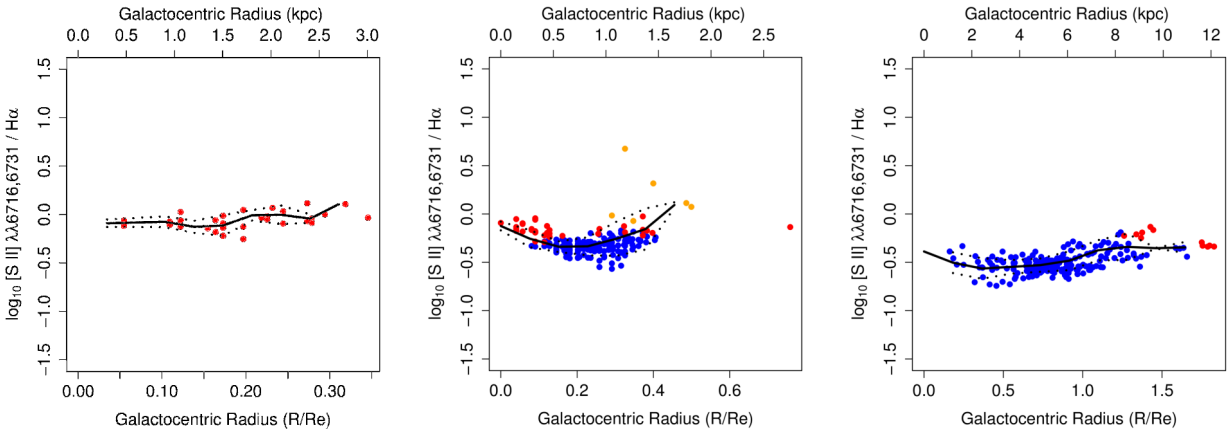

(j) NGC3160 (k) NGC3182 (l) NGC4644

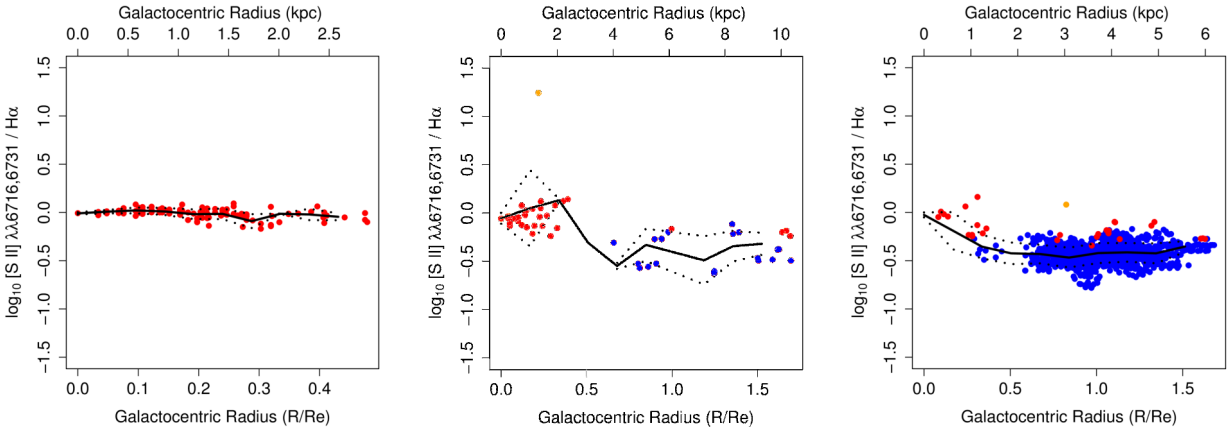

(m) NGC5216 (n) NGC5378 (o) NGC5957

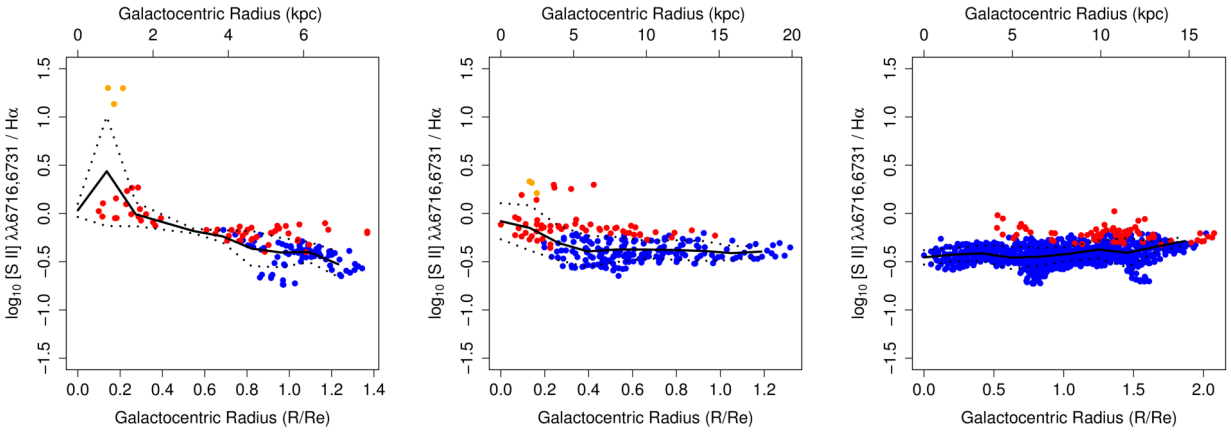

(p) NGC5971 (q) NGC6394 (r) UGC09110

Fig. A.14: $\log_{10}$ [S II] $\lambda\lambda 6716, 6731/$ Hα radial profile. Continued.

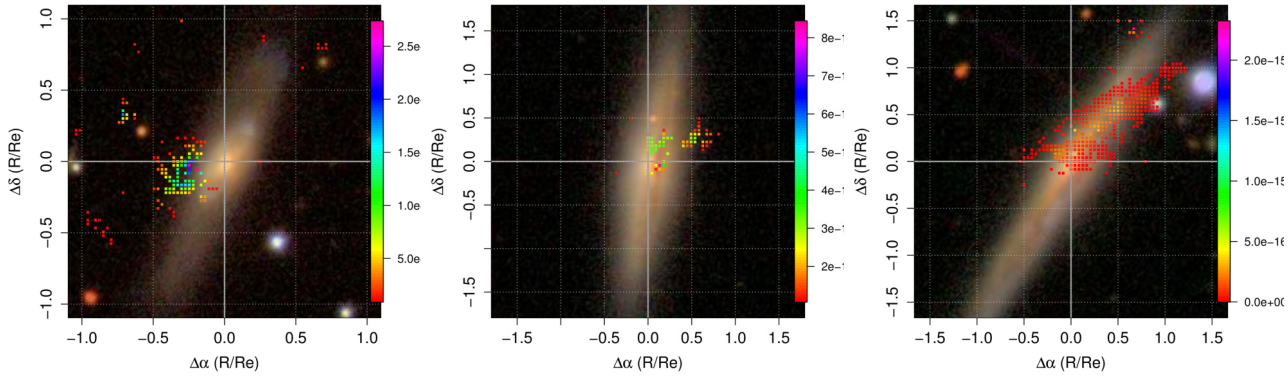

(a) IC0485 (b) IC0540 (c) IC2247

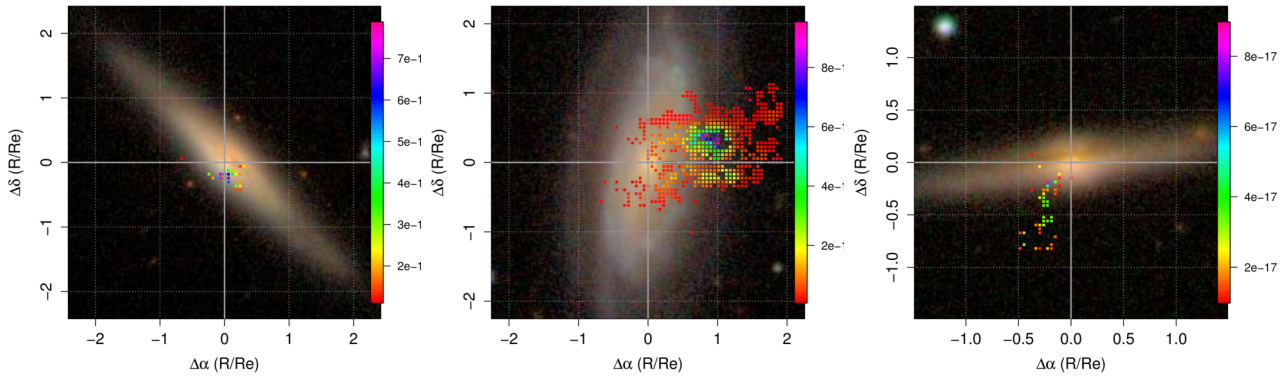

(d) IC4215 (e) MCG-02-02-030 (f) MCG-02-08-014

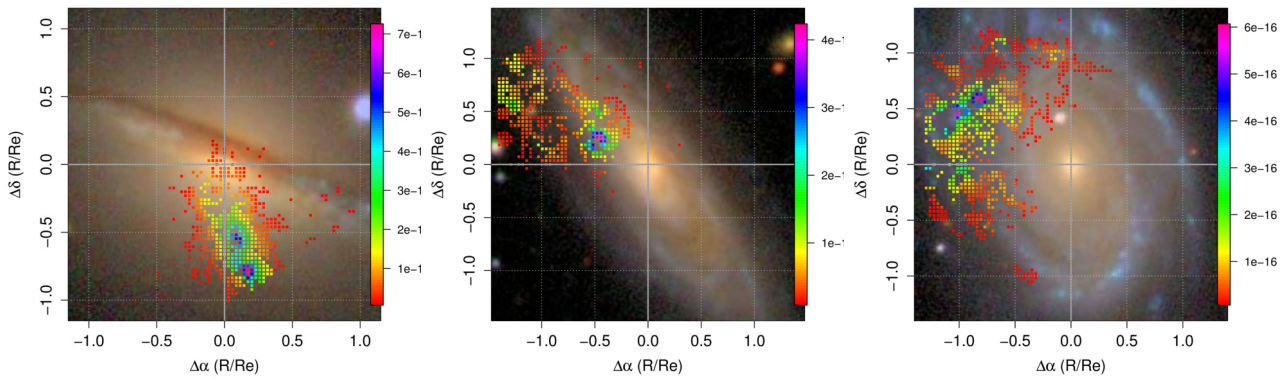

(g) NGC0681 (h) NGC2410 (i) NGC2916

Fig. A.15: Maps of the surface specific flux of the blue shifted component of Hα. The colour code is in units of [erg s^{-1} cm^{-2} Å^{-1} arcsec^{-2}].

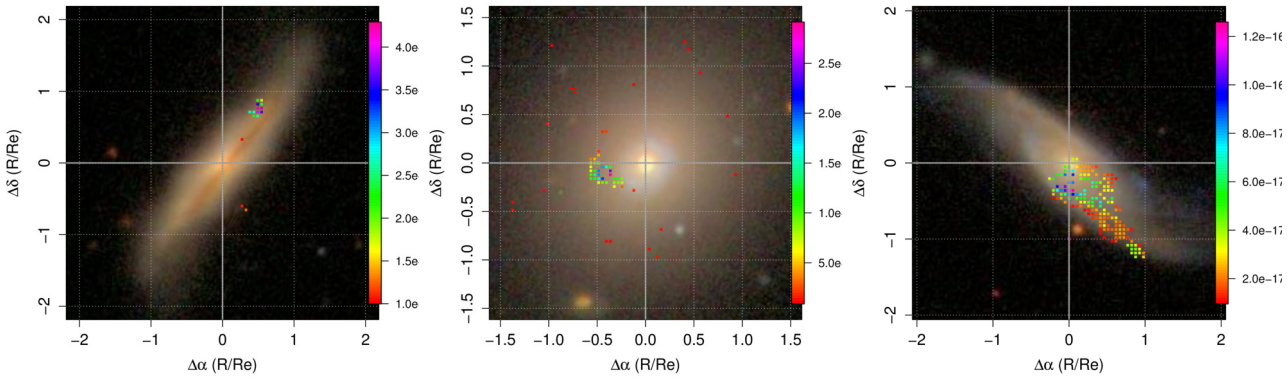

(j) NGC3160 (k) NGC3182 (l) NGC4644

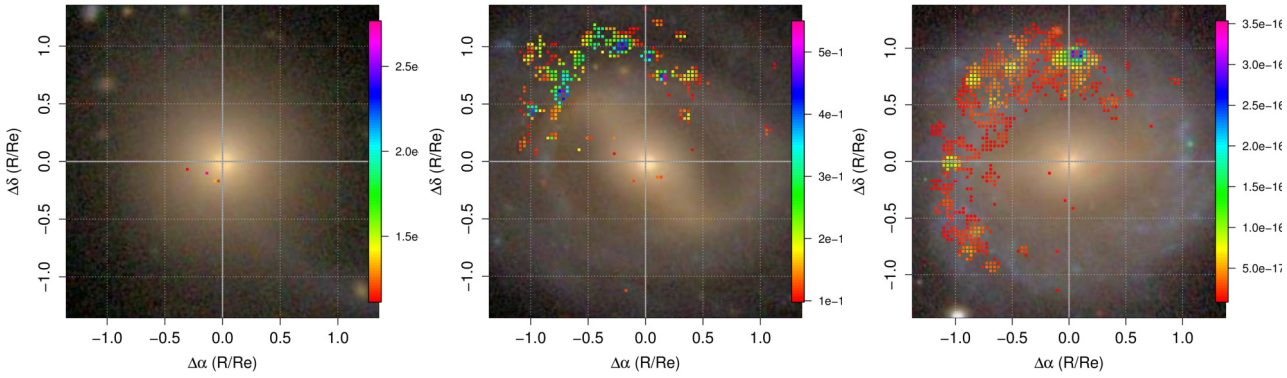

(m) NGC5216 (n) NGC5378 (o) NGC5957

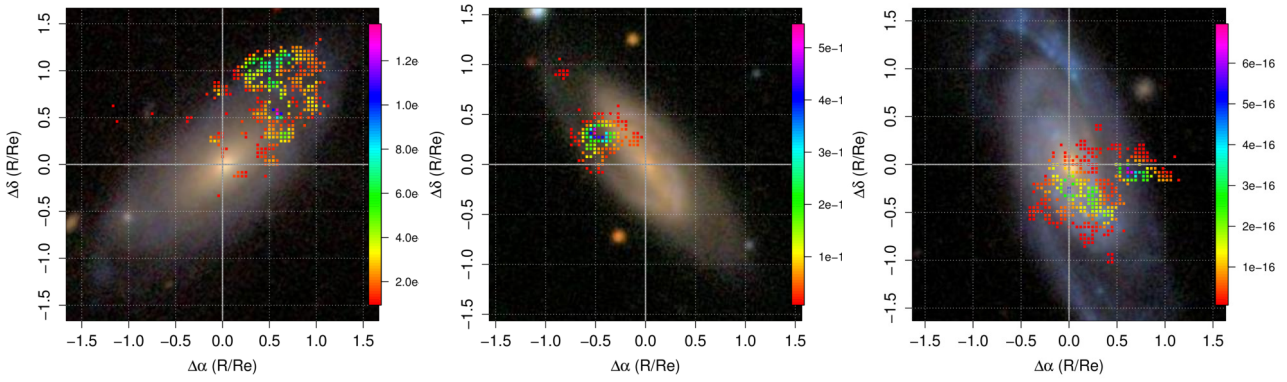

(p) NGC5971 (q) NGC6394 (r) UGC09110

Fig. A.15: Maps of the surface specific flux of the blue shifted component of Hα. Continued.

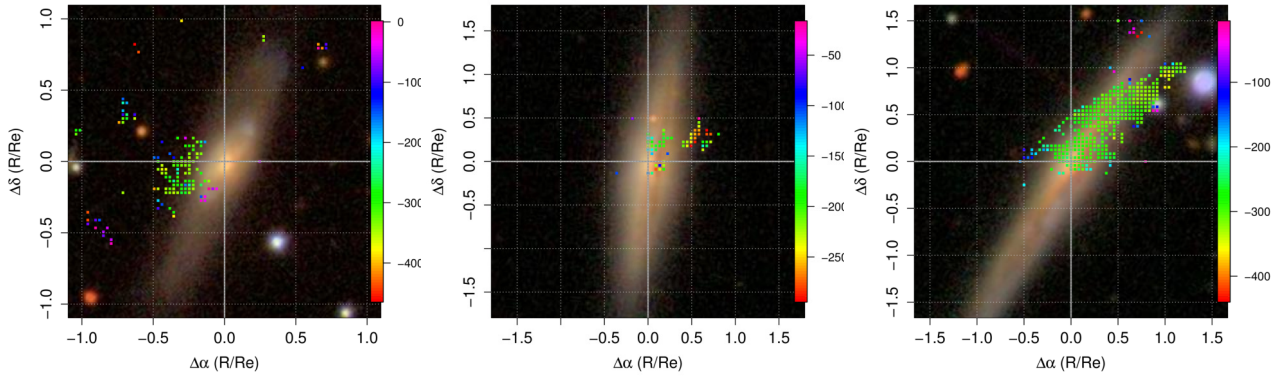

(a) IC0485 (b) IC0540 (c) IC2247

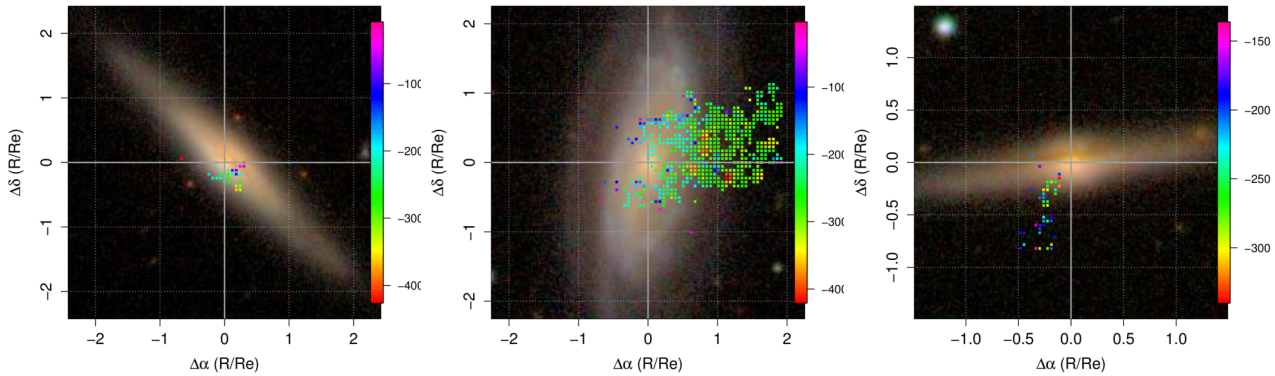

(d) IC4215 (e) MCG-02-02-030 (f) MCG-02-08-014

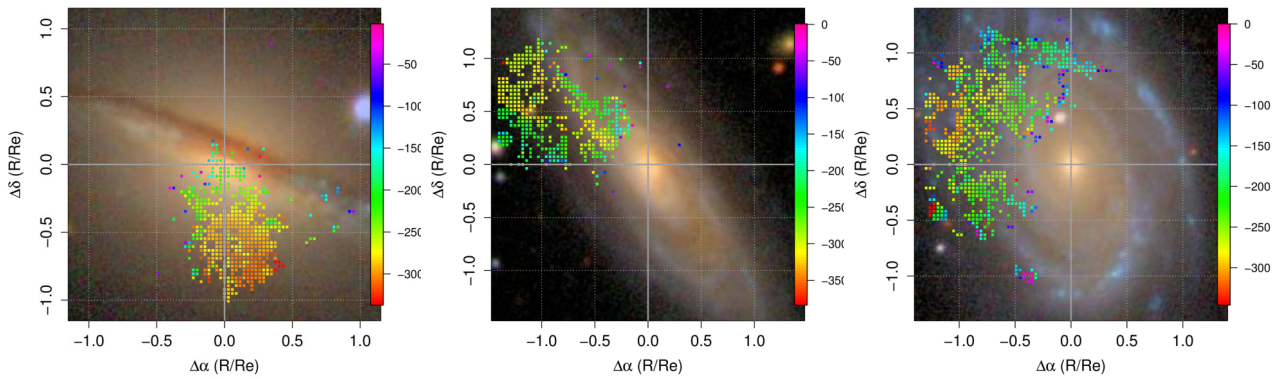

(g) NGC0681 (h) NGC2410 (i) NGC2916

Fig. A.16: Maps of the velocity in the line-of-sight of the blue shifted component of Hα. The colour code is in units of km s^{-1}.

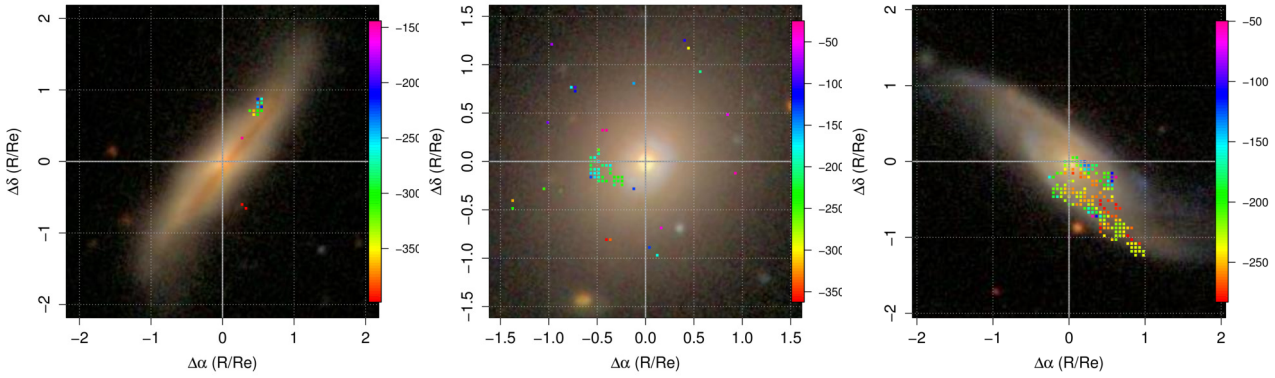

(j) NGC3160 (k) NGC3182 (l) NGC4644

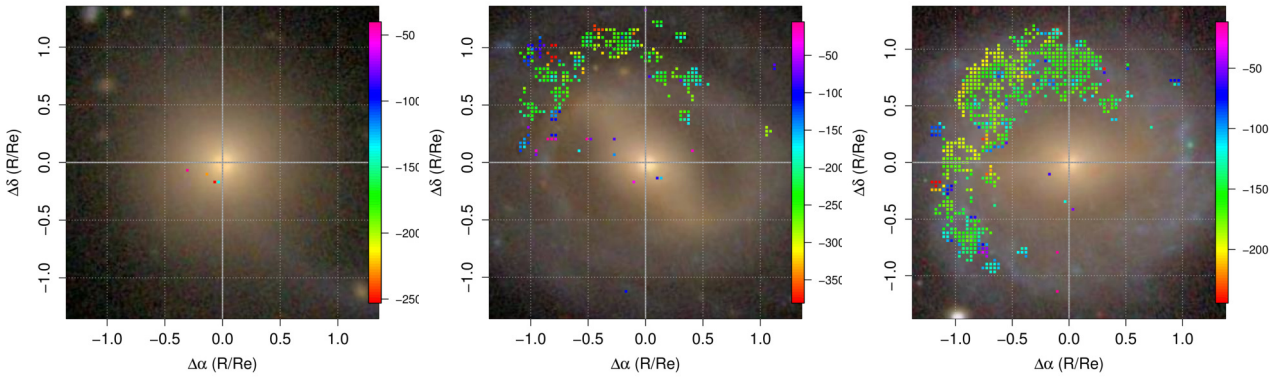

(m) NGC5216 (n) NGC5378 (o) NGC5957

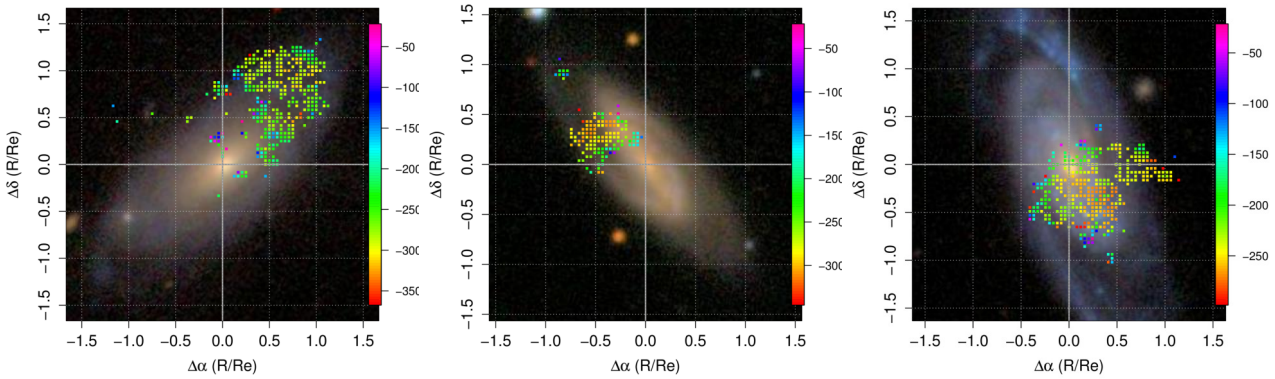

(p) NGC5971 (q) NGC6394 (r) UGC09110

Fig. A.16: Maps of the velocity in the line-of-sight of the blue shifted component of Hα. Continued.

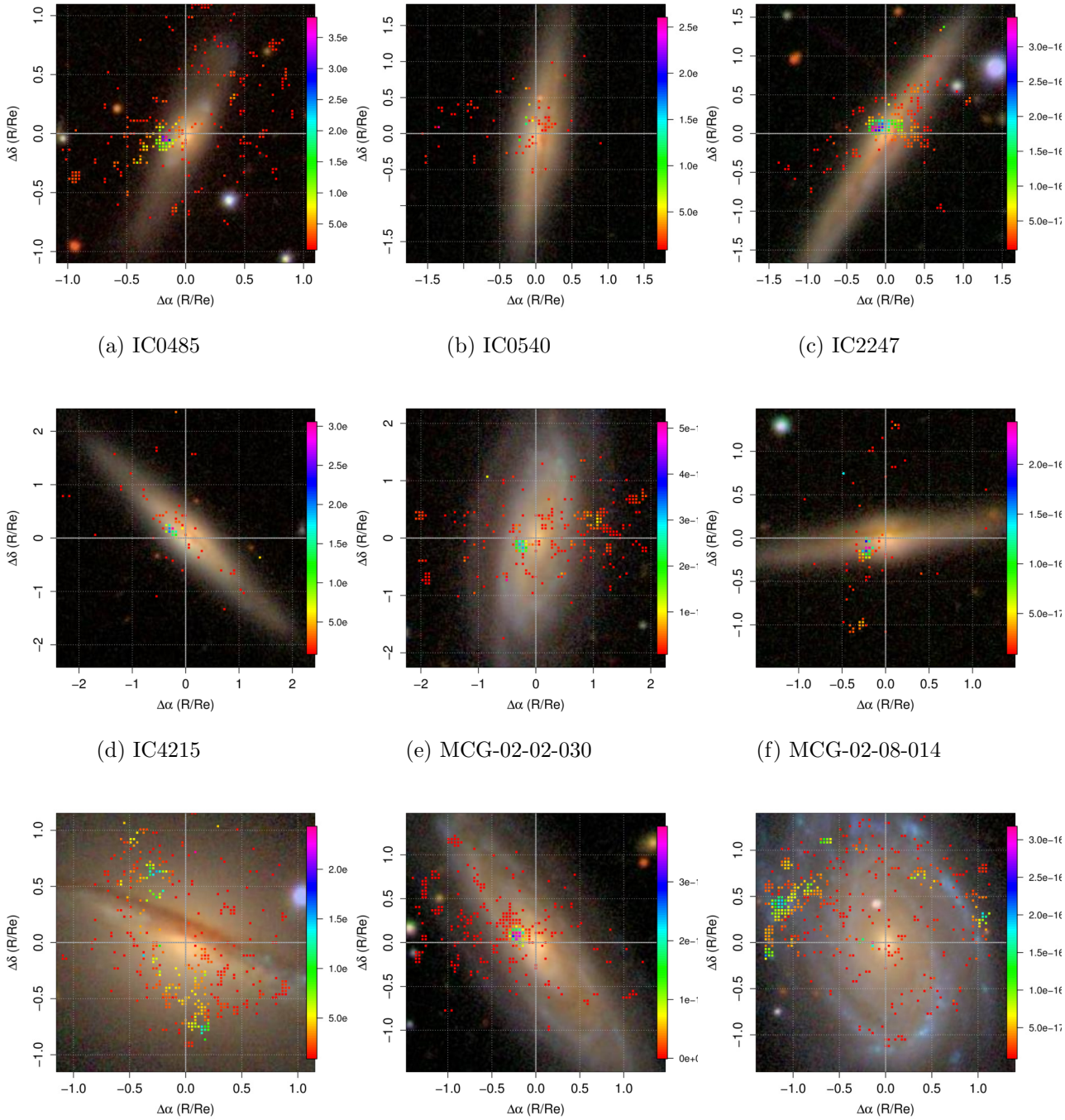

(a) IC0485 (b) IC0540 (c) IC2247

(d) IC4215 (e) MCG-02-02-030 (f) MCG-02-08-014

(g) NGC0681 (h) NGC2410 (i) NGC2916

Fig. A.17: Maps of the surface specific flux of the blue shifted component of [O III] λ5007. The colour code is in units of [erg s^{-1} cm^{-2} Å^{-1}] $arcsec^{-2}$].

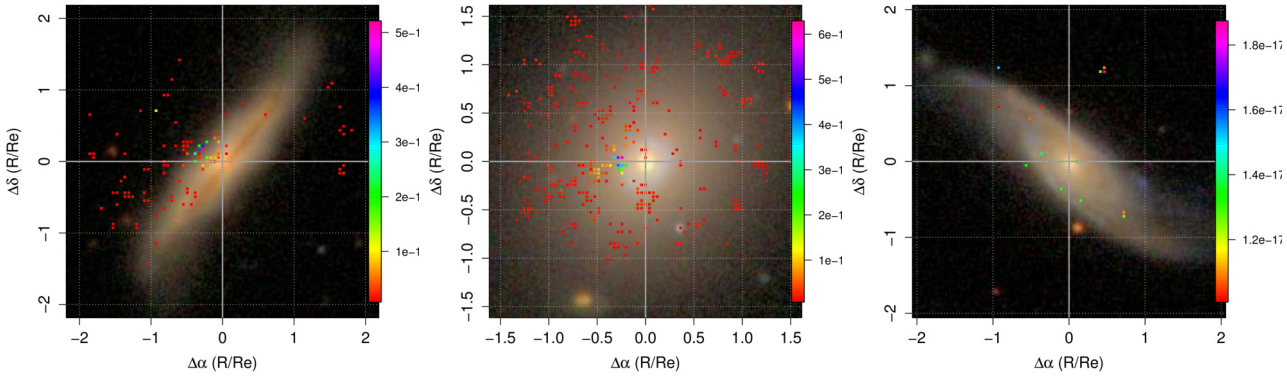

(j) NGC3160 (k) NGC3182 (l) NGC4644

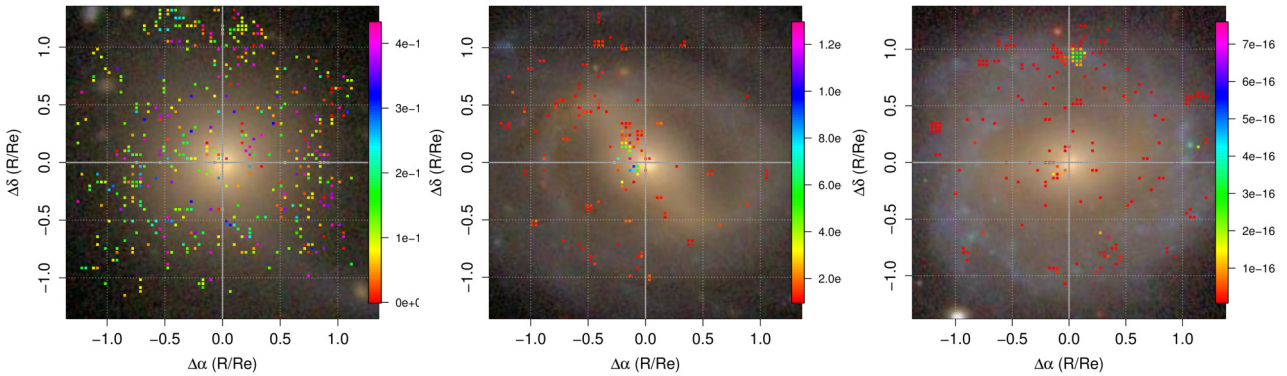

(m) NGC5216 (n) NGC5378 (o) NGC5957

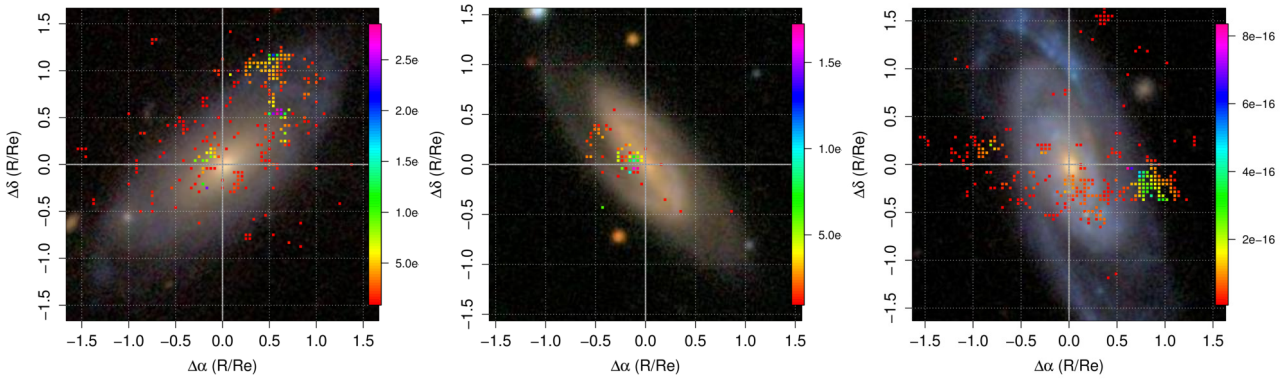

(p) NGC5971 (q) NGC6394 (r) UGC09110

Fig. A.17: Maps of the surface specific flux of the blue shifted component of [O III] λ5007. Continued.

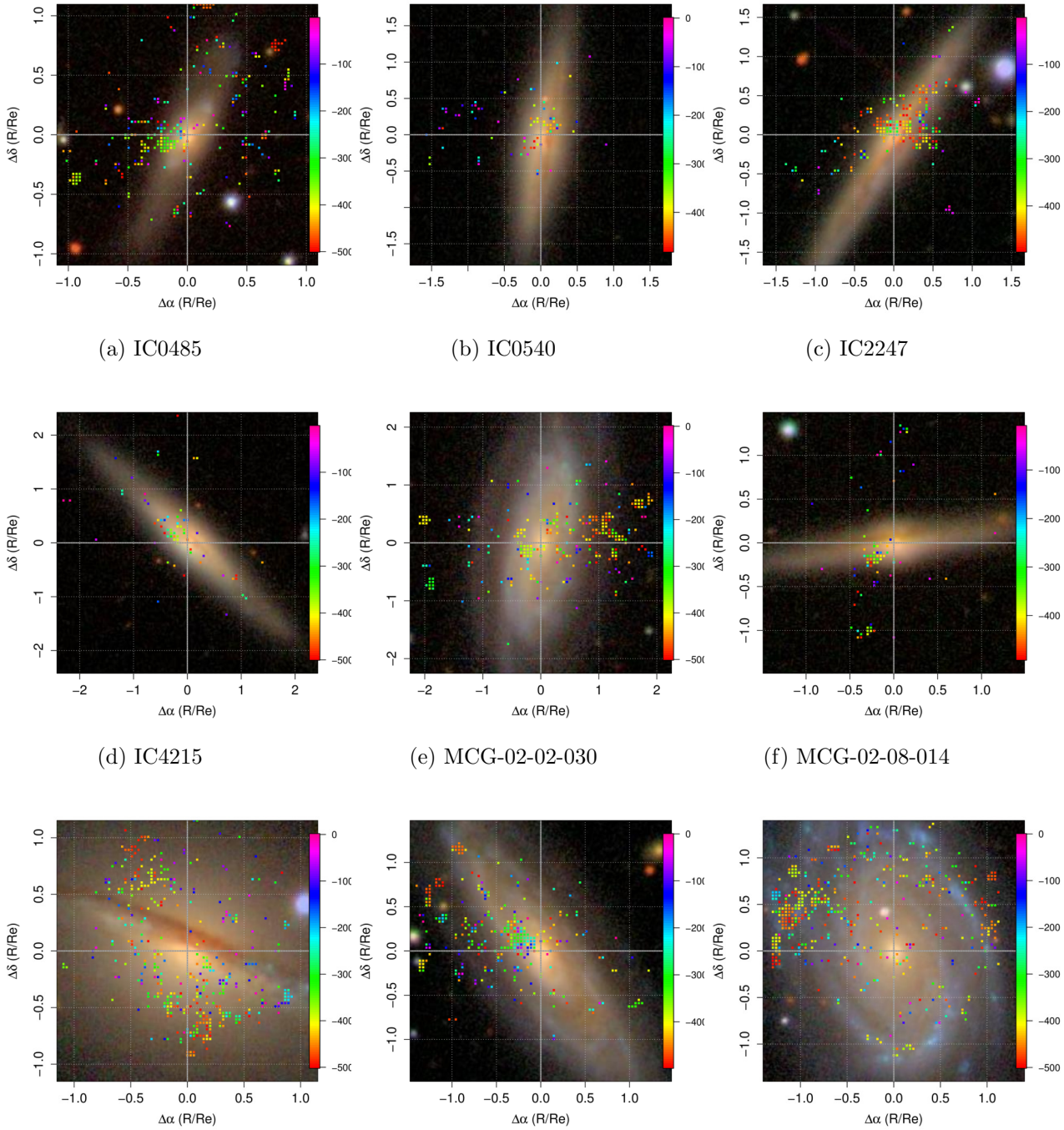

(a) IC0485 (b) IC0540 (c) IC2247

(d) IC4215 (e) MCG-02-02-030 (f) MCG-02-08-014

(g) NGC0681 (h) NGC2410 (i) NGC2916

Fig. A.18: Maps of the velocity in the line-of-sight of the blue shifted component of [O III] λ5007. The colour code is in units of km s^{-1}.

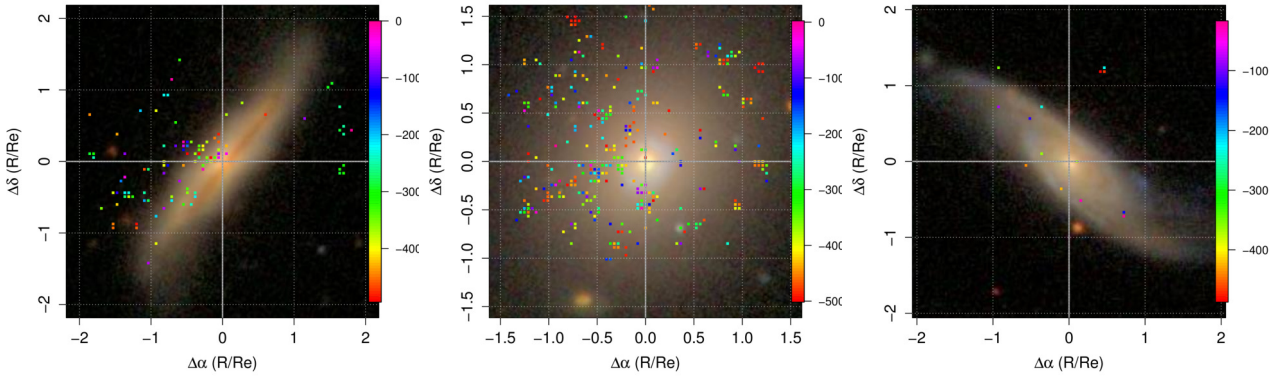

(j) NGC3160 (k) NGC3182 (l) NGC4644

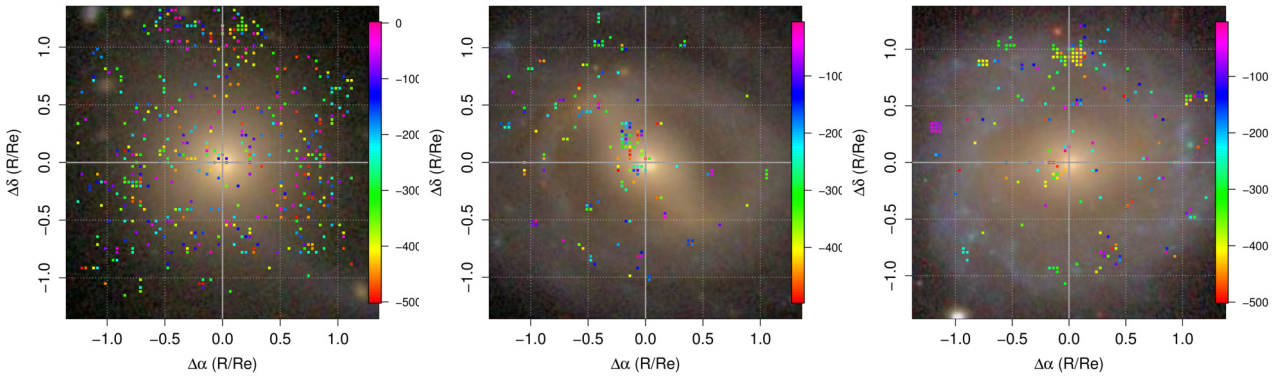

(m) NGC5216 (n) NGC5378 (o) NGC5957

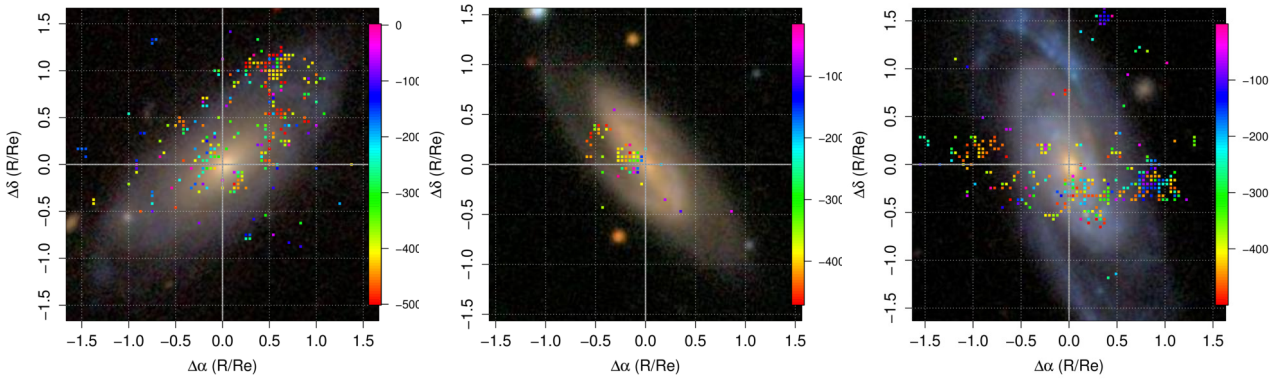

(p) NGC5971 (q) NGC6394 (r) UGC09110

Fig. A.18: Maps of the velocity in the line-of-sight of the blue shifted component of [O III] λ5007. Continued.

Appendix B

Kernel Density Estimation

A Kernel Density Estimation (KDE) is a non-parametric estimation of the Probability Density Function (PDF) for a continuous random variable. A Kernel is a PDF that meets the following criteria:

Even (symmetric)

Real-valued

Non-negative

It must be normalized so its definite integral over all data must be equal to 1.

At every datum from our data set, we assign a kernel function centered on the datum, so the kernel is symmetric about it. All resultant kernels are summed up and divided by the total number of data. The result is a PDF with the properties:

Non-Negative

Normalized so its definite integral is equal to 1.

This can be expressed as:

$$\hat{f}(x) = n^{-1}h^{-1}\sum_{i=1}^{n} K\left[\frac{(x - x_i)}{h}\right] \tag{B.1}$$

Where:

n is the number of data

h is the bandwidth

K is the selected kernel function

$(x - x_i)$ is the distance from the datum x_i to the point x where we are evaluating the kernel function

The kernel function K must be any function that satisfies the aforementioned criteria, usually a Gaussian function is used. h is known as the bandwidth, smoothing factor or window width. It limits the neighbourhood of values to which the probability is assigned by the kernel. As its integral is normalized to 1, at each datum, a larger value of h results in a shorter and wider probability function spreading farther from the centre implying a larger standard deviation. The value of h must be carefully selected. For small data sets, a large value of h is recommended, and a small one for large data sets.

In this work we always apply the Gaussian kernel and the bandwidth is selected using the rule-of-thumb by Silverman (1986). First we find which one is minimum: the variance of x or the interquartile distance divided by 1.34. We will call this selected value w. The bandwidth is then:

$$h = 4.24 w^{\frac{1}{2}} n^{-\frac{1}{5}} \tag{B.2}$$

Appendix C

Guía para desenrojecer espectros según el método de CCM89

C.1 Desenrojecimiento de un espectro o una línea

C.1.1 Deducción de la ecuación general de enrojecimiento

Hay diferentes formas, todas equivalentes, de llegar a esta ecuación. En este caso seguiremos el procedimiento explicado en el libro de Osterbrock & Ferland (2006). La solución de la ecuación de transferencia radiativa para el caso de absorción pura (en realidad es absorción más dispersión fuera de la línea de visión) es:

$$I_\lambda = I_{\lambda 0} e^{-\tau_\lambda} \tag{C.1}$$

donde I_λ es la intensidad (específica) observada (enrojecida), $I_{\lambda 0}$ es la intensidad que observaríamos si no hubiera extinción (la intrínseca) y τ_λ es la profunidad óptica en la línea de visión. Pasando el exponencial del lado derecho de la ecuación a base 10, sabemos que $e = 2.71828 = 10^{0.4342942}$, por tanto:

$$I_\lambda = I_{\lambda 0} 10^{-0.434(\tau_\lambda)} \tag{C.2}$$

Podemos describir la profundidad óptica dependiente de la longitud de onda mediante una ley de enrojecimiento (reddening law) $f(\lambda)$, también llamada ley de extinción, que depende de la longitud de onda:

$$\tau_\lambda = C f(\lambda) \tag{C.3}$$

y nos queda:

$$I_\lambda = I_{\lambda 0} 10^{-0.434[C f(\lambda)]} \tag{C.4}$$

Podemos sustituir las constantes del exponente por $c = 0.434C$ y reescribir:

$$I_\lambda = I_{\lambda 0}\ 10^{-c[f(\lambda)]} \tag{C.5}$$

que es la ecuación general de enrojecimiento; c debe ser determinada en cada caso, y está relacionada a la forma de la curva de extinción, es decir, cómo varía la extinción de una λ a otra, que normalmente se relaciona directamente al exceso de color $E(B-V)$ (para el caso explicado en la sección C.1.2 con $R_V = 3.1$, $E(B-V) \approx 0.77c$).

Se debe tener cuidado con la interpretación de esta ecuación. En este caso introducimos en ella la intensidad intrínseca de la fuente sin enrojecer y obtenemos la que deberíamos observar una vez que la luz atraviesa el medio interestelar y sufre enrojecimiento. El caso práctico suele requerir lo contrario: queremos encontrar la intensidad intrínseca a partir de la observada, para lo cual debemos despejarla, y tiene efecto en el cambio de signo del exponente.

$$I_{\lambda 0} = I_\lambda \ 10^{c[f(\lambda)]} \tag{C.6}$$

C.1.2 El método de Cardelli

Siguiendo el artículo de Cardelli et al. (1989), conocido como CCM89:

$$R_V = \frac{A(V)}{E(B-V)} \tag{C.7}$$

A_V es la extinción en la banda V en magnitudes. $E(B-V)$ es el exceso de color entre las bandas B y V (en magnitudes), que nos da una medida de la pendiente del espectro.

En CCM89 hicieron un ajuste de mínimos cuadrados de $A(\lambda)/A(V)$ vs R_V^{-1} que da como resultado lo que nos da la ley de extinción $f_V(\lambda)$ normalizada en la banda V (y promediada para cada R_V), donde $A(\lambda)$ es la exitinción en magnitudes a la longitud de onda λ que nos interesa desenrojecer (que podemos aplicársela a líneas individuales o a todo el espectro) y $A(V)$ es la extinción en magnitudes en la banda V:

$$f_V(\lambda) = \left\langle \frac{A(\lambda)}{A(V)} \right\rangle = a(x) + \frac{b(x)}{R_V} \tag{C.8}$$

donde los coeficientes $a(x)$ y $b(x)$ vienen dados por los polinomios:

$$a(x) = 1 + 0.17699y - 0.50447y^2 - 0.02427y^3 + 0.72085y^4 + 0.01979y^5 - 0.77530y^6 + 0.32999y^7 \tag{C.9}$$

$$b(x) = 1.41338y + 2.28305y^2 + 1.07233y^3 - 5.38434y^4 - 0.62251y^5 + 5.30260y^6 - 2.09002y^7 \tag{C.10}$$

en los que $x = 1/\lambda$ y $y = x - 1.82$.

El hecho de que el segundo término del lado derecho de la ecuación C.8 esté dividido por R_V implica que está normalizado por $A(V)$ (ver ecuación C.7). Siempre hay que tener presente que la ley de extinción tal cual la presenta CCM89 está normalizada respecto a la banda V. Para la Vía Láctea se toma $R_V = 3.1$, pero no es necesariamente cierto para la extinción interna de otras galaxias y puede ser necesario calcularlas para cada caso a partir de la ecuación C.7 (u otros métodos). Con esto, podemos desenrojecer cualquier línea (en efecto, cualquier longitud de onda, incluidas las del contínuo) mediante la siguiente ecuación (ver sección C.1.1):

$$I_{\lambda 0} = I_\lambda \ 10^{cf(\lambda)} \tag{C.11}$$

donde I_λ es la intensidad observada (enrojecida) a la longitud de onda λ y $I_{\lambda 0}$ es la intensidad intrínseca y c es una constante a determinar que depende de la normalización que usemos.

C.2 Normalización respecto a Hβ

Para trabajar con líneas nebulares en el óptico, y especialmente en la medición de abundancias químicas, suele seguirse la convención de normalizar respecto a Hβ. Esto es conveniente porque conocemos bien la razón de las intensidades de las líneas Hα y Hβ para las condiciones físicas típicas de las regiones H II ($T_e = 10000$ K y $n_e = 100$ cm^{-3}) en cuyo caso se cumple que

Primero debemos normalizar la ley de extinción, dividiendo cada uno de los valores que calculamos para las diferentes longitudes de onda por la ley de extinción de Hβ:

$$f_{H\beta}(\lambda) = \frac{f_V(\lambda)}{f_V(H\beta)} \tag{C.12}$$

Normalizamos la ecuación C.11 por Hβ para la longitud de onda que nos interesa, usando las leyes de extinción normalizadas de la ecuación C.12:

$$\frac{I_{\lambda 0}}{I_{H\beta 0}} = \frac{I_\lambda}{I_{H\beta}} 10^{c(H\beta)\ [f_{H\beta}(\lambda) - f_{H\beta}(H\beta)]} \tag{C.13}$$

Donde $I_{H\beta 0}$ es la intensidad intrínseca de la línea Hβ, $I_{H\beta}$ su intensidad observada y $c(H\beta)$ es la constante c de la ley de extición para la normalización por $H\beta$. Como precisamente normalizamos las leyes de extinción respecto a Hβ, entonces $f_{H\beta}(H\beta) = 1$ y podemos reescribir la ecuación anterior como:

$$\frac{I_\lambda 0}{I_{H\beta 0}} = \frac{I_\lambda}{I_{H\beta}} 10^{c(H\beta)\ [f_{H\beta}(\lambda) - 1]} \tag{C.14}$$

Ahora necesitamos la constante $c(H\beta)$. Como se mencionó antes, podemos simplemente despejar $c(H\beta)$ directamente de la ecuación C.14 a partir de la razón $I_{H\alpha}/I_{H\beta} = 2.86$ como se mencionó anteriormente:

$$c(H\beta) = \frac{\log_{10} 2.86 - \log_{10}\left(\frac{I_{H\alpha}}{I_{H\beta}}\right)}{f_{H\beta}(H\alpha) - 1} \tag{C.15}$$

Con este resultado ya podemos aplicar la ecuación C.14 a todas las demás líneas (o al contínuo). Existe la convención, especialmente en el estudio de abundancias en el óptico, de que se multiplique siempre el resultado de la ecuación C.14 por 100, de modo que si todo salió bien, el resultado para Hβ siempre debe de ser 100 y para Hα de 286. Si obtenemos otros valores, significa que cometimos un error en el proceso, por tanto verificar que obtuvimos estos valores es una prueba de control que siempre vale la pena realizar. Es importante estudiar detenidamente el artículo de referencia y las ecuaciones de cada método de medición de abundancias químicas que utilicemos, para saber qué nos están pidiendo exáctamente. También hay que tener en cuenta que si no estamos tratando regiones H II comunes, las condiciones físicas mencionadas arriba podrían no cumplirse y el valor $I_{H\alpha}/I_{H\beta}$ podría ser diferente a 2.86; por ejemplo el artículo de L. Kewley et al. (2001), que utiliza $I_{H\alpha}/I_{H\beta} = 3.1$ para AGNs.